
# Transverse Oscillations of Non-Planar Coronal Loops

**Amy Scott**

**Submitted for the degree of Doctor of Philosophy**

**School of Mathematics and Statistics**

**August 2012**

**Supervisors: Professor Michael S. Ruderman, Professor Robert von Fáy-Siebenbürgen**

**University of Sheffield**

## Acknowledgements

I would like to thank my supervisors, Misha and Robertus, for their help over the years and for giving me the chance to do this PhD. I would also like to thank the STFC for the funding they provided because I would not have been able to complete my studies without it. It has been a great four years and as well as doing research my PhD has given me the opportunity to do things I never expected I'd do - visiting China for example!

I would also like to thank the many friends I've made while I've been in Sheffield, for making this a fun four years and for all the work related encouragement along the way. There are too many people to mention you all individually but I do want to say a big thank you to Tacita and Elena for putting up with all the messages I sent when thesis writing wasn't going very well!

Finally, a huge thank you goes to my Mum and Dad for all of their support throughout the many ups and downs of PhD life. Thanks for telling me to keep going every time I wanted to stop! If you're reading this then it means I finally made it to the point where I have a thesis - yay!

August 2012

P.S. Thanks to Mum, Dad, Elena, Elizabeth, Amy, Al and Shazia for helping to keep me going while the deadline was approaching and everything seemed impossible!

December 2012

## Abstract

In this thesis a non-planar coronal loop model is introduced. The loop has helical geometry and therefore has non-zero curvature and torsion. A curvilinear coordinate system is introduced, which uses the loop axis as a coordinate line and the loop boundary as a coordinate surface. We assume that the density along the loop is stratified. The governing equation for kink oscillations of the loop is derived under the assumption of the thin tube approximation. It is found that the governing equation has the same form as the governing equation for a straight loop with density varying along the tube. Therefore we find that the curvature and torsion do not directly affect the eigenfrequencies, although they still affect the eigenfrequencies indirectly through modifying the density profile along the loop. The main effect of the loop torsion is that it alters the polarization of the oscillation. We find that, for a loop with non-zero torsion, the direction of polarization rotates with the principal normal as we move along the loop. Observational signatures of kink oscillations of a non-planar loop are discussed.

We also investigate whether the non-planarity of a loop has any effect on the results of coronal seismology. We consider two seismological applications: the estimate of the density scale height in the corona using the ratio of the periods of the fundamental harmonic and first overtone of kink oscillations, and the estimate of the magnetic field strength obtained from the period of the fundamental harmonic and the loop length. We show that the non-planarity of the loop does not affect the period ratio, and therefore does not change estimates of the density scale height, and we find that density stratification and loop non-planarity only have a weak effect on estimates of the magnetic field strength.

## Copyright Notices

# Contents

# Chapter 1

# Introduction

## 1.1 The Sun

The Sun is a highly complex object with many different motions and features influencing its appearance. It is composed of plasma and is inhomogeneous throughout its mass. The Sun is powered by nuclear fusion reactions in its core where protons are fused together to form helium nuclei, releasing energy in the process. The core forms part of the solar interior, along with the radiative and convection zones. The interior is surrounded by the solar atmosphere, which stretches from the solar surface out into the Solar System.

The theoretical view of the solar atmosphere has changed significantly over the last several decades. For many years it was assumed to be gravitationally stratified and separated into layers at specific heights. However, the image of the atmosphere has increased in complexity as increasingly sophisticated spacecraft send back new data (Aschwanden et al., 2001). The current description of the atmosphere still includes these layers, which are known as the photosphere, chromosphere, transition region and corona, but the locations of the boundaries between them are less defined.

A factor which contributes to the atmosphere's lack of homogeneity is the solar magnetic field, which is generated by a dynamo at the base of the convection zone. This magnetic field can emerge from beneath the surface and move up through the atmosphere, creating various structures on many different scales (Solanki et al., 2006). These structures take different forms depending on the properties of the plasma which surrounds them.

The photosphere is the visible surface of the Sun and here the plasma is relatively cool and dense in comparison to the rest of the atmosphere. Here the magnetic field is often found to be aligned in the radial direction and high concentrations of field are mainly found in active regions and as part of the network field (Priest, 2000; Solanki et al., 2006). Active regions usually consist of two areas of opposite polarity, which are connected by magnetic field lines. They are mostly found within $\pm 30^{\circ}$ of the equator and are visible as sunspots (Aschwanden, 2009). The network field outlines granule and supergranule patterns. Granules and supergranules represent the tops of convection cells below the surface. They have a typical scale of 1000 km and 30 000 km, respectively, and field lines are seen to collect at the cell boundaries, due to the outward motion of the granular plasma, from the cell centres to their edges (Foukal, 2004; Solanki et al., 2006). Here the field lines are constantly perturbed by the buffeting of granules, which is a possible driver for waves seen higher in the atmosphere.

The photosphere is approximately 500 km thick and occupies the region of the solar atmosphere between the convection zone and the temperature minimum, where the temperature has dropped to 4300 K from its value of 6600 K at the base of the photosphere (Priest, 2000). On top of the photosphere lies the chromosphere. Here the temperature starts to increase unexpectedly with height, slowly at first but quickly reaching $\sim 10^4$ K in the upper chromosphere. The chromosphere has more structuring than the photosphere and is highly inhomogeneous (Golub and Pasachoff, 2002). The network field can still be seen at these temperatures but sunspots are not, although bright regions known as plages are found near sunspot locations (Foukal, 2004). Dark filaments are seen in the plage outlining regions of different polarity and it is likely that magnetic field lines arch over them to connect the different regions (Golub and Pasachoff, 2002). Other chromospheric features are spicules, mottles and fibrils. It is possible that these features are all related but their appearance is slightly different depending on where they are seen (Foukal, 2004). Spicules are seen on the limb and are jets of plasma which rise from the chromosphere following magnetic field lines. It is possible that mottles are actually the same structures as spicules but viewed on the disk rather than the limb. This is hard to prove due to their short lifetime of only 5 to 10 minutes, but seems likely due to their

similar physical characteristics (e.g. Sterling, 2000; Kuridze et al., 2012). In contrast to spicules, which are approximately vertical, fibrils are horizontal and lie parallel to the disk. However, it is still possible that these two features are linked. Spicules are usually observed in quiet regions of the Sun, where the magnetic field is vertical and extends higher into the atmosphere before returning to the surface and connecting to a region of opposite polarity, whereas fibrils are seen in active regions where the field lines connect to closer regions, leading to the flatter, horizontal shapes (Foukal, 2004).

There is a further sharp increase in temperature from $10^4$ K to $10^6$ K when moving from the upper chromosphere into the outer region of the solar atmosphere known as the corona. This increase occurs over a short distance of approximately 100 km in a section of atmosphere called the transition region. The cause of this sudden temperature increase, in both the chromosphere and the transition region, is still unknown and is an active topic of research in solar physics today. In a gravitationally stratified model of the atmosphere, the transition region is assumed to be horizontal, but it is likely that this boundary does not have a uniform shape. The interface between the chromosphere and corona is thought to be influenced by spicules elevating cooler plasma, and hot plasma penetrating downwards via coronal structures which are connected to the photosphere (Golub and Pasachoff, 2010). Therefore, the region of temperature increase is unlikely to be at a constant height for all points on the Sun.

It is possible to image the corona in several different wavelengths, each of which reveals different features and provides information about the overall structure of the coronal plasma. Due to the extreme high temperatures in the corona, the plasma primarily emits in the EUV and soft X-ray portions of the spectrum. However, there are also many emission lines in the visible part of the spectrum, which are produced by emission from highly ionized elements (Golub and Pasachoff, 2010). The majority of emission at EUV and soft X-ray wavelengths comes from the corona, therefore providing a clear view of this part of the atmosphere. EUV and soft X-ray images of the corona show regions that are bright and others that are dark (see figure 1.1). The bright regions coincide with active regions and are formed from many closed magnetic field lines, whereas the dark regions correspond to areas where the field lines are

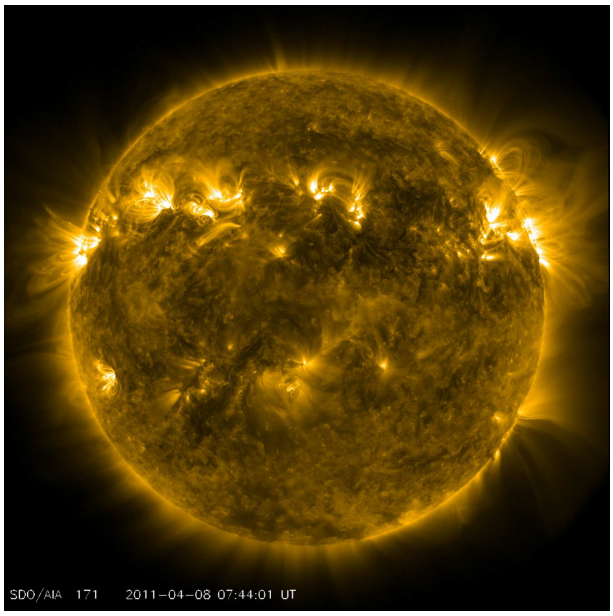


Figure 1.1: An EUV image of the solar corona. When imaged at a wavelength of 171 Å, we see that the corona has many bright and dark regions. (Courtesy of NASA/SDO and the AIA, EVE, and HMI science teams.)

open (Priest, 2000). Although these field lines are usually called open, it is important to remember that they are in fact closed, with one end located in the solar magnetic field and the other in a magnetic region far out in the Solar System. Since the field lines stretch out and away from the Sun, this gives them the appearance of being open. This is in contrast to the closed magnetic field lines that form active regions, which have both ends rooted in the solar magnetic field.

The closed magnetic field lines form large loop shapes and join regions of different magnetic polarity (see figure 1.2). They are known as coronal loops, of which there are several different types, but all with the same general structure. Coronal loops are magnetic flux tubes, filled with plasma of a higher density than that of the surrounding plasma. Their length varies depending on the type of loop, for example loops connecting active regions are typically up to 700 Mm long while post-flare loops are shorter, with lengths in the region of 100 Mm. An individual loop might only have a lifetime of approximately a day, but a whole loop system can last for several weeks (Priest, 2000).

The open field regions of the corona are called coronal holes. Here magnetic

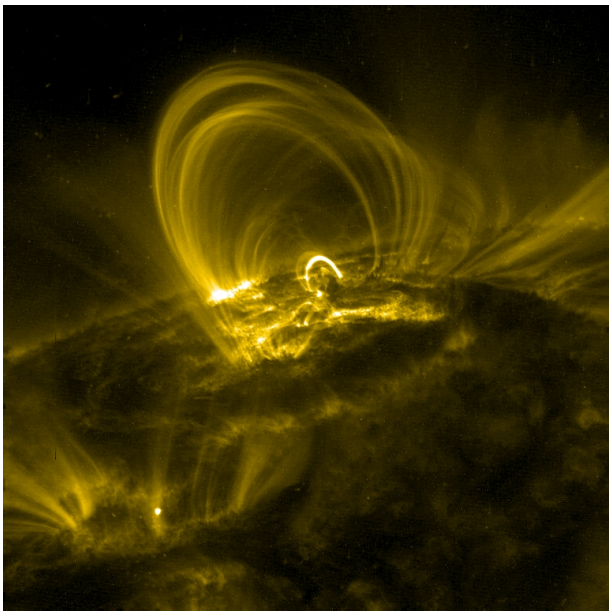

Figure 1.2: Coronal loops seen on the limb of the Sun. (Image courtesy of the Transition Region and Coronal Explorer, TRACE, which is a mission of the Stanford-Lockheed Institute for Space Research, and part of the NASA Small Explorer program.)

field lines extend out from the Sun into the Solar System. Plasma leaving the Sun along these field lines is known as the solar wind. A consequence of the plasma being removed from the Sun in this way is that the density and temperature in coronal holes are lower than the background coronal values, therefore explaining their dark appearance in images (Aschwanden, 2009). Coronal holes are commonly seen at the north and south poles, but also appear at other latitudes during times when the solar cycle is at a minimum (Golub and Pasachoff, 2010).

Other features can be seen on the limb when observing with visible wavelengths. As mentioned above, the corona emits light at several visible wavelengths, but another source of visible light that can be used to view the corona comes from photospheric emission which has been scattered by coronal electrons (Golub and Pasachoff, 2002). This light is much dimmer than the intense light shining from the photosphere and therefore can only be viewed when the main disk of the Sun is blocked either during an eclipse or by using a coronagraph, which acts as an artificial eclipse. Under these conditions, we see

structures that extend out to several solar radii, which are called streamers. Streamers are found located over active regions, or in the specific case of a helmet streamer, over prominences. They are formed from closed magnetic field lines, which cover the active region or prominence in the lower section of the structure, and form a pointed, cusp shape towards the top (Aschwanden, 2009). Over the course of the 11 year solar cycle, the locations of streamers are seen to change. Throughout solar minimum they are typically found at equatorial latitudes, but when activity increases during the maximum part of the cycle streamers are seen extending in all directions. This gives the corona a more spherical appearance when compared with its elliptical shape during solar minimum (Golub and Pasachoff, 2010). The latitudinal variation of streamers is also linked to the variation in the position of active regions throughout the solar cycle. At the beginning of each cycle active regions appear at high latitudes and as the cycle progresses they form at lower latitudes, gradually getting closer to the equator. Since streamers form over active regions, then they will also follow this trend. Smaller versions of streamers, known as polar plumes, are found near the coronal holes at each pole. They are typically seen near solar minimum when streamers are not observed at such high latitudes.

For the research which will be discussed in this thesis the most important solar features are coronal loops. The ends of these loops, called footpoints, are anchored in the photosphere because the magnetic field lines are frozen into the dense photospheric plasma. The section of the loop between the footpoints is free to move and can be disturbed by other motions in the surrounding atmosphere, such as a blast wave from a nearby flare. If a loop is perturbed in this way, then a magnetic restoring force will act to bring the loop back to its equilibrium position. If the disturbance is large enough, the effect of this force will be to set up oscillations in the loop, which will continue until the motion is damped (Aschwanden et al., 2001). One possible trigger of these oscillations is a propagating wave front excited by a nearby flare (Foukal, 2004).

There are several different ways a loop can oscillate but here we focus on standing kink oscillations. These are transverse oscillations in which the whole loop, including its axis, is seen to oscillate in phase. Many types of oscillations have been observed in the corona, but kink oscillations tend to be observed more frequently than others (e.g. Aschwanden, 2003; De Moortel and Nakariakov,

2012). This is because the whole loop moves from its equilibrium position and is therefore relatively easy to see, especially if the oscillating loop is near the limb of the Sun. These oscillations and the main theory used to describe them, magnetohydrodynamics (MHD), will be explained in chapter 2, but first to complete this introduction, there will be a short review of research concerning these oscillations and how different models can affect the wave modes we might expect to see.

## 1.2 Transverse Oscillations of Coronal Loops

The first transverse oscillations of coronal loops were imaged by the *Transition Region And Coronal Explorer* (TRACE) in 1998. The observations were reported by Aschwanden et al. (1999) and Nakariakov et al. (1999) and identified as fast kink MHD standing waves. Since then, many other oscillation events have been seen by TRACE (e.g. Schrijver et al. (2002)) and other new spacecrafts, such as the *Solar Dynamics Observatory* (SDO) (e.g. Aschwanden and Schrijver, 2011; White and Verwichte, 2012).

Schrijver et al. (2002) reported that loop oscillations have never been seen under quiet conditions. This is unsurprising since oscillations are usually triggered or driven by an event such as a flare, which are typically found in active regions. On the other hand, not all loops in an active region are seen to oscillate following a nearby event. Aschwanden et al. (2001) discussed a case where only six out of the hundreds of loops in the flaring region were seen to oscillate. They explained this by saying that not all loops matched the kink-mode resonance, while others could have been strongly damped such that the oscillation did not have time to establish itself. Another way for oscillations to be excited is through granular motions at the loop footpoints, which act as a continuous driver for the oscillation.

Coronal loop oscillations had been studied theoretically for many years before they were imaged, with an aim of investigating possible wave modes. However, after they were observed, research efforts increased in an attempt to improve our theories and understanding of these features.

Sound oscillations in magnetic tubes situated in an unmagnetized plasma were first considered by Ryutov and Ryutova (1976), who found that the os-

cillations can be damped due to scattering of sound waves by the magnetic tubes. Other early work in this area was done in a series of papers by Roberts (1981a,b) and Edwin and Roberts (1982, 1983). Their research discusses the propagation of different kinds of waves in various types of magnetic structures. In the first paper, Roberts (1981a) considered the interface between two regions, one of which was field-free. Here the magnetic field was aligned such that the field lines were parallel to the boundary. It was found that at the interface between the two regions a slow surface wave could always propagate. In addition, if the temperature in the field-free region is greater than that of the magnetic region, then it is possible for a fast surface wave to propagate. In the second paper, Roberts (1981b) considered a magnetic slab in a field-free environment, where the magnetic field was oriented such that the field lines were parallel to the slab boundaries. Here, slow surface and body waves can always propagate, although the fast mode can only propagate if the slab is cooler than the outer medium. The fast wave propagates as a body or surface wave depending on whether the external sound speed is greater or less than the Alfvén speed, respectively. Edwin and Roberts (1982) extended this idea further to a slab in a medium which itself had a magnetic field, but of a different magnitude to that in the slab. It was found that there are many vibrational modes which could be present in this situation and in general slow and fast, body and surface waves can propagate. However, the particular modes which are present depends upon the relative magnitudes of the sound and Alfvén speeds in each region. Finally, Edwin and Roberts (1983) studied wave propagation in a cylinder that had a magnetic field directed along it, which can be used to represent a coronal loop. Under coronal conditions it was found that the magnetic cylinder exhibited the two types of body waves but no surface waves. From this starting point of using a cylindrical model, many adaptations have been incorporated in an attempt to construct a more realistic model.

One important factor that has been included in coronal loop models is the density stratification of the solar atmosphere. The cylindrical model used by Edwin and Roberts (1983) assumed a constant density along the loop, although this is not very realistic. The height of a loop apex is typically larger than the density scale height in the corona, therefore density variation along the loop should be expected. However, we should remember that if the wavelength of

a particular oscillation is much smaller than the density scale height, then the oscillation will not be affected by the inhomogeneity of the plasma. This is because the density of the plasma will be approximately uniform over the space of a wavelength. Density stratification in a straight cylindrical tube has been studied by Andries et al. (2005b) who found that this leads to changes in the frequency of kink oscillations. The nature of the change in frequency depends on how the density is weighted along the loop. For example, for a density function defined with respect to a constant footpoint density, the oscillation frequency is found to increase as stratification increases. On the other hand, for a density function which keeps the apex density constant, the oscillation frequency is seen to decrease as stratification increases. Weighting the density function in other ways will lead to a result in between these two cases, and Andries et al. (2005b) demonstrated that it is possible to weight the density function such that the oscillation frequency is approximately invariant with respect to the stratification parameter. Density stratification has also been studied by Dymova and Ruderman (2005) for the case of a prominence fibril. Their model consisted of a straight cylindrical tube with a magnetic field directed along it and density varying in the direction parallel to the tube axis, both in and outside the tube. Since the tube radius of a fibril is generally much smaller than its length, Dymova and Ruderman (2005) introduced the ratio of these two quantities into their analysis and assumed that it was small. This assumption, known as the thin tube approximation, simplified the analytical derivation and allowed the governing equation for the oscillations to be found. Dymova and Ruderman (2005) discovered that the oscillation frequencies of this system are given by the eigenvalues of a Sturm-Liouville problem. Although this result was derived with prominence fibrils in mind, the equilibrium state of a thin cylindrical tube applies equally well to a coronal loop and this result is often quoted in relation to them.

Most loop models assume that the magnetic field is straight and directed along the length of the loop. However, it could also be possible for field lines to become twisted due to granular motions at loop footpoints or current systems in the atmosphere (Aschwanden, 2009). Several studies have been carried out to learn about the effect the magnetic twist has on various different wave motions. Ruderman (2007) examined standing oscillations of a twisted flux tube. The

model also included density stratification and used the thin tube approximation. For a weakly twisted tube it was found that the governing equation can be reduced to a Sturm-Liouville problem, which reduces further to the equation found by Dymova and Ruderman (2005) in the case where there is zero twist. The study concluded that there is no change to the kink mode of a thin twisted loop.

Although loop models generally assume a circular cross-section this is not necessarily the case. Erdélyi and Morton (2009) suggested that an elliptical cross-section could be caused by gravitational forces or the buffeting of flux tubes by supergranular motions at the loop footpoints. Ruderman (2003) studied a loop model of this form in a cold plasma. The analysis showed that introducing an elliptical cross-section for the tube, allows the kink mode to be polarized in two directions, either along the major or minor ellipse axis. The frequencies of these oscillations were found to be either smaller or larger than the kink frequency of a tube with a circular cross-section, respectively. Erdélyi and Morton (2009) extended these results to a finite-$\beta$ plasma. They also found the splitting of the kink mode into two polarizations and calculated that the difference in frequency between each polarization depends on the ellipticity. The largest difference occurs when the ellipticity is large, and for small values of ellipticity the frequencies tend towards that of the circular case.

The studies discussed so far have all considered a single loop structure. However, observations rarely show individual loops by themselves. They are usually part of a large system of loops in close proximity to each other, which suggests that interactions between loops could be a useful topic of study. There is also the possibility that loop structures could be formed from many different strands, which we are unable to see due to resolution limits of current observations. These strands are also likely to interact and could influence loop oscillations (Aschwanden, 2009). A multiple loop system was studied numerically by Luna et al. (2008), who modelled a system of two identical straight homogeneous loops which were parallel to each other. They found that loop systems of this type oscillate at a different frequency than would be expected for an individual loop. Four normal modes were found: the loops can oscillate in the plane containing the two loops or in the perpendicular direction, and in each direction a symmetric or antisymmetric mode is possible. These modes are represented by

$A_x$, $A_y$, $S_x$ and $S_y$, where $A$ and $S$ stand for the antisymmetric and symmetric modes, $x$ is the direction parallel to the loop plane and $y$ is the perpendicular direction. Van Doorsselaere et al. (2008) extended this model with an analytical study considering two identical tubes. The ratio of the distance between the loop axes and the length of the loops was assumed to be small. To a first order approximation in this small parameter, they also found these four modes, although each mode did not oscillate at an individual frequency. They found that the $A_x$ and $S_y$ modes oscillate at one frequency and the $A_y$ and $S_x$ modes oscillate at another, lower, frequency. The authors suggested that continuing to the next order approximation is likely to reveal different frequencies for each mode. Van Doorsselaere et al. (2008) also considered non-identical tubes, where their radius and density were not necessarily equal. Here the system can either have standard behaviour, with eigenmodes the same as in the identical tube case, or anomalous behaviour, with two $A_x$ and two $S_y$ type eigenmodes. Again they found only two frequencies, with each type having one high and one low frequency oscillation. A system is categorized as anomalous if the Alfvén frequency in one tube is higher than the lower of the two oscillation frequencies and standard if the Alfvén frequency in both tubes is lower than the lower frequency. Luna et al. (2009, 2010) continued their numerical studies by first considering a system of 3 loop strands, and then moving on to study systems of 10 and 40 loop strands. Their results showed that strands with similar densities oscillate at the same frequency, but if there is a large difference between densities, then they will oscillate as if they are individual loops. Another conclusion from Luna et al. (2010) is that due to the complex motions of the loop strands, a multi-stranded loop cannot be adequately described by a single loop structure.

Another factor of loop geometry which is often neglected is the loop curvature. Coronal loops are seen to arch high into the atmosphere, but loop models usually ignore this in favour of a simpler model featuring a straight tube. The effect of curvature on loop oscillations was first considered by Van Doorsselaere et al. (2004) and corrected by Van Doorsselaere et al. (2009), who defined a model based on a semi-toroidal magnetic field for the case of zero density stratification in a cold plasma. Using the aspect ratio of the loop as a small parameter in the thin tube approximation, they concluded that, to a first order

approximation, there is no change in the frequency or damping time of kink oscillations when curvature is included. They also found that any corrections to the frequencies caused by including second order terms would be at maximum 6%.

Considering a curved loop introduces the possibility of new directions of oscillation. Basing their ideas on observational data, Wang and Solanki (2004) suggested that there could be a vertical kink oscillation, as opposed to the horizontal mode that is usually studied. Díaz et al. (2006) also introduced vertical oscillations for a curved arcade, along with swaying and rocking modes. The vertical and swaying modes can be either sausage or kink, but the rocking mode corresponds only to a kink oscillation. They studied the vertical and swaying modes analytically and found that each mode has a separate frequency but if the structure is straightened then they become degenerate. Terradas et al. (2006) performed numerical studies on a toroidal loop. They too found that horizontal and vertical kink oscillations have different frequencies, but added that the difference between them is mainly noticeable if the loop is thick. Ruderman (2009) considered the case of a thin curved tube analytically, with density stratification and loop expansion included. The loop cross-section was elliptical and in this model expansion was caused by the loop curvature. The expansion was assumed to be weak and characterized by a small parameter, which was then used to perform a power series expansion. The results showed that to a first order approximation, the kink frequencies are the same as those found by Dymova and Ruderman (2005) for a straight cylindrical tube. However, the next order approximation showed the vertical and horizontal polarizations. Ruderman (2009) concluded that these modes have different frequencies due to the change in shape of the tube cross-section caused by the curvature of the tube. It was also noted that for a weak expansion the difference between these frequencies is small, but larger differences would be expected if the tube expansion was increased.

Extending a loop model to contain the realistic curved nature of coronal loops typically involves studying a loop which is confined to a plane when in its equilibrium position. From here we can think about developing this further to the possibility of a non-planar loop, which has non-zero torsion as well as non-zero curvature. A loop of this type will be considered throughout this thesis

and has not been studied theoretically before.

## 1.3 Coronal Seismology

Coronal seismology was first suggested by Uchida (1970) and Rosenberg (1970), and uses wave motions in the corona to estimate parameters of the coronal plasma and magnetic field that are difficult to measure directly. Uchida (1970) put forward an idea to use the motion and distortion of Moreton waves to investigate the magnetic field's structure in the path of the wave, and Rosenberg (1970) used the observed periodic pulsation of radio emission to estimate the magnetic field strength in coronal loops. Later, Roberts et al. (1984) considered using the modulation of radio signals by fast magnetoacoustic sausage waves in coronal loops to find the spatial dimensions of a structure along with the Alfvén speed inside and outside the structure.

Different wave motions provide a source of information about different aspects of coronal plasma. The transverse oscillations that have been discussed above can be used to estimate both the magnetic field strength and density scale height of oscillating loops. Nakariakov and Ofman (2001) developed a method to use the oscillation period of a loop along with its length to estimate the magnetic field strength in a loop. The authors noted that one source of error in these calculations comes from an inability to measure the loop length accurately due to projection effects. This is relevant to research involving non-planar loops, because if a non-planar loop is assumed to be planar then its length could be underestimated, and this would lead to the magnetic field strength being wrongly calculated.

Andries et al. (2005a) studied a loop model which included density stratification in the longitudinal direction and found that the density inhomogeneity does not affect each harmonic equally. This results in the ratio between the periods of the fundamental mode and first overtone being less than two, which would be the expected value for an unstratified loop. This is a useful seismological tool because the deviation of the period ratio from its expected value can provide us with information about the density scale height in the corona. Andries et al. (2005a) tested the method using multimode oscillations reported by Verwichte et al. (2004) and it was found to give reasonable values close to

the expected value of 50 Mm.

Both of these methods have proved to be successful in providing us with good estimates for their respective coronal parameters. However, it is interesting to see if these results vary when the loop model is changed. Nakariakov and Ofman (2001) assumed a straight homogeneous cylindrical tube and as far as we know the magnetic field strength has not been calculated using any other model. Andries et al. (2005a) analysed a semicircular tube with a constant circular cross-section located in a vertical plane. This model has been expanded on and varied many times in order to investigate which parameters influence the period ratio and density scale height, and some of these developments will be discussed below.

Another major factor which has been shown to affect the period ratio is loop expansion. Verth and Erdélyi (2008) modelled a flux tube with uniform density that had a larger radius at its apex than at its footpoints. They found that loop expansion has the opposite effect to longitudinal density stratification and causes the period ratio to increase. Hence, neglecting loop expansion would lead to the density scale height being overestimated. Ruderman et al. (2008) took this study further and included density variation along the loop in their model. As expected, they find that when loop expansion is included, the density scale height is less than would be found if only density stratification was considered.

Other features that have been studied and found to influence the period ratio are loop shape, radial structuring and cooling. Dymova and Ruderman (2006) and Morton and Erdélyi (2009a) examined the effect of loop shape by modelling a loop as a circular arc and an elliptical arc, respectively. Both studies showed that differing the loop shape does lead to small changes in the period ratio, although the change is smaller than that due to density stratification. Morton and Erdélyi (2009a) investigated both minor and major elliptical loops, which are categorized depending on which axis is in the vertical direction. Out of the two types they found that minor elliptical loops have the largest effect on the period ratio. For these loops it was shown that as the ellipticity increases, the period ratio increases with respect to the circular arc case. The authors noted that this difference between the circular and elliptical cases would be measurable in current observations and therefore it is important that the loop shape is obtained from observations along with other oscillation parameters. Radial

structuring of a loop has been considered by McEwan et al. (2006). Under the initial assumption of a loop with uniform density, they varied the dimensions of the loop and found that this also causes the ratio to decrease from two, with the maximum deviation occurring when the loop radius is approximately equal to, or slightly smaller than, its length. The period ratio was also found to decrease further as the ratio of the densities inside and outside the loop was increased. Next, they included the longitudinal density stratification and found that this has a much larger effect on the period ratio than structuring in the radial direction. Morton and Erdélyi (2009b) found that a change of loop temperature can affect the period ratio. They studied a straight cylindrical magnetic tube with longitudinal density structuring and in particular their results showed that as a loop cools, the period ratio decreases.

Other factors that have been studied and found not to influence the period ratio significantly are an elliptical loop cross-section (Morton and Ruderman, 2011) and multi-threaded loop structure (Robertson et al., 2010).

## 1.4 Motivation for Studying Non-Planar Loops

Since loops with non-zero curvature have previously been studied, moving onto loops which also have non-zero torsion seems a logical next step. There is also observational evidence which provides further motivation to study loops of this nature. Recently, Aschwanden et al. (2008) used data from the *Solar Terrestrial Relations Observatory* (STEREO) to reconstruct the 3D geometry of coronal loops. Their analysis found seven loops that were not confined to a plane, which provides evidence for the existence of non-planar loops in the corona.

Here we investigate a non-planar loop model, which we choose to have a helical form. Previous studies have suggested that other solar structures have a helical shape, such as filaments (Rust, 2003), prominences (Anzer and Tandberg-Hanssen, 1970), sigmoid structures (Rust and Kumar, 1996) and CMEs (Dere et al., 1999; Plunkett et al., 2000). In addition, the reconstructed shape of two, possibly three, of the seven loops examined by Aschwanden et al. (2008) showed the distinctive S-shape which would be characteristic of a helical loop. Furthermore, Aschwanden (2009) reconstructed the 3D motion of two coronal loops, which revealed both horizontal and vertical oscillations. In each case it was

found that the horizontal and vertical oscillations had similar periods, which suggested that they were linked. One possible outcome of this is the components combining to form a linearly polarized oscillation at some angle between the horizontal and vertical directions. However, the results also showed a phase difference between the two components and Aschwanden (2009) suggested that this introduced the possibility of the oscillation being circularly polarized if the loop had a helical shape. Therefore, theoretical studies of helical loop oscillations could prove useful.

The present thesis deals with the study of standing kink oscillations of a non-planar loop with helical geometry, and is organized as follows: Chapter 2 covers the theories of magnetohydrodynamics and waves in a magnetized plasma, which provides background information for the work in the following chapters. In chapter 3 the equilibrium state is defined and compared to observations of non-planar coronal loops. In chapter 4 the governing equation for kink oscillations of the loop is derived and we discuss the polarization and observational signatures of the oscillations. Chapter 5 explores any effects of this new loop geometry on estimates of the coronal density scale height and magnetic field strength found using the methods of coronal seismology. In chapter 6 we discuss an observation, which possibly shows a non-planar loop oscillation. Finally, the main conclusions of the work are summarized in chapter 7.

# Chapter 2

# Background Theories

The Sun and its atmosphere are in a state known as plasma. A plasma can be thought of as an ionized gas, although the fraction of ionized particles does not need to be large for the gas to display plasma characteristics. This is the case in the photosphere, whereas the corona is highly ionized.

The plasma state is very common and accounts for 99% of the Universe. Other than the Sun, there are many terrestrial and astrophysical examples including flames, the aurora and interstellar space (Baumjohann and Treumann, 1997). Plasmas contain approximately the same amount of positive and negative particles and therefore on a macroscopic scale they usually appear to be neutral. However, on a microscopic scale localized areas can occur where the charge is unbalanced.

There are two theories that can be used to describe a plasma. The first is kinetic theory, which is used to study plasma on a microscopic scale. The second is magnetohydrodynamics (MHD), which can be derived from kinetic theory using a statistical approach. MHD is a fluid theory and describes the macroscopic properties of a plasma (Aschwanden, 2009). In the case of the corona it is more appropriate to use the second of these theories, MHD. This is because the typical length scales of coronal structures are much greater than plasma parameters such as the ion gyro radius, and time scales for variations in the plasma are much longer than collisional time scales. Therefore we can approximate the plasma as a continuous fluid, which can be described using MHD.

In section 2.1 the basic equations of MHD will be discussed, before moving

on to describe the wave modes that are possible in a magnetized plasma in section 2.2. Section 2.3 will then consider kink oscillations in the specific case of a cylindrical magnetic tube.

## 2.1 Magnetohydrodynamics

Magnetohydrodynamics links the fluid properties of a plasma to the effect that a magnetic field has on it. The electromagnetic fields involved can be described using Maxwell's equations, (2.1) to (2.4) (e.g. Goedbloed and Poedts, 2004),

$$\nabla \times \boldsymbol{E} = -\frac{\partial \boldsymbol{B}}{\partial t}, \tag{2.1}$$

$$\nabla \times \boldsymbol{B} = \mu_0 \boldsymbol{j} + \frac{1}{c^2}\frac{\partial \boldsymbol{E}}{\partial t}, \tag{2.2}$$

$$\nabla \cdot \boldsymbol{E} = \frac{\rho_c}{\varepsilon_0}, \tag{2.3}$$

$$\nabla \cdot \boldsymbol{B} = 0. \tag{2.4}$$

In the above equations $\boldsymbol{B}$ is the magnetic field, $\boldsymbol{E}$ is the electric field, $\boldsymbol{j}$ is the current density, $\rho_c$ is the charge density and the speed of light $c = (\varepsilon_0 \mu_0)^{-1/2}$ where $\varepsilon_0$ and $\mu_0$ are the permittivity and permeability of free space, respectively. Equations (2.1) and (2.3) are the Faraday and Gauss equations, respectively, and show that either a time varying magnetic field or electric charges can produce an electric field. Equation (2.2) tells us that a time varying electric field or a current can produce a magnetic field. Finally the solenoidal constraint, equation (2.4), shows that there are no magnetic monopoles and also implies that a magnetic flux tube has a constant strength along it (Priest, 2000; Goedbloed and Poedts, 2004).

The fluid properties of the plasma can be expressed using the fluid equations,

$$\frac{\partial \rho}{\partial t} + \nabla \cdot (\rho \boldsymbol{v}) = 0, \tag{2.5}$$

$$\rho \frac{\partial \boldsymbol{v}}{\partial t} + \rho \boldsymbol{v} \cdot \nabla \boldsymbol{v} = -\nabla p + \boldsymbol{F}, \tag{2.6}$$

$$\frac{\partial u}{\partial t} + \nabla (u \boldsymbol{v}) = -p \nabla \cdot \boldsymbol{v} - \nabla \cdot \boldsymbol{h} + S. \tag{2.7}$$

Here $\rho$ is the density, $p$ is the pressure, $\boldsymbol{v}$ is the plasma velocity, $\boldsymbol{F}$ represents all the inertial forces per unit volume acting on the plasma, such as gravitational, viscous or magnetic forces, $u$ is the internal energy density, $\boldsymbol{h}$ is a heat conduction vector and $S$ accounts for heating and cooling due to collisions and radiation. Equation (2.5) is the continuity equation and represents the conservation of mass in the system. Equation (2.6) is known as the equation of motion and is derived from Newton's second law. Finally, equation (2.7) is an energy equation, of which there are many different forms depending on which dependent variables are being used. The energy equation follows from the first law of thermodynamics and represents the conservation of energy in the system (Choudhuri, 1998).

These are the basic equations that can be used to describe a plasma. However, in systems that are usually governed by MHD, there are assumptions that can be made to simplify them. The first of these is to assume that changes in the electric and magnetic field are non-relativistic and therefore $v_0 \ll c$, where $v_0 = l_0/t_0$ is a characteristic plasma speed and $l_0$, $t_0$ are a characteristic length and time, respectively. In addition, typical values for the magnetic field, $B_0$, and electric field, $E_0$, can be assumed such that the magnitudes of each side of equation (2.1) are the same, i.e. $E_0/l_0 \approx B_0/t_0$. This can be used to consider the size of the terms in equation (2.2). Starting with the second term on the right hand side, known as the displacement current, this has a magnitude of

$$\frac{E_0}{c^2 t_0} \approx \frac{B_0 l_0}{c^2 t_0^2} \approx \frac{v_0^2 B_0}{c^2 l_0} \approx \frac{v_0^2}{c^2} |\nabla \times \boldsymbol{B}|. \tag{2.8}$$

Due to the non-relativistic condition introduced above, this term is much smaller than the left hand side of the equation and hence can be ignored, resulting in $\nabla \times \boldsymbol{B} = \mu_0 \boldsymbol{j}$ (Priest, 2000).

The distribution of ions in a plasma is usually such that the plasma appears neutral. Therefore the number density of positive ions, $n_+$, is approximately equal to the number density of negative ions, $n_-$, and hence $n_+ - n_- \ll n$, where $n$ is the total number density and we have assumed a hydrogen plasma. This means that the charge density, $\rho_c = (n_+ - n_-)e \ll ne$. Hence, $\rho_c$ is negligible, meaning that we can remove equation (2.3) from our system of equations, although it can still be used if we are required to find a value for $\rho_c$.

Finally, an equation known as the induction equation can be derived from equations (2.1), (2.2) and Ohm's law, $\boldsymbol{j} = \sigma(\boldsymbol{E} + \boldsymbol{v} \times \boldsymbol{B})$, which states that the current density is proportional to the total electric field of the system. The total electric field consists of the electric field, $\boldsymbol{E}$, which would act on the system at rest, plus the electric field, $\boldsymbol{v} \times \boldsymbol{B}$, due to the movement of the plasma in a magnetic field (Priest, 2000). Starting with equation (2.1), Ohm's law can be substituted in to give

$$\frac{\partial \boldsymbol{B}}{\partial t} = -\nabla \times \boldsymbol{E} = -\nabla \times (\boldsymbol{j}/\sigma - \boldsymbol{v} \times \boldsymbol{B}) = -\nabla \times (\boldsymbol{j}/\sigma) + \nabla \times (\boldsymbol{v} \times \boldsymbol{B}). \quad (2.9)$$

Then use of the simplified form of equation (2.2), $\nabla \times \boldsymbol{B} = \mu_0 \boldsymbol{j}$, allows the above equation to be written as

$$\frac{\partial \boldsymbol{B}}{\partial t} = \nabla \times (\boldsymbol{v} \times \boldsymbol{B}) - \nabla \times (\eta \nabla \times \boldsymbol{B}), \quad (2.10)$$

where $\eta = 1/\mu_0\sigma$ is the magnetic diffusivity and $\sigma$ is the conductivity of the plasma. Finally, assuming $\eta$ is constant and the use of the vector identity

$$\nabla \times (\nabla \times \boldsymbol{B}) = \nabla(\nabla \cdot \boldsymbol{B}) - (\nabla \cdot \nabla)\boldsymbol{B} \quad (2.11)$$

and the solenoidal constraint, equation (2.4), allows the induction equation to be written in a simpler form

$$\frac{\partial \boldsymbol{B}}{\partial t} = \nabla \times (\boldsymbol{v} \times \boldsymbol{B}) + \eta \nabla^2 \boldsymbol{B}. \quad (2.12)$$

The induction equation links the fluid properties of the plasma to the magnetic field through the $\boldsymbol{v} \times \boldsymbol{B}$ term.

To summarize, the basic equations of MHD are

$$\frac{\partial \rho}{\partial t} + \nabla \cdot (\rho \boldsymbol{v}) = 0, \quad (2.13)$$

$$\rho \frac{\partial \boldsymbol{v}}{\partial t} + \rho \boldsymbol{v} \cdot \nabla \boldsymbol{v} = -\nabla p + \boldsymbol{F}, \quad (2.14)$$

$$\frac{\partial u}{\partial t} + \nabla(u\boldsymbol{v}) = -p \nabla \cdot \boldsymbol{v} - \nabla \cdot \boldsymbol{h} + S, \quad (2.15)$$

$$\frac{\partial \boldsymbol{B}}{\partial t} = \nabla \times (\boldsymbol{v} \times \boldsymbol{B}) + \eta \nabla^2 \boldsymbol{B}, \tag{2.16}$$

along with an equation of state, for example $p = k_B \rho T/m$ where $T$ is the temperature and $m$ is the average mass of a particle in the plasma, and

$$\nabla \cdot \boldsymbol{B} = 0, \qquad \nabla \times \boldsymbol{B} = \mu_0 \boldsymbol{j}, \qquad \boldsymbol{E} = -\boldsymbol{v} \times \boldsymbol{B} + \boldsymbol{j}/\sigma. \tag{2.17}$$

These equations can be used to describe plasmas provided certain conditions are met. The length scale for the plasma must be much greater than internal length scales, such as the mean free path, so that the plasma can be treated as a continuum. In a similar way, the time scale for variations within the system must be much larger than the time between ion collisions, the plasma must be treated as a single fluid and the non-relativistic condition, $v_0 \ll c$, applies (Priest, 2000).

A useful parameter that can be obtained from the induction equation (equation (2.12)) is the magnetic Reynolds number, which can be defined as a dimensionless ratio of the convective and diffusive terms in the equation. The magnetic Reynolds number, $R_m$, can be defined as

$$R_m = \frac{|\nabla \times (\boldsymbol{v} \times \boldsymbol{B})|}{\eta |\nabla^2 \boldsymbol{B}|} \approx \frac{v_0 B_0/l_0}{\eta B_0/l_0^2} = \frac{v_0 l_0}{\eta}. \tag{2.18}$$

The number $R_m$ is a measure of the strength of the coupling between the flow and the magnetic field (Priest, 2000). In cases where $R_m \ll 1$ the induction equation reduces to

$$\frac{\partial \boldsymbol{B}}{\partial t} = \eta \nabla^2 \boldsymbol{B}, \tag{2.19}$$

which is a diffusion equation and implies that over lengths $l_0$, the magnetic field variations are destroyed over a diffusion time scale, $\tau_d = l_0^2/\eta$. Plasmas with $R_m \ll 1$ are usually found in a laboratory. However, plasma in the solar corona has $R_m \gg 1$. In this limit the induction equation reduces to

$$\frac{\partial \boldsymbol{B}}{\partial t} = \nabla \times (\boldsymbol{v} \times \boldsymbol{B}) \tag{2.20}$$

and the frozen-flux theorem applies. This theorem states that in a perfectly conducting plasma the magnetic field lines move with the plasma. Hence, if

the plasma experiences a force and subsequently moves, the magnetic field lines move with it. When the MHD equations are taken to contain this version of the induction equation, and the terms due to heating and viscosity are removed, they are known as the ideal MHD equations.

Looking again at the right hand side of the equation of motion, (2.14), and assuming there is no viscosity this leaves $\boldsymbol{F}$ as the sum of the contributions from the gravitational force, $\rho\boldsymbol{g}$, and the Lorentz force, $\boldsymbol{j} \times \boldsymbol{B}$. The importance of the Lorentz force can be estimated by comparing it to the pressure gradient term, $-\nabla p$. By using $\boldsymbol{j} = \nabla \times \boldsymbol{B}/\mu_0$ and a vector identity, the Lorentz force can be written as

$$\boldsymbol{j} \times \boldsymbol{B} = (\nabla \times \boldsymbol{B}) \times \boldsymbol{B}/\mu_0 = (\boldsymbol{B} \cdot \nabla)\boldsymbol{B}/\mu_0 - \nabla(B^2/2\mu_0). \tag{2.21}$$

The first term on the right hand side of this equation represents magnetic tension while the second term represents magnetic pressure. The ratio between the plasma pressure and the magnetic pressure gives a parameter, $\beta = 2\mu_0 p/B^2$, called the plasma beta. If $\beta \gg 1$ this implies that the pressure gradient is more important than the Lorentz force and if $\beta \ll 1$ the opposite case is true. In solar applications it is found that in the photosphere $\beta \gtrsim 1$, while in the corona $\beta \ll 1$.

## 2.2 Waves in a Magnetized Plasma

If a system in equilibrium is perturbed, there is a chance that the resulting disturbance will propagate as a wave. On the Sun there are many different types of waves and studying them can provide much information about the medium they are propagating through. Helioseismology studies the oscillations of the solar interior, which has provided detailed observations of the structure of the solar interior and revealed the presence of the tachocline between the radiative and convection zones. As discussed in section 1.3, coronal seismology studies the oscillations of the Sun's atmosphere and can give information about the density scale height and magnetic field strength in the corona (Chaplin and Ballai, 2005).

In a plasma a wave can propagate in one of three ways, whereas in a gas a

wave can only propagate as a sound wave because the only force present that can act to restore equilibrium in a gas is the force due to the gas pressure. However, the magnetic field in a plasma introduces two additional restoring forces, the magnetic tension and the gradient of the magnetic pressure. When magnetic tension acts as the restoring force, Alfvén waves propagate. Alfvén waves propagate along magnetic field lines at a speed $v_A = B(\mu_0\rho)^{-1/2}$ and, in the case of an infinite uniform plasma, they are transverse waves, which displace the field lines in a direction perpendicular to the direction of propagation. If the magnetic and plasma pressures act together as restoring forces this results in magnetoacoustic waves. There are two types of magnetoacoustic waves, slow and fast. The slow magnetoacoustic waves are subsonic and travel along, or at small angles to, the field lines while the fast wave can travel in any direction (Priest, 2000).

Waves are usually investigated using the ideal MHD equations with the energy equation in the form

$$\frac{D}{Dt}(p\rho^{-\gamma}) = 0, \tag{2.22}$$

where

$$\frac{D}{Dt} = \frac{\partial}{\partial t} + \boldsymbol{v}\cdot\nabla, \tag{2.23}$$

is the convective derivative. The background state is then perturbed using quantities such as $\rho = \rho_0(\boldsymbol{r}) + \rho_1(\boldsymbol{r},t)$, $p = p_0(\boldsymbol{r}) + p_1(\boldsymbol{r},t)$, $\boldsymbol{v} = \boldsymbol{v}_0(\boldsymbol{r}) + \boldsymbol{v}_1(\boldsymbol{r},t)$ and $\boldsymbol{B} = \boldsymbol{B}_0(\boldsymbol{r}) + \boldsymbol{B}_1(\boldsymbol{r},t)$. The zeroth order terms represent the background quantities, which are usually constant and $\boldsymbol{v}_0$ is often taken to be zero. The first order terms are the perturbations to the initial state and are assumed to be small. This assumption allows the equations to be linearized by ignoring terms which are non-linear in these small quantities. This gives the set of linear ideal MHD equations as

$$\frac{\partial\rho_1}{\partial t} + \nabla\cdot(\rho_0\boldsymbol{v}_1) = 0, \tag{2.24}$$

$$\rho_0\frac{\partial\boldsymbol{v}_1}{\partial t} = -\nabla p_1 + ((\nabla\times\boldsymbol{B}_0)\times\boldsymbol{B}_1 + (\nabla\times\boldsymbol{B}_1)\times\boldsymbol{B}_0)/\mu_0, \tag{2.25}$$

$$\frac{\partial\boldsymbol{B}_1}{\partial t} = \nabla\times(\boldsymbol{v}_1\times\boldsymbol{B}_0), \tag{2.26}$$

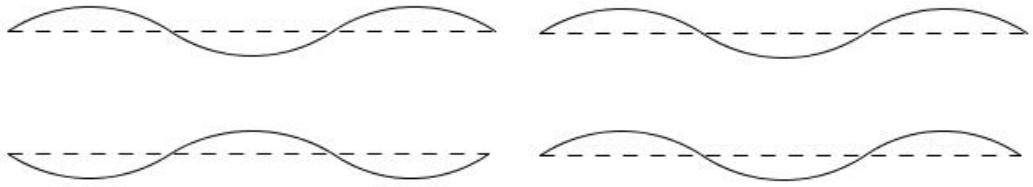

(a) (b)

Figure 2.1: (a) Sausage and (b) kink mode of a magnetoacoustic wave.

$$\nabla \cdot \boldsymbol{B}_1 = 0, \tag{2.27}$$

$$p_1 = c_s^2 \rho_1, \tag{2.28}$$

where the sound speed $c_s = (\gamma p_0/\rho_0)^{1/2}$. Note that the second term on the right-hand side of equation (2.25) usually vanishes because $\boldsymbol{B}_0$ is generally constant. However, we have kept it here because it will be needed in later chapters. Combining these equations and then looking for plane wave solutions, which have a Fourier form, e.g.

$$\boldsymbol{v}_1 = v_1 \exp(i(k_x x + k_y y + k_z z + \omega t)), \tag{2.29}$$

where $\boldsymbol{k} = (k_x, k_y, k_z)$ is a wave vector and $\omega$ is the frequency, should allow a dispersion relation, $\omega = \omega(\boldsymbol{k})$, to be found. The dispersion relation can then be examined further to find possible propagation characteristics for waves in the system.

The linearized MHD equations depend on eight variables: three components of the magnetic field, three components of the velocity, density and pressure. In the case of a uniform plasma the variables split into two uncoupled sets. If we assume that $\boldsymbol{B}_0$ and $\boldsymbol{k}$ are in the $xz$-plane, then the variables $v_y$ and $B_y$ describe Alfvén waves, and the remaining six variables describe magnetoacoustic waves. As the Alfvén waves are not influenced by pressure or density this implies that they are incompressible. The dispersion relation for the magnetoacoustic waves has two solutions, which correspond to slow and fast waves.

In the case of a non-uniform plasma, the equilibrium quantities depend on position. However, in some cases a magnetic field can structure the plasma in such a way that the equilibrium parameters can be taken as constant on either

side of a boundary. This simplifies the problem but gives two solutions, one for each side of the boundary. Assuming there are no flows in the system and the equilibrium magnetic field is parallel to the interface, the total pressure and displacement should be continuous across the interface and this information can be used to specify boundary conditions for the problem. The solution should be chosen so that the amplitude of the oscillation vanishes with distance from the boundary. This requires that the solution is evanescent. In structures, such as a slab, which have a finite width and therefore two boundaries, the solution in the region between these boundaries can either be evanescent or oscillatory and is called a surface or body wave, respectively. The solution outside the slab should be evanescent. For any oscillations which occur far from, and do not encounter, the boundary, the solution should be equivalent to that of a uniform medium.

In non-uniform plasmas with a slab or tube geometry, the magnetoacoustic waves modes can also be classified as sausage or kink oscillations. Sausage modes are symmetric about the axis, which remains fixed, and the boundaries oscillate as shown in figure 2.1(a). Kink modes are antisymmetric and here the cross section retains a constant size and shape, while the plasma moves with respect to its equilibrium position as shown in figure 2.1(b).

## 2.3 Kink Oscillations in a Cylindrical Tube

In this thesis, we discuss kink oscillations of a coronal loop. As discussed in section 1.2, the first theoretical models of a coronal loop approximated the loop as a straight magnetic cylinder. Here we will consider the kink modes obtained from such a model before moving on to study kink modes of a helically shaped loop in subsequent chapters.

Oscillations in a magnetic cylinder were previously studied by Ryutov and Ryutova (1976), Edwin and Roberts (1983) and many others. In general, the equilibrium state is taken to be a straight homogeneous cylinder of length $L$ and radius $a$, with the magnetic field directed along the cylinder (see figure 2.2). We use cylindrical coordinates $r, \theta, z$ with the cylinder centred on the $z$-axis. The density inside and outside the cylinder are assumed to be constant and are denoted by $\rho_i$ and $\rho_e$ respectively. Since we will be considering magnetic tubes

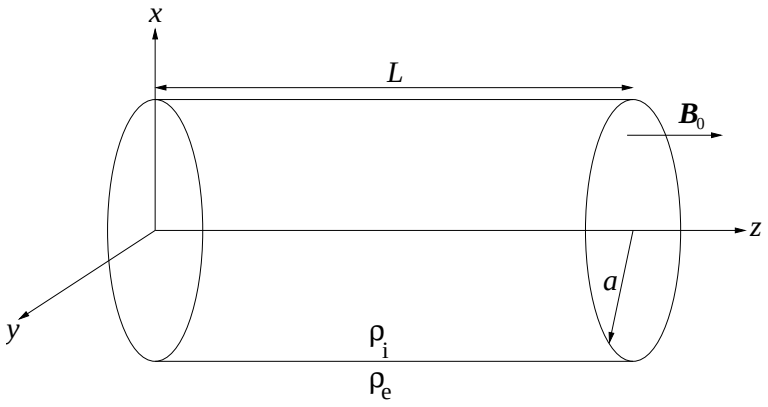


Figure 2.2: The equilibrium state of a straight homogeneous magnetic cylinder.

in the corona, we can make the following approximation. In the corona, the magnetic pressure is much greater than the plasma pressure. This leads us to set the plasma pressure $p = 0$, which is a method known as the cold plasma approximation.

We now consider the linearized ideal MHD equations, given in equations (2.25) to (2.26), and introduce the displacement vector $\boldsymbol{\xi}$ by using the following expression:

$$\boldsymbol{v}_1 = \frac{\partial \boldsymbol{\xi}}{\partial t}. \tag{2.30}$$

This leads to

$$\rho_1 \frac{\partial^2 \boldsymbol{\xi}}{\partial t^2} = \frac{1}{\mu_0} \left( (\nabla \times \boldsymbol{B}_0) \times \boldsymbol{b} + (\nabla \times \boldsymbol{b}) \times \boldsymbol{B}_0 \right), \tag{2.31}$$

$$\boldsymbol{b} = \nabla \times (\boldsymbol{\xi} \times \boldsymbol{B}_0), \tag{2.32}$$

where we have renamed $\boldsymbol{B}_1 = \boldsymbol{b}$. Since the magnetic field is directed along the loop, we have $\boldsymbol{B}_0 = B_0 \hat{\boldsymbol{z}}$, where $B_0$ is constant, and hence equation (2.31) reduces to

$$\rho_1 \frac{\partial^2 \boldsymbol{\xi}}{\partial t^2} = \frac{1}{\mu_0} \left( (\nabla \times \boldsymbol{b}) \times \boldsymbol{B}_0 \right). \tag{2.33}$$

The components of this equation are:

$$\rho_1 \frac{\partial^2 \xi_r}{\partial t^2} = \frac{B_0}{\mu_0} \frac{\partial b_r}{\partial z} - \frac{\partial P}{\partial r}, \tag{2.34}$$

$$\rho_1 \frac{\partial^2 \xi_\theta}{\partial t^2} = \frac{B_0}{\mu_0}\frac{\partial b_\theta}{\partial z} - \frac{1}{r}\frac{\partial P}{\partial \theta}, \tag{2.35}$$

$$\frac{\partial^2 \xi_z}{\partial t^2} = 0, \tag{2.36}$$

where we have introduced the magnetic pressure perturbation $P = B_0 b_z/\mu_0$. The components of the induction equation (4.27) are

$$b_r = B_0 \frac{\partial \xi_r}{\partial z}, \tag{2.37}$$

$$b_\theta = B_0 \frac{\partial \xi_\theta}{\partial z}, \tag{2.38}$$

$$P = -\frac{B_0^2}{\mu_0 r}\left(\frac{\partial (r\xi_r)}{\partial r} + \frac{\partial \xi_\theta}{\partial \theta}\right). \tag{2.39}$$

Next, we take all variables proportional to $\exp(i(-\omega t + m\theta + kz))$ and set $m = 1$, which corresponds to kink modes. Therefore the above equations reduce to:

$$(\omega^2 - v_A^2 k^2)\xi_r = \frac{1}{\rho_0}\frac{dP}{dr} \tag{2.40}$$

$$(\omega^2 - v_A^2 k^2)\xi_\theta = \frac{iP}{r\rho_0} \tag{2.41}$$

$$-\omega^2 \xi_z = 0 \quad \Rightarrow \quad \xi_z = 0 \tag{2.42}$$

$$b_r = iB_0 k \xi_r \tag{2.43}$$

$$b_\theta = iB_0 k \xi_\theta \tag{2.44}$$

$$P = -\frac{B_0^2}{\mu_0 r}\left(\frac{d(r\xi_r)}{dr} + i\xi_\theta\right). \tag{2.45}$$

These can be combined to give

$$\frac{d^2 P}{dr^2} + \frac{1}{r}\frac{dP}{dr} + P\left(\kappa^2 - \frac{1}{r^2}\right) = 0, \tag{2.46}$$

where $\kappa^2 = \omega^2 v_A^2 - k^2$. This equation is the modified Bessel equation and describes magnetoacoustic wave modes. The equation can be solved for the regions both inside and outside the tube and must satisfy several conditions at the boundary. The first of these conditions is that the magnetic pressure perturbation must be continuous at the boundary. The same applies for the

component of the plasma displacement which is perpendicular to the boundary. These conditions equate to $P_i = P_e$ and $\xi_{ri} = \xi_{re}$ at $r = a$, where a subscript $i$ or $e$ refers to the region inside or outside the loop, respectively. We also need to ensure that the solution vanishes with distance from the tube boundary. Applying these boundary conditions to the solution of equation (2.46), results in two dispersion relations: the first, in equation (2.47), represents surface waves and the second in equation (2.48), represents body waves (Edwin and Roberts (1983), see also: Nakariakov and Verwichte, 2005; Ruderman and Erdélyi, 2009).

$$\rho_{1i}(k^2 v_{Ai}^2 - \omega^2)\kappa_e \frac{K_1'(\kappa_e a)}{K_1(\kappa_e a)} = \rho_{1e}(k^2 v_{Ae}^2 - \omega^2)\kappa_i \frac{I_1'(\kappa_i a)}{I_1(\kappa_i a)}, \tag{2.47}$$

$$\rho_{1i}(k^2 v_{Ai}^2 - \omega^2)\kappa_e \frac{K_1'(\kappa_e a)}{K_1(\kappa_e a)} = \rho_{1e}(k^2 v_{Ae}^2 - \omega^2)|\kappa_i| \frac{J_1'(|\kappa_i| a)}{J_1(|\kappa_i| a)}. \tag{2.48}$$

Here, $I_1$, $J_1$ and $K_1$ are modified Bessel functions and a dash denotes a derivative with respect to the argument of the Bessel function. Under coronal conditions ($v_{Ae} > v_{Ai}$), there are two classes of body wave that can occur, but no surface waves. Equation (2.48) describes many kink waves. All of these except one have a cut-off wavelength, which is of the order of, or smaller than, the tube radius. Therefore, because the tube length is much larger than the tube radius, these waves can only exist in the loop at high harmonics. The kink mode which does not have a cut-off wavelength can exist at all harmonics, including the fundamental mode. This kink mode is known as the global kink mode and travels at the kink speed,

$$c_k = \left( \frac{2B_0^2}{\mu_0(\rho_i + \rho_e)} \right)^{1/2}. \tag{2.49}$$

Due to the symmetrical nature of the cylindrical model, there is no preferred direction for the kink oscillations and therefore they are considered to be degenerate. This is in contrast to the distinct horizontal and vertical kink oscillations that can occur when a curved loop is considered.

# Chapter 3

# A Non-Planar Coronal Loop Model

In chapter 1 we discussed several coronal loop models, which all considered loops whose axis lay in a plane. Here we investigate a loop model which is not confined to a plane and has non-zero curvature and torsion. We have chosen to define the loop such that it has helical geometry and we also include density stratification along the loop.

In section 3.1 we introduce the equilibrium for our loop model, while in section 3.2 we examine how the geometry of our model relates to observations of non-planar loops, with an aim of establishing which loops are best described by our model.

## 3.1 Equilibrium

We start by introducing Cartesian coordinates $x, y, z$, with the $z$-axis in the vertical direction, and cylindrical coordinates $\varpi, \varphi, x$, with the cylinder axis parallel to the $x$-axis. The Cartesian and cylindrical coordinates are related by

$$x = x, \qquad y = \varpi \cos\varphi, \qquad z = \varpi \sin\varphi. \tag{3.1}$$

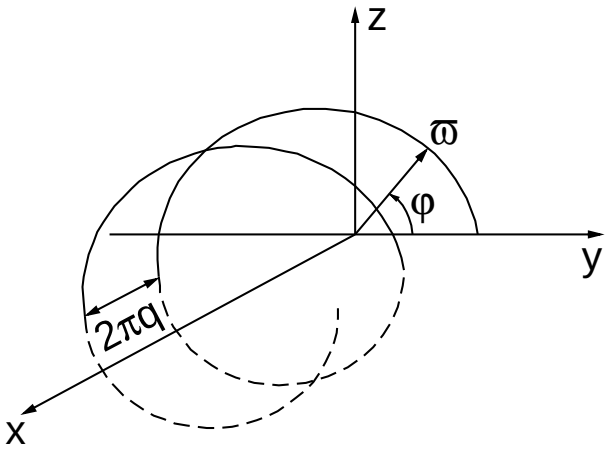


Figure 3.1: A typical magnetic field line is shown. Parts of this line that are above the $xy$-plane are shown by solid lines, and those below the $xy$-plane are shown by dashed lines.

We define a magnetic field $\boldsymbol{B}$ with components given by

$$B_x = \frac{q^2 B_0}{q^2 + \varpi^2}, \qquad B_\varpi = 0, \qquad B_\varphi = \frac{q\varpi B_0}{q^2 + \varpi^2}, \tag{3.2}$$

where $B_0$ and $q$ are constants, and $q$ is related to the pitch of the helix. It can be shown that

$$\nabla \times \boldsymbol{B} = \frac{2q\boldsymbol{B}}{q^2 + \varpi^2}. \tag{3.3}$$

It follows from this result that the magnetic field $\boldsymbol{B}$ is force-free and can be used as an equilibrium magnetic field if we adopt the cold plasma approximation.

In cylindrical coordinates the equation of a magnetic field line is

$$\frac{dx}{B_x} = \frac{\varpi\, d\varphi}{B_\varphi} = \frac{d\varpi}{0}, \tag{3.4}$$

which implies that $\varpi$ is constant and

$$\frac{dx}{d\varphi} = \frac{\varpi B_x}{B_\varphi} = q \quad \Rightarrow \quad x = q\varphi + x_0, \tag{3.5}$$

where $x_0$ is a constant. Similarly, in Cartesian coordinates we can write

$$\frac{dx}{B_x} = \frac{dy}{-B_\varphi \sin\varphi} = \frac{dz}{B_\varphi \cos\varphi}, \tag{3.6}$$

which leads to

$$\frac{dy}{dz} = -\tan\varphi = -\frac{z}{y} \quad \Rightarrow \quad y^2 + z^2 = \varpi_0^2. \tag{3.7}$$

Hence we see that the projection of the field line on the $yz$-plane is a circle of radius $\varpi_0$ centred at the origin. From equations (3.5) and (3.7) we find that the parametric equations of the magnetic field lines are given by

$$x = q\varphi + x_0, \qquad y = \varpi_0 \cos\varphi, \qquad z = \varpi_0 \sin\varphi. \tag{3.8}$$

Therefore the magnetic field lines are helical and all have the same pitch equal to $2\pi q$. Each magnetic field line is invariant under the helical space transformation defined by

$$\varphi \mapsto \varphi + \tilde{\varphi}, \qquad x \mapsto x + q\tilde{\varphi}, \tag{3.9}$$

where $\tilde{\varphi}$ is an arbitrary constant. The magnitude of the magnetic field is

$$|\boldsymbol{B}| = B = \frac{qB_0}{\sqrt{q^2 + \varpi^2}}. \tag{3.10}$$

Since $\varpi$ is constant for each magnetic field line, the magnitude is also constant along each field line. The magnetic field lines are frozen in the dense photospheric plasma at $z = z_0$. A typical magnetic field line can be seen in figure 3.1.

One of the magnetic field lines corresponding to $x_0 = 0$ and $\varpi_0 = R > |z_0|$ is chosen to be the magnetic loop axis. Its equation is

$$x = q\varphi, \qquad y = R\cos\varphi, \qquad z = R\sin\varphi. \tag{3.11}$$

The loop is defined to be part of the first turn of the helical field line, and the loop footpoints are located at $\varphi = \varphi_0$ and $\varphi = \pi - \varphi_0$, where $\varphi_0 = \arcsin(z_0/R)$.

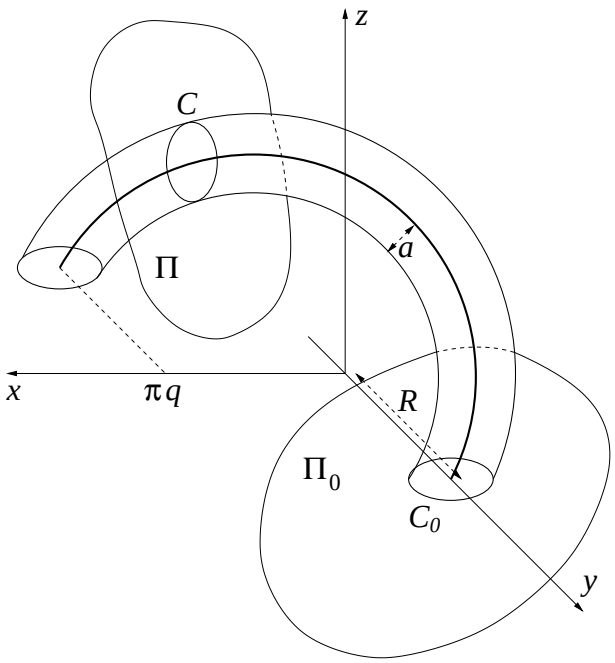


Figure 3.2: A sketch of the equilibrium state. The axis of the magnetic loop is shown by the thick line.

The loop axis crosses the plane $z = z_0$ at points with the Cartesian coordinates

$$\left(q\varphi_0, \sqrt{R^2 - z_0^2},\, z_0\right), \qquad \left(q(\pi - \varphi_0),\, -\sqrt{R^2 - z_0^2},\, z_0\right), \tag{3.12}$$

and the loop axis (or its extension if $z_0 > 0$) crosses the $xy$-plane at the point $(0, R)$. We now take the plane $\Pi_0$ orthogonal to the loop axis (or its extension) at this point and consider a circle $\mathcal{C}_0$ of radius $a$ centred at $(0, R)$, $a \ll R$ (see figure 3.2). The magnetic field lines crossing the plane $\Pi_0$ at points on the circle $\mathcal{C}_0$ form the tube boundary. As mentioned above, any magnetic field line is invariant under the helical space transformation defined by equation (3.9). In particular, this implies that the magnetic field line containing the tube axis is mapped onto itself. Since the helical transformation is an orthogonal transformation, it maps the plane $\Pi_0$ onto a plane $\Pi$ that is orthogonal to the loop axis at the point of their intersection. The circle $\mathcal{C}_0$ is mapped onto a circle $\mathcal{C}$ of radius $a$, in the plane $\Pi$, centred at the point of intersection of $\Pi$ with the loop axis. Since any magnetic field line is mapped onto itself, any point on $\mathcal{C}$ is also on the tube boundary. Hence, $\mathcal{C}$ is the intersection of $\Pi$ with the

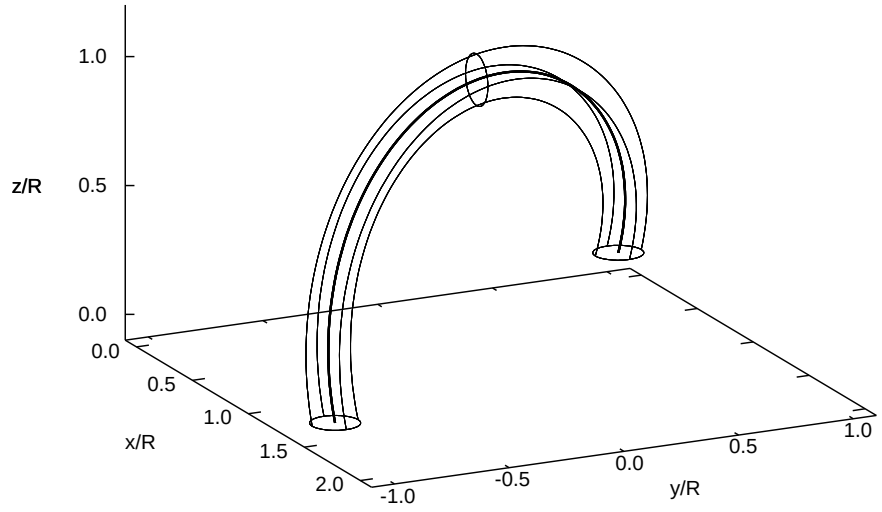


Figure 3.3: Equation (3.8) has been used to plot several field lines which form a loop with $q/R = 0.5$ and $a/R = 0.1$. The loop axis, which is represented by the thick arc, and four field lines that are on the loop boundary are shown. Circles have been added at the footpoints and apex to illustrate the constant loop cross-section.

loop boundary, which implies that the loop cross-section is a circle of radius $a$ centred at the loop axis for all points along the axis. An example of a loop showing individual field lines on the tube boundary can be seen in figure 3.3.

The curvature, $\kappa$, and torsion, $\tau$, of the loop axis can be found using

$$\kappa = \frac{|\boldsymbol{X}' \times \boldsymbol{X}''|}{|\boldsymbol{X}'|^3}, \qquad \tau = \frac{|\boldsymbol{X}' \times \boldsymbol{X}''| \cdot \boldsymbol{X}'''}{|\boldsymbol{X}' \times \boldsymbol{X}''|^2}, \tag{3.13}$$

where $\boldsymbol{X} = (x, y, z)$ is defined using the parametric representation of the loop axis given in equation (3.11) and a dash denotes a derivative with respect to $\varphi$. On evaluation of equation (3.13) it is found that

$$\kappa = \frac{R}{R^2 + q^2} = \frac{1}{R(1 + \gamma^2)}, \tag{3.14}$$

and

$$\tau = \frac{q}{R^2 + q^2} = \frac{\gamma}{R(1 + \gamma^2)}. \tag{3.15}$$

Here, we have introduced the non-planarity parameter $\gamma = q/R$, which can be

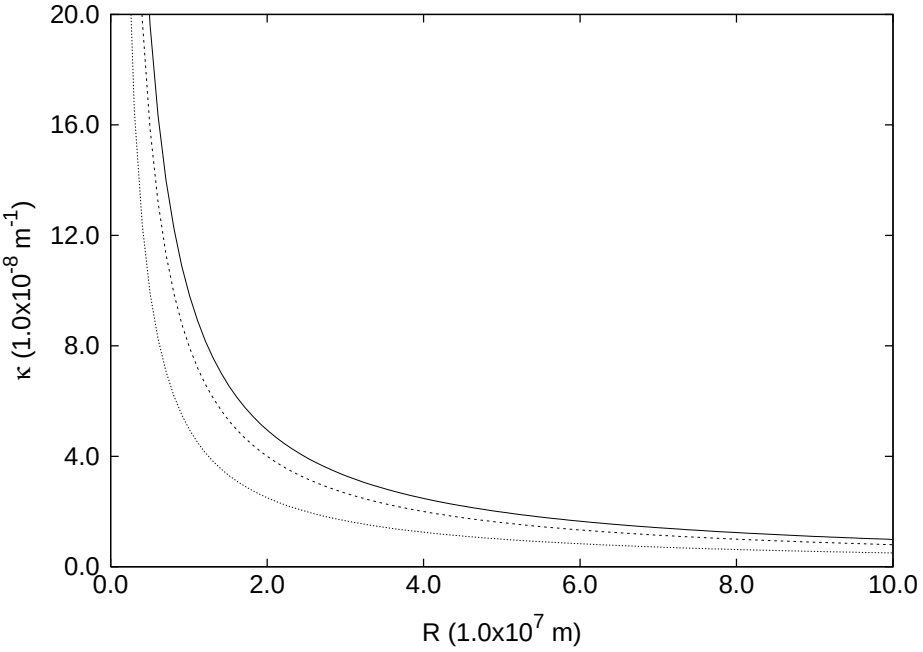


(a)

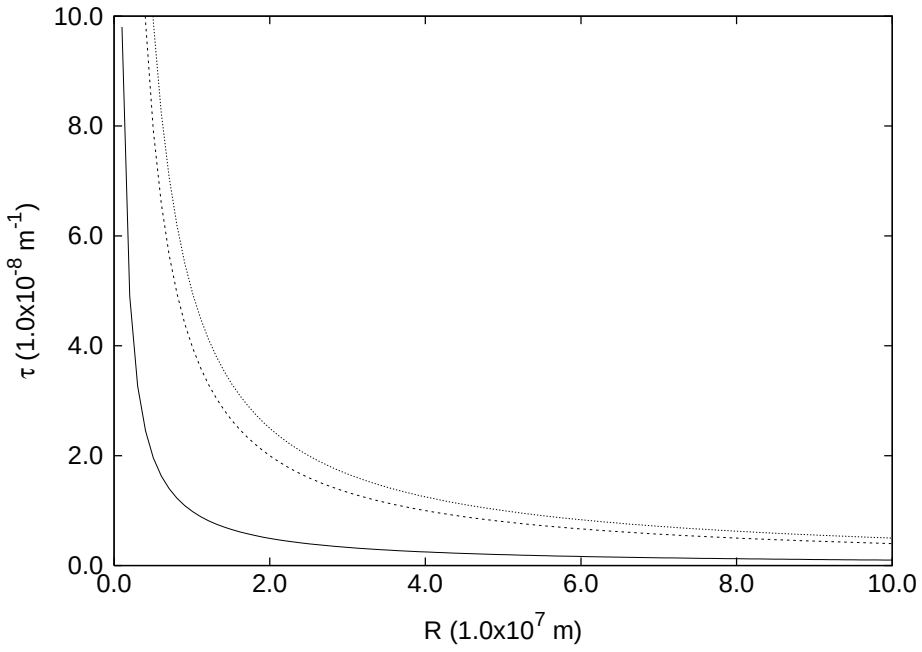


(b)

Figure 3.4: The dependence of the (a) curvature, $\kappa$, and (b) torsion, $\tau$, on $R$ and $\gamma$. In both figures, the solid, dashed and dotted lines correspond to $\gamma = 0.1$, 0.5 and 1, respectively.

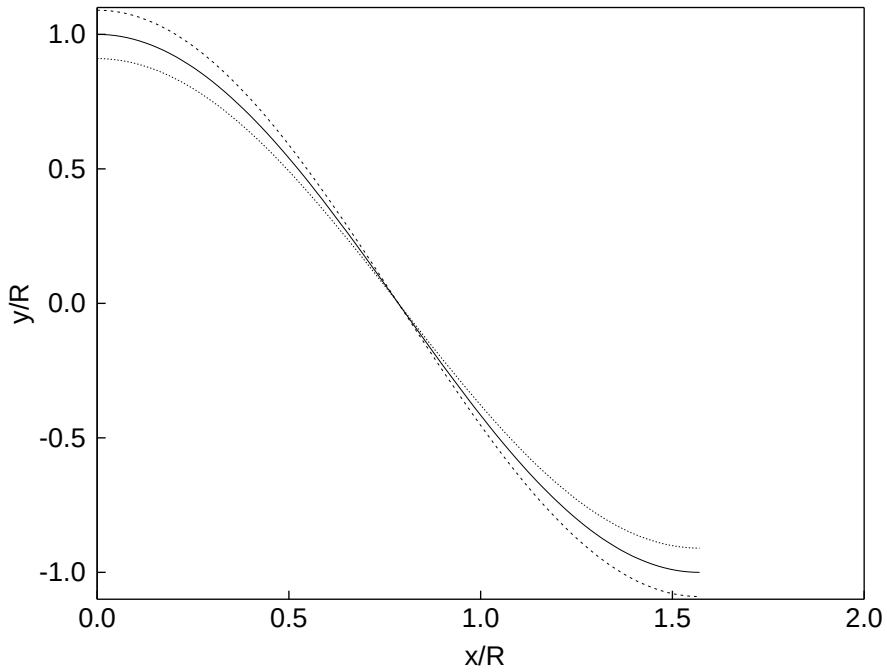


Figure 3.5: Equation (3.8) has been used to plot several field lines which form a loop with $q/R = 0.5$ and $a/R = 0.09$. Their projections on the $xy$-plane are shown. The dashed and dotted lines are field lines on the tube boundary and can be seen to twist around the loop axis, which is represented by the solid line.

used to measure the non-planarity of a loop and will be discussed further in section 3.2. Figure 3.4 shows how the curvature and torsion vary with $R$ and $\gamma$. We see that, as the non-planarity of a loop is increased, the curvature decreases and the torsion increases. We should point out that there is a clear distinction between the loop torsion and twist. The loop torsion is related to the shape of the loop axis and measures the loop non-planarity. The twist is related to the behaviour of the magnetic field lines in the vicinity of the loop axis. A straight loop is twisted if the magnetic field lines are helical in the vicinity of its axis. In the case of a straight loop, magnetic twist creates an electrical current along the loop. We can use this relation between magnetic twist and electrical current to distinguish between twisted and untwisted curved magnetic loops, and say that the loop is twisted if there is an electrical current parallel to the loop axis and untwisted otherwise. Since the current density $\boldsymbol{j} = \nabla \times \boldsymbol{B}/\mu_0$, it follows from equation (3.3) that there is an electrical current parallel to the loop axis

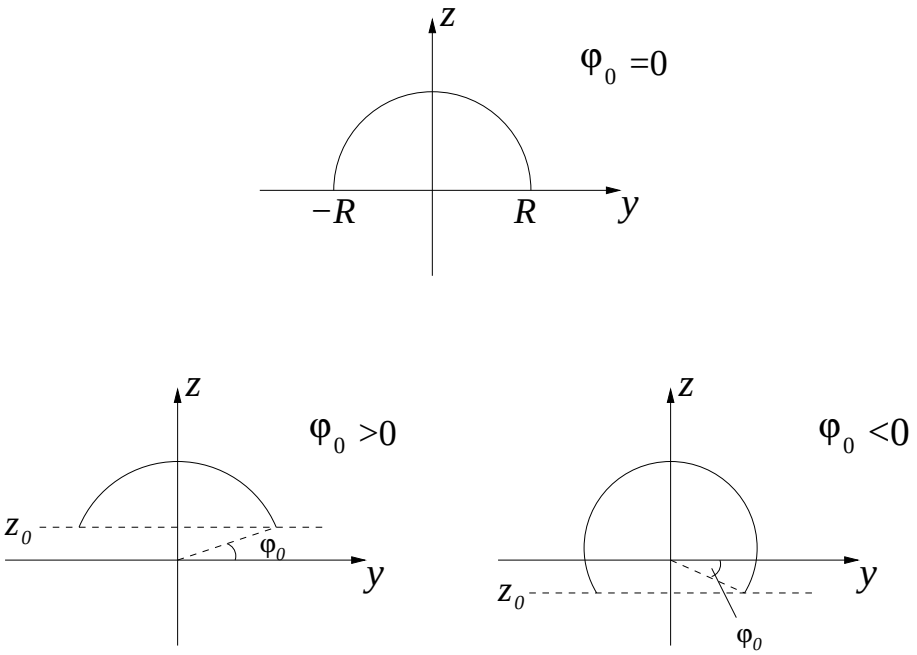


Figure 3.6: The projection of the loop axis on the $yz$-plane.

in our model. Hence, in the equilibrium we consider here, the magnetic loop is twisted (see figure 3.5).

The plasma density is equal to $\rho_i$ inside the loop and $\rho_e$ outside. We consider a stratified atmosphere, hence both $\rho_i$ and $\rho_e$ can vary along the loop, but they do not vary in the directions perpendicular to the loop axis.

We obtain a particular case of a loop with the shape of a half-torus if we take $q = 0$ and $\varphi_0 = 0$. The kink oscillations of such a loop have been studied by Van Doorsselaere et al. (2004) analytically and Terradas et al. (2006) numerically as discussed in section 1.2. However, we should point out that, in order to obtain a non-zero magnetic field in a planar loop, we would have to take $B_0 \to \infty$ simultaneously with $q \to 0$ in such a way that $qB_0$ is constant. For loops with $\varphi_0 \neq 0$ and $q \geq 0$ the projection of the loop axis on the $yz$-plane is more or less than a semicircle if $\varphi_0$ is less than or greater than zero, respectively. The projection of a loop on the $xy$-plane resembles the letter S, leading to non-planar loops often being described as S-shaped loops (see figures 3.5 and 3.7).

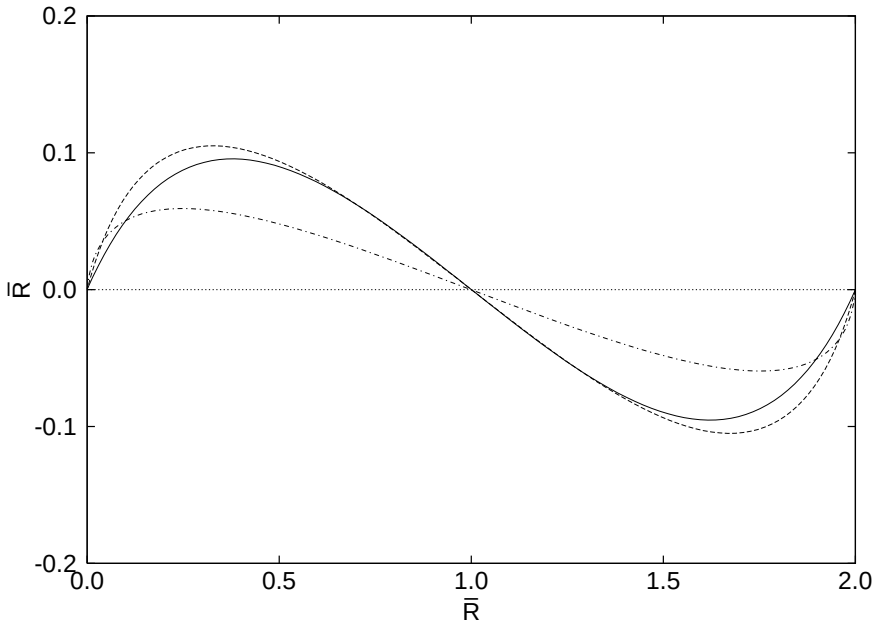


Figure 3.7: Projections of the loop axis on the $xy$-plane, for loops with $\gamma \neq 0$. Here $z_0 = 0$ and the solid, dashed and dashed-dotted lines correspond to $\gamma = 1.0$, 0.6 and 0.2, respectively. The distances on the figure are shown to provide scale, and are given in units of the half-distance between the footpoints, $\bar{R} = R\sqrt{1 + \pi^2\gamma^2/4}$.

## 3.2 Comparison with Non-Planar Loop Observations

Before proceeding with the main analysis, it is useful to compare our loop model with observations of non-planar loops. To do this, we examine the reconstructed coronal loop geometries found by Aschwanden et al. (2008) and Aschwanden (2009), which can be seen in figures 3.8 and 3.9, respectively. The projections of the loop reconstructions shown in the left and right columns clearly show that the loops do not lie in a plane, some to a larger extent than others.

For loops described by our model, we can measure the variation in non-planarity by using the non-planarity parameter $\gamma = q/R$, which was introduced in equation (3.14). If $\gamma = 0$ then the loop is planar with its axis lying in the $yz$-plane. For loops with $\gamma \neq 0$, the loop axis is not confined to a plane and examples of their projections on the $xy$-plane are shown in figure 3.7. Figure 3.7

shows that the loops appear to be S-shaped when viewed from above. This shape can also be seen in the right-hand column of some of the loop reconstructions shown in figures 3.8 and 3.9. It is interesting to note that the S-shapes in figure 3.8 curve in the opposite direction to the S-shapes in figure 3.9. This suggests that non-planar coronal loops can be both left- and right-handed. The model introduced here describes a right-handed helical loop.

The loops shown in figure 3.7 were all plotted under the assumption that $z_0 = 0$, which implies that they have a semicircular projection on the $yz$-plane. However, coronal loops are not necessarily this shape. Loops with $z_0 < 0$ could provide a better match for loops such as examples 2 and 7 in figure 3.8, which appear to curve back on themselves when viewed from above. To consider this further, we have plotted several loops with $z_0 < 0$ (see figure 3.10) and found that their shape does resemble some of the loops shown in figure 3.8, particularly when $\gamma \lessapprox 0.2$.

Aschwanden et al. (2008) characterized loop non-planarity by introducing the coplanarity parameter $P_*$. This parameter is equal to the maximum distance of a point on the loop axis from the loop plane, divided by the curvature radius. To define the loop plane for the case of a non-planar loop, Aschwanden et al. (2008) chose the plane which passes through the loop apex and both footpoints. By finding the equivalent of the coplanarity parameter in our geometry, we can relate $\gamma$ to the observed values of $P_*$.

To start, we must find the equation for the loop plane. The Cartesian coordinate of the loop apex is $(\pi q/2, 0, R)$ and for simplicity we will assume that $z_0 = 0$, which implies that the coordinates of the footpoints are $(0, R, 0)$ and $(\pi q, -R, 0)$. The equation of the plane which passes through these three points is

$$2Rx + \pi qy = \pi qR. \tag{3.16}$$

Then, combining this with the parametric form of the loop axis given in equation (3.11), we find that the distance to the loop plane from the loop axis is given by

$$d(\varphi) = \gamma R \, \frac{2\varphi - \pi(1 - \cos\varphi)}{\sqrt{4 + \pi^2\gamma^2}}. \tag{3.17}$$

The maximum distance of the loop axis from the loop plane is equal to the maximum value of $d(\varphi)$ in the range $0 \leq \varphi \leq \pi$. Since we have assumed that

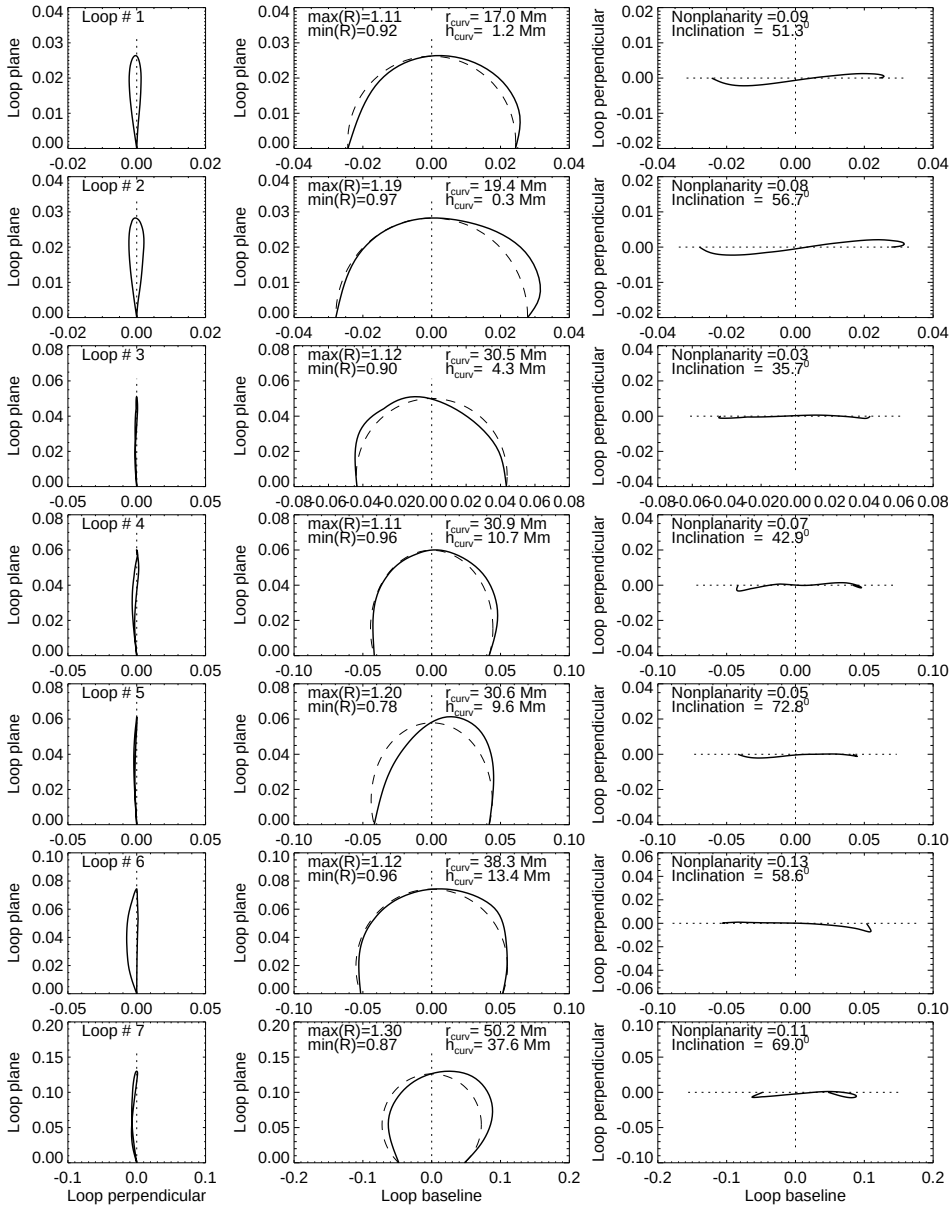


Figure 3.8: Reconstruction of 3D loop geometry by Aschwanden et al. (2008). The figure shows the projections of seven complete loops in the loop plane (middle) and in the orthogonal directions, from the side (left) and the top (right). The loop plane is defined by the two footpoints and the loop top above the midpoint between the footpoints. A circle is also interpolated through these three points in order to visualize the circularity (dashed lines). (This figure is taken from Aschwanden et al. (2008, Fig. 9) and is reproduced by permission of the AAS and M. J. Aschwanden.)

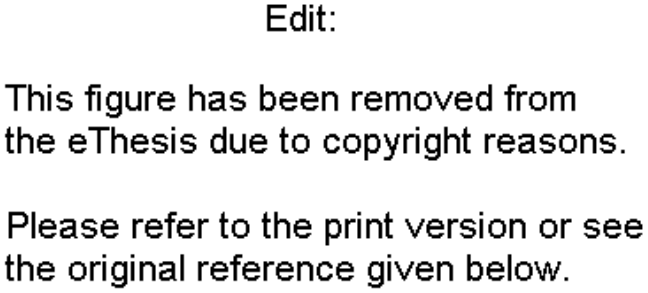


Figure 3.9: Reconstruction of 3D loop geometry by Aschwanden (2009). The figure shows the projections of the loop into three orthogonal planes, which are the same as those defined in figure 3.8. The three rows show three independent trials of manual loop tracings. (This figure is taken from Aschwanden (2009, Fig. 7) and is reproduced in the print version with kind permission from Springer Science+Business Media B.V. and M. J. Aschwanden.)

$z_0 = 0$, the range of variation of $\varphi$ does not include $\varphi_0$. By differentiating the above equation we obtain that the maximum value, $d_M$, occurs at $\varphi = \varphi_M = \arcsin(2/\pi)$ and is equal to

$$d_M = \gamma R \frac{\sqrt{\pi^2 - 4} - 2\arccos(2/\pi)}{\sqrt{4 + \pi^2\gamma^2}}. \tag{3.18}$$

The curvature radius of the loop is equal to $\kappa^{-1}$, where $\kappa$ is the loop curvature, given by equation (3.14). Hence, the curvature radius is equal to $R(1+\gamma^2)$ and we find that

$$P_* = \frac{d_M}{R(1+\gamma^2)} = \gamma \frac{\sqrt{\pi^2 - 4} - 2\arccos(2/\pi)}{(1+\gamma^2)\sqrt{4 + \pi^2\gamma^2}}. \tag{3.19}$$

The dependence of $P_*$ on $\gamma$ is shown in figure 3.11, where we can see that $P_*$ is a non-monotonic function of $\gamma$. As $\gamma$ increases from 0, $P_*$ is seen to increase

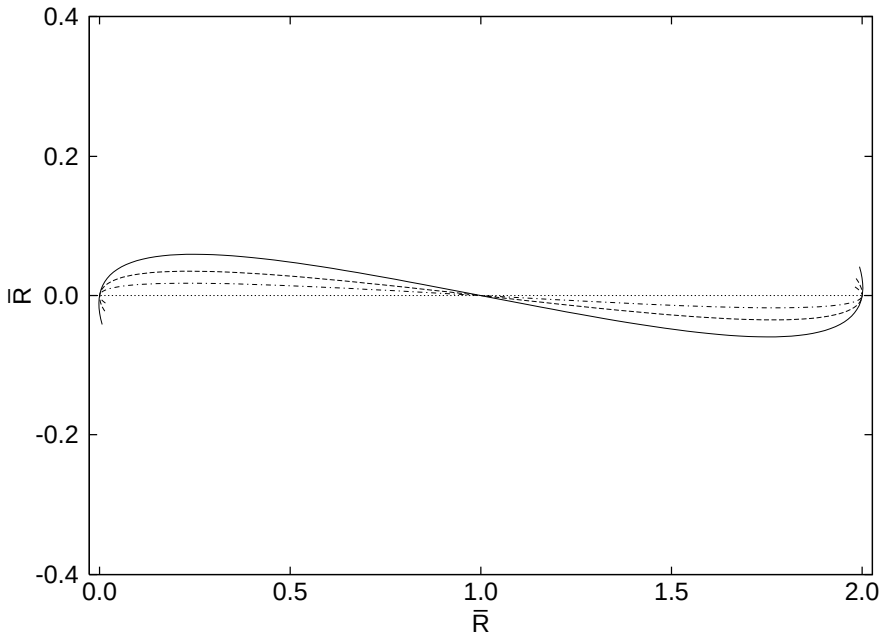


Figure 3.10: Projections of the loop axis on the $xy$-plane, for loops with $\gamma \neq 0$. Here $\varphi_0 = -0.2$, which implies that $z_0 < 0$. The solid, dashed and dashed-dotted lines correspond to $\gamma = 0.2$, 0.1 and 0.05, respectively. The distances on the figure are shown to provide scale and $\bar{R}$ is defined in the same way as for figure 3.7. Note that, since $z_0 \neq 0$, $\bar{R}$ no longer corresponds to the half-distance between the footpoints, but has been used here to allow for an easy comparison with figure 3.7.

monotonically from 0 to a maximum value $P_M$ at $\gamma = \gamma_M$, where

$$\gamma_M = \frac{\sqrt{\sqrt{1+2\pi^2}-1}}{\pi} \approx 0.6, \tag{3.20}$$

and therefore

$$P_M = \frac{\pi\sqrt{\sqrt{1+2\pi^2}-1}\left(\sqrt{\pi^2-4}-2\arccos(2/\pi)\right)}{\left(\pi^2+\sqrt{1+2\pi^2}-1\right)\sqrt{3+\sqrt{1+2\pi^2}}} \approx 0.106. \tag{3.21}$$

After this point $P_*$ decreases monotonically towards 0. This implies that for all $P_* < P_M$ there are two corresponding values of $\gamma$, $\gamma_-$ and $\gamma_+$. Hence, we need to choose which of these is the most appropriate for our model. To do this we consider the ratio of the distance between the loop footpoints and the loop

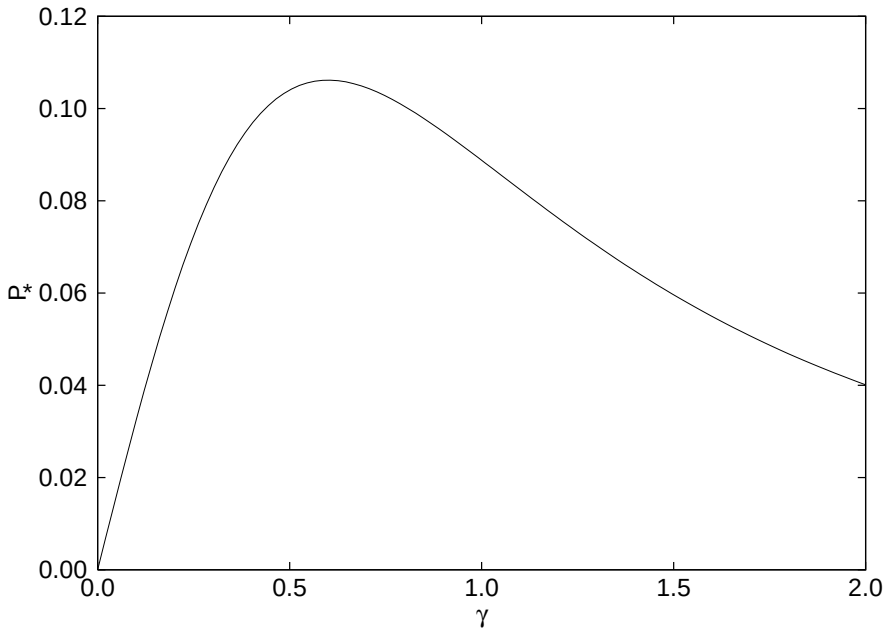


Figure 3.11: The dependence of the coplanarity parameter $P_*$ on $\gamma$.

height. Since we are assuming a loop with a semicircular projection on the $yz$-plane, we know that the loop height is equal to $R$. Then, using the coordinates of the two footpoints, we find that the distance between the loop footpoints is $R\sqrt{4+\pi^2\gamma^2}$. Therefore the ratio of the distance between the footpoints and the loop height is given by $\sqrt{4+\pi^2\gamma^2}$. At $\gamma = \gamma_M$ this is equal to

$$\sqrt{4+\pi^2\gamma_M^2} = \sqrt{3+\sqrt{1+2\pi^2}} \approx 2.75. \tag{3.22}$$

Therefore we find that

$$\begin{aligned} \sqrt{4+\pi^2\gamma_-^2} &\leq \sqrt{3+\sqrt{1+2\pi^2}}, \\ \sqrt{4+\pi^2\gamma_+^2} &\geq \sqrt{3+\sqrt{1+2\pi^2}}. \end{aligned} \tag{3.23}$$

For all coronal loops examined by Aschwanden et al. (2008) and Aschwanden (2009), the ratio of the distance between the loop footpoints and the loop height was smaller than 2.75. Hence, we choose $\gamma_-$. For six of the seven loops studied by Aschwanden et al. (2008), $P_*$ was found to be in the range 0.03 to 0.11 (see figure 3.8). The highest value in this range is approximately equal to $P_M$.

From figure 3.11 we find that the corresponding range for $\gamma_-$ is from 0.09 to 0.6. The remaining loop analysed by Aschwanden et al. (2008) has $P_* = 0.13$. The loop examined by Aschwanden (2009) was analysed three times in order to investigate the errors in the reconstruction method used (see figure 3.9). This loop was found to have a value of $P_*$ in the range 0.16 to 0.21. Both of these loops have $P_* > P_M$, which leads us to conclude that they cannot be reproduced by our model. In particular, the Aschwanden (2009) case, shown in figure 3.9, is highly non-planar and the loop reconstruction shows a strong variation in curvature along the loop. This provides further evidence to support our conclusion, because the helical loop described by our model has constant curvature.

To summarize, we find that our model can reproduce non-planar loops with small or moderate non-planarity. We expect that $\gamma$ is usually smaller than or equal to 0.6, and it is unlikely to exceed one.

# Chapter 4

# Transverse Oscillations of Non-Planar Coronal Loops

In chapter 3 we introduced a new coronal loop model, which features a loop that is not confined to a plane. Next, we move on to consider transverse oscillations of loops described by this model.

In section 4.1 we derive a system of curvilinear coordinates for use with the model, and in section 4.2 the MHD equations are written in terms of this new curvilinear coordinate system. Section 4.3 contains the derivation of the governing equation for kink oscillations of a non-planar loop. In sections 4.4 and 4.5 we discuss the polarization and observational signatures of these oscillations.

## 4.1 Curvilinear Coordinates

It is useful to set up a new coordinate system for use with these helical loops, rather than using the Cartesian or cylindrical coordinates introduced previously. To start, we introduce the small parameter $\varepsilon = a/R$. In what follows we only consider perturbations that decay far from the loop, with the characteristic scale of decay equal to $a$. Hence, we only study the plasma motion inside the loop and in the loop vicinity. As a result of this we only need to define curvilinear coordinates that cover the spatial domain which is elongated in the direction of the loop axis and is the size of a few $a$ in the directions orthogonal to the loop axis.

To obtain the curvilinear coordinate system we first introduce polar coordi-

nates in the $\Pi_0$ plane. It follows from the parametric equation of the loop axis given in equation (3.11), that the vector

$$\begin{aligned} \boldsymbol{l} &= (x'(\varphi), y'(\varphi), z'(\varphi)) \\ &= (q, -R\sin\varphi, R\cos\varphi), \end{aligned} \tag{4.1}$$

is tangent to the loop axis or its extension. Note that in the equation above, a dash denotes a derivative with respect to $\varphi$. At the Cartesian point $(0, R, 0)$ the tangent to the loop axis is $\boldsymbol{l} = (q, 0, R)$ and hence we find the equation of the plane $\Pi_0$ to be

$$qx + Rz = 0. \tag{4.2}$$

We now rotate the axes such that the plane $\Pi_0$ has the equation $z_1 = 0$. This leads to another set of Cartesian coordinates, $x_1, y_1, z_1$, being introduced, which are related to $x, y, z$ by

$$x_1 = \frac{Rx - qz}{\sqrt{R^2 + q^2}}, \qquad y_1 = y, \qquad z_1 = \frac{qx + Rz}{\sqrt{R^2 + q^2}}. \tag{4.3}$$

The $x_1y_1$-plane is equivalent to $\Pi_0$. Therefore we can introduce polar coordinates $r$ and $\theta$ in $\Pi_0$ by relating them to $x_1$ and $y_1$ as follows

$$x_1 = r\cos\theta, \qquad y_1 = R + r\sin\theta. \tag{4.4}$$

In these polar coordinates the equation of circle $\mathcal{C}_0$, of radius $a \ll R$ and centred at $x_1 = 0$, $y_1 = R$ in the plane $\Pi_0$, is $r = a$. Inverting the relations in equation (4.3) we obtain that, for any point $(x, y, z)$ on $\Pi_0$,

$$x = \frac{Rr\cos\theta}{\sqrt{R^2 + q^2}}, \qquad y = R + r\sin\theta, \qquad z = -\frac{qr\cos\theta}{\sqrt{R^2 + q^2}}. \tag{4.5}$$

Note that from here onwards, we do not use the $x_1, y_1, z_1$ coordinate system again and all Cartesian coordinates will refer to the $x, y, z$ coordinate system.

To obtain the curvilinear coordinates of an arbitrary point $(\bar{x}, \bar{y}, \bar{z})$ we do the following: first we take the magnetic field line $\mathcal{L}$ that passes through this point. It intersects the plane $\Pi_0$ at the point with polar coordinates $r, \theta$ (see figure 4.1). These are the first and second curvilinear coordinates of the point $(\bar{x}, \bar{y}, \bar{z})$.

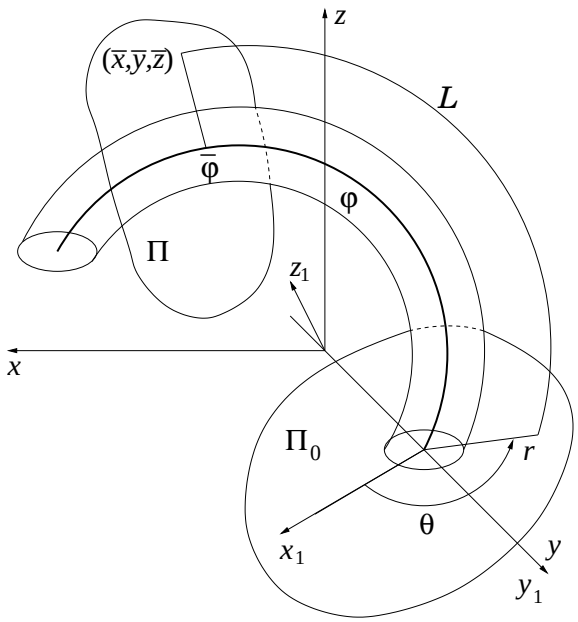


Figure 4.1: A sketch of the equilibrium state. The axis of the magnetic loop is shown by the thick line. Introducing curvilinear coordinates is illustrated.

To obtain the third curvilinear coordinate we take the plane $\Pi$ orthogonal to the loop axis and containing $(\bar{x}, \bar{y}, \bar{z})$. It crosses the loop axis at the point $\varphi = \bar{\varphi}$. Then the curvilinear coordinates of $(\bar{x}, \bar{y}, \bar{z})$ are $(r, \theta, \bar{\varphi})$. Hence, the three coordinates $r$, $\theta$ and $\varphi$ combine to form the new coordinate system that we will use with our helical loop model.

Now we obtain the expressions of $\bar{x}$, $\bar{y}$ and $\bar{z}$ in terms of $r$, $\theta$ and $\bar{\varphi}$. Let $\mathcal{L}$ cross $\Pi_0$ at the point $(x_c, y_c, z_c)$. The coordinates of $(x_c, y_c, z_c)$, in terms of $r$ and $\theta$, can be found using equation (4.5), which leads to

$$x_c = \frac{Rr\cos\theta}{\sqrt{R^2+q^2}}, \qquad y_c = R + r\sin\theta, \qquad z_c = -\frac{qr\cos\theta}{\sqrt{R^2+q^2}}. \tag{4.6}$$

The parametric equation of $\mathcal{L}$ is

$$x = q\varphi' + x_0, \qquad y = \varpi_0\cos\varphi', \qquad z = \varpi_0\sin\varphi', \tag{4.7}$$

where we have used $\varphi'$ to avoid confusing the parameter on $\mathcal{L}$ with $\varphi$, the parameter on the loop axis. $\mathcal{L}$ intersects $\Pi_0$ at $\varphi' = \varphi'_c$, therefore we also find

that

$$x_c = q\varphi'_c + x_0, \qquad y_c = \varpi_0 \cos\varphi'_c, \qquad z_c = \varpi_0 \sin\varphi'_c. \tag{4.8}$$

Equating the two versions of $(x_c, y_c, z_c)$ given in equations (4.6) and (4.8) allows us to obtain the following expressions

$$x_0 = \frac{Rr\cos\theta}{\sqrt{R^2+q^2}} - q\varphi'_c, \tag{4.9}$$

$$\cos\varphi'_c = \frac{R + r\sin\theta}{\varpi_0}, \qquad \sin\varphi'_c = -\frac{qr\cos\theta}{\varpi_0\sqrt{R^2+q^2}}. \tag{4.10}$$

Combining the expressions for $y_c$ and $z_c$, we also obtain that

$$\begin{aligned} y_c^2 + z_c^2 = \varpi_0^2 &= (R + r\sin\theta)^2 + \frac{q^2 r^2 \cos^2\theta}{R^2+q^2} \\ &= R^2 + 2Rr\sin\theta + r^2\frac{q^2 + R^2\sin^2\theta}{R^2+q^2}. \end{aligned} \tag{4.11}$$

As mentioned above, the arbitrary point $(\bar{x}, \bar{y}, \bar{z})$ lies in a plane $\Pi$ which is orthogonal to the loop axis. This plane crosses the loop axis at $\varphi = \bar{\varphi}$, which has coordinates $(\bar{x}_a, \bar{y}_a, \bar{z}_a)$ given by

$$\bar{x}_a = q\bar{\varphi}, \qquad \bar{y}_a = R\cos\bar{\varphi}, \qquad \bar{z}_a = R\sin\bar{\varphi}. \tag{4.12}$$

Here the tangent to the loop axis is $\bar{\boldsymbol{l}} = (q, -R\sin\bar{\varphi}, R\cos\bar{\varphi})$. Therefore the plane orthogonal to the loop axis at this point is given by

$$q(x - \bar{x}_a) - R\sin\bar{\varphi}(y - \bar{y}_a) + R\cos\bar{\varphi}(z - \bar{z}_a) = 0, \tag{4.13}$$

which reduces to

$$qx = q^2\bar{\varphi} + R(y\sin\bar{\varphi} - z\cos\bar{\varphi}) \tag{4.14}$$

on substitution of equation (4.12). The point $(\bar{x}, \bar{y}, \bar{z})$ corresponds to $\varphi' = \bar{\varphi}'$, therefore it follows from equations (4.7) and (4.9) that

$$\bar{x} = q(\bar{\varphi}' - \varphi'_c) + \frac{Rr\cos\theta}{\sqrt{R^2+q^2}}, \qquad \bar{y} = \varpi_0\cos\bar{\varphi}', \qquad \bar{z} = \varpi_0\sin\bar{\varphi}'. \tag{4.15}$$

Substituting this into the equation of the plane $\Pi$, as given in equation (4.14),

allows us to obtain an equation determining $\bar{\varphi}'$

$$q^2(\bar{\varphi}' - \bar{\varphi} - \varphi_c') + \varpi_0 R\sin(\bar{\varphi}' - \bar{\varphi}) = -\frac{qrR\cos\theta}{\sqrt{R^2+q^2}}. \tag{4.16}$$

This equation cannot be solved analytically. We do not attempt to find a solution here because it is not needed in what follows. As we have already mentioned, we only need to use the curvilinear coordinates in the vicinity of the loop, at distances not exceeding a few $a$. Hence, it suffices to obtain approximate expressions for the Cartesian coordinates in terms of $r$, $\theta$ and $\varphi$ that are linear with respect to $r$. However, we first note that when $r = 0$, it follows from equations (4.10) and (4.11) that $\varpi_0 = R$ and $\varphi_c' = 0$. Therefore the solution to equation (4.16) is $\bar{\varphi}' = \bar{\varphi}$. This is as expected because when $r = 0$, $\mathcal{L}$ coincides with the loop axis and $(\bar{x}, \bar{y}, \bar{z}) = (\bar{x}_a, \bar{y}_a, \bar{z}_a)$. We then continue on to linearize the expressions for the Cartesian coordinates given in equation (4.15), such that they are linear with respect to $r$. To do this, first we must linearize equations (4.10) and (4.11) which gives

$$\varpi_0 \approx R + r\sin\theta, \qquad \varphi_c' \approx -\frac{qr\cos\theta}{R\sqrt{R^2+q^2}}. \tag{4.17}$$

Next, we look for an approximate linear solution to equation (4.16) in the form $\bar{\varphi}' = \bar{\varphi} + cr$, where $c$ is a constant to be determined. Substituting this expression in equation (4.16) along with equation (4.17) gives

$$q^2\left(cr + \frac{qr\cos\theta}{R\sqrt{R^2+q^2}}\right) + (R + r\sin\theta)R\sin(cr) \approx -\frac{qrR\cos\theta}{\sqrt{R^2+q^2}}. \tag{4.18}$$

The $\sin(cr)$ term can be linearized by using the approximation $\sin(cr) \approx cr$ to give

$$q^2\left(cr + \frac{qr\cos\theta}{R\sqrt{R^2+q^2}}\right) + crR(R + r\sin\theta) \approx -\frac{qrR\cos\theta}{\sqrt{R^2+q^2}}. \tag{4.19}$$

This introduces another non-linear term which we drop, leaving us with

$$q^2\left(cr+\frac{qr\cos\theta}{R\sqrt{R^2+q^2}}\right)+crR^2\approx-\frac{qrR\cos\theta}{\sqrt{R^2+q^2}}. \tag{4.20}$$

Then, rearranging to find $c$, we find that

$$c\approx-\frac{q\cos\theta}{R\sqrt{R^2+q^2}}, \tag{4.21}$$

and therefore

$$\bar{\varphi}'\approx\bar{\varphi}-\frac{qr\cos\theta}{R\sqrt{R^2+q^2}}. \tag{4.22}$$

Substituting equations (4.17) and (4.22) in equation (4.15) and dropping the bar, as shown in appendix A.1, we finally arrive at

$$x=q\varphi+\frac{Rr\cos\theta}{\sqrt{R^2+q^2}}+\mathcal{O}(\varepsilon^2), \tag{4.23}$$

$$y=R\cos\varphi+r\sin\theta\cos\varphi+\frac{qr\cos\theta\sin\varphi}{\sqrt{R^2+q^2}}+\mathcal{O}(\varepsilon^2), \tag{4.24}$$

$$z=R\sin\varphi+r\sin\theta\sin\varphi-\frac{qr\cos\theta\cos\varphi}{\sqrt{R^2+q^2}}+\mathcal{O}(\varepsilon^2), \tag{4.25}$$

where $\varepsilon=a/R$ and $\mathcal{O}(\varepsilon^2)$ indicates higher terms with respect to $r$ starting from quadratic.

## 4.2 MHD in Curvilinear Coordinates

To investigate the oscillations of our loop we use the ideal linear MHD equations in the form introduced in equations (2.31) and (2.32)

$$\rho\frac{\partial^2\boldsymbol{\xi}}{\partial t^2}=\frac{1}{\mu_0}\left((\nabla\times\boldsymbol{B})\times\boldsymbol{b}+(\nabla\times\boldsymbol{b})\times\boldsymbol{B}\right), \tag{4.26}$$

$$\boldsymbol{b}=\nabla\times(\boldsymbol{\xi}\times\boldsymbol{B}), \tag{4.27}$$

where $\boldsymbol{\xi}$ is the plasma displacement, $\boldsymbol{B}$ is the equilibrium magnetic field, $\boldsymbol{b}=(b_r,b_\theta,b_\varphi)$ is the perturbed magnetic field and $\rho=\rho(\varphi)$ is the density. Using

equation (3.3), with $\varpi = \varpi_0$, and also equation (4.17) we can write

$$\nabla \times \boldsymbol{B} = \frac{2q\boldsymbol{B}}{q^2 + \varpi_0^2} \approx \frac{2q\boldsymbol{B}}{q^2 + (R + r\sin\theta)^2} \approx \frac{2q\boldsymbol{B}}{q^2 + R^2}, \tag{4.28}$$

where we have also assumed that $r\sin\theta \ll R$. Hence, equation (4.26) can be written as

$$\rho\frac{\partial^2\boldsymbol{\xi}}{\partial t^2} = \frac{1}{\mu_0}\left(\frac{2q}{q^2 + R^2}\boldsymbol{B} \times \boldsymbol{b} + (\nabla \times \boldsymbol{b}) \times \boldsymbol{B}\right). \tag{4.29}$$

Before we can use these equations to derive the governing equation for our model, we must write them in terms of our curvilinear coordinates. The main task involved in this is to find the curl of a vector in our coordinate system. We start this derivation by introducing the stretching variable $\sigma = \varepsilon^{-1}r/R$. It is convenient to introduce this variable because, in what follows, we consider only the vicinity of the magnetic tube where $r/R = \mathcal{O}(\varepsilon)$. Hence, from now on, the curvilinear coordinates are $\sigma$, $\theta$, $\varphi$, such that

$$x = q\varphi + \frac{\varepsilon\sigma R^2\cos\theta}{\sqrt{R^2 + q^2}} + \mathcal{O}(\varepsilon^2), \tag{4.30}$$

$$y = R\cos\varphi + \varepsilon\sigma R\sin\theta\cos\varphi + \frac{\varepsilon\sigma qR\cos\theta\sin\varphi}{\sqrt{R^2 + q^2}} + \mathcal{O}(\varepsilon^2), \tag{4.31}$$

$$z = R\sin\varphi + \varepsilon\sigma R\sin\theta\sin\varphi - \frac{\varepsilon\sigma qR\cos\theta\cos\varphi}{\sqrt{R^2 + q^2}} + \mathcal{O}(\varepsilon^2). \tag{4.32}$$

The general expression for the curl of a vector in an arbitrary coordinate system can be found in many textbooks, such as Goedbloed and Poedts (2004), and is written below for our coordinate system

$$\begin{aligned}\nabla \times \boldsymbol{B} &= \frac{1}{h_\theta h_\varphi}\left(\frac{\partial}{\partial\theta}(h_\varphi B_\varphi) - \frac{\partial}{\partial\varphi}(h_\theta B_\theta)\right)\hat{\boldsymbol{\sigma}} \\ &+ \frac{1}{h_\sigma h_\varphi}\left(\frac{\partial}{\partial\varphi}(h_\sigma B_\sigma) - \frac{\partial}{\partial\sigma}(h_\varphi B_\varphi)\right)\hat{\boldsymbol{\theta}} \\ &+ \frac{1}{h_\sigma h_\theta}\left(\frac{\partial}{\partial\sigma}(h_\theta B_\theta) - \frac{\partial}{\partial\theta}(h_\sigma B_\sigma)\right)\hat{\boldsymbol{\varphi}},\end{aligned} \tag{4.33}$$

where

$$h_\sigma = \left|\frac{\partial\boldsymbol{X}}{\partial\sigma}\right|, \qquad h_\theta = \left|\frac{\partial\boldsymbol{X}}{\partial\theta}\right|, \qquad h_\varphi = \left|\frac{\partial\boldsymbol{X}}{\partial\varphi}\right|, \tag{4.34}$$

are scale factors, $\boldsymbol{X} = (x, y, z)$ and $|\boldsymbol{A}|$ represents the magnitude of a vector, $\boldsymbol{A}$. Hence, we need to find the derivatives of $\boldsymbol{X}$ with respect to each coordinate. Using equations (4.30) to (4.32) we obtain

$$\begin{aligned}\frac{\partial \boldsymbol{X}}{\partial \sigma} &= \varepsilon R \left( \frac{R\cos\theta}{\sqrt{R^2+q^2}}, \sin\theta\cos\varphi + \frac{q\cos\theta\sin\varphi}{\sqrt{R^2+q^2}}, \right. \\ &\qquad \left. \sin\theta\sin\varphi - \frac{q\cos\theta\cos\varphi}{\sqrt{R^2+q^2}} \right) + \mathcal{O}(\varepsilon^2), \end{aligned} \tag{4.35}$$

$$\begin{aligned}\frac{\partial \boldsymbol{X}}{\partial \theta} &= \varepsilon\sigma R \left( -\frac{R\sin\theta}{\sqrt{R^2+q^2}}, \cos\theta\cos\varphi - \frac{q\sin\theta\sin\varphi}{\sqrt{R^2+q^2}}, \right. \\ &\qquad \left. \cos\theta\sin\varphi + \frac{q\sin\theta\cos\varphi}{\sqrt{R^2+q^2}} \right) + \mathcal{O}(\varepsilon^2), \end{aligned} \tag{4.36}$$

$$\begin{aligned}\frac{\partial \boldsymbol{X}}{\partial \varphi} &= \left( q, -R\sin\varphi - \varepsilon\sigma R\sin\theta\sin\varphi + \frac{\varepsilon\sigma q R\cos\theta\cos\varphi}{\sqrt{R^2+q^2}}, \right. \\ &\qquad \left. R\cos\varphi + \varepsilon\sigma R\sin\theta\cos\varphi + \frac{\varepsilon\sigma q R\cos\theta\sin\varphi}{\sqrt{R^2+q^2}} \right) + \mathcal{O}(\varepsilon^2). \end{aligned} \tag{4.37}$$

Then, using equations (4.35) to (4.37) to evaluate equation (4.34) as shown in appendix A.2, we obtain the following expressions for the scale factors

$$h_\sigma = \varepsilon R + \mathcal{O}(\varepsilon^2), \qquad h_\theta = \varepsilon\sigma R + \mathcal{O}(\varepsilon^2), \qquad h_\varphi = \sqrt{R^2+q^2} + \mathcal{O}(\varepsilon). \tag{4.38}$$

Therefore, to the leading order approximation with respect to $\varepsilon$, we find that

$$\begin{aligned}\nabla\times\boldsymbol{B} &= \left( \frac{1}{\varepsilon\sigma R}\frac{\partial B_\varphi}{\partial\theta} - \frac{1}{\sqrt{R^2+q^2}}\frac{\partial B_\theta}{\partial\varphi} \right)\hat{\boldsymbol{\sigma}} \\ &+ \left( \frac{1}{\sqrt{R^2+q^2}}\frac{\partial B_\sigma}{\partial\varphi} - \frac{1}{\varepsilon R}\frac{\partial B_\varphi}{\partial\sigma} \right)\hat{\boldsymbol{\theta}} \\ &+ \frac{1}{\varepsilon\sigma R}\left( \frac{\partial(\sigma B_\theta)}{\partial\sigma} - \frac{\partial B_\sigma}{\partial\theta} \right)\hat{\boldsymbol{\varphi}}. \end{aligned} \tag{4.39}$$

Using equation (4.39) we can now write the MHD equations in terms of our curvilinear coordinates. The components of the momentum equation (4.29) are

$$\frac{\partial^2 \xi_\sigma}{\partial t^2} = \frac{B}{\mu_0 \rho}\left(\frac{1}{\sqrt{R^2+q^2}}\frac{\partial b_\sigma}{\partial \varphi} - \frac{1}{\varepsilon R}\frac{\partial b_\varphi}{\partial \sigma} - \frac{2q b_\theta}{R^2+q^2}\right), \tag{4.40}$$

$$\frac{\partial^2 \xi_\theta}{\partial t^2} = \frac{B}{\mu_0 \rho}\left(\frac{1}{\sqrt{R^2+q^2}}\frac{\partial b_\theta}{\partial \varphi} - \frac{1}{\varepsilon \sigma R}\frac{\partial b_\varphi}{\partial \theta} + \frac{2q b_\sigma}{R^2+q^2}\right), \tag{4.41}$$

$$\frac{\partial^2 \xi_\varphi}{\partial t^2} = 0. \tag{4.42}$$

Note that equation (4.42) is similar to the equivalent equation for the straight loop case, shown in equation (2.36), where we find that $\xi_z = 0$. The components of the induction equation (4.27) are

$$b_\sigma = \frac{B}{\sqrt{R^2+q^2}}\frac{\partial \xi_\sigma}{\partial \varphi}, \tag{4.43}$$

$$b_\theta = \frac{B}{\sqrt{R^2+q^2}}\frac{\partial \xi_\theta}{\partial \varphi}, \tag{4.44}$$

$$b_\varphi = -\frac{B}{\varepsilon \sigma R}\left(\frac{\partial(\sigma \xi_\sigma)}{\partial \sigma} + \frac{\partial \xi_\theta}{\partial \theta}\right). \tag{4.45}$$

## 4.3 Derivation of the Governing Equation

Now that we have found the MHD equations in terms of our curvilinear coordinates, we can proceed to derive the governing equation for kink oscillations of our loop model. We start by combining the components of the momentum and induction equations, and introducing the magnetic pressure perturbation, $P = B b_\varphi / \mu_0$, to find

$$\frac{\partial^2 \xi_\sigma}{\partial t^2} = v_A^2\left(\frac{1}{R^2+q^2}\frac{\partial^2 \xi_\sigma}{\partial \varphi^2} - \frac{\mu_0}{\varepsilon R B_0^2}\frac{\partial P}{\partial \sigma} - \frac{2q}{(R^2+q^2)^{3/2}}\frac{\partial \xi_\theta}{\partial \varphi}\right), \tag{4.46}$$

$$\frac{\partial^2 \xi_\theta}{\partial t^2} = v_A^2\left(\frac{1}{R^2+q^2}\frac{\partial^2 \xi_\theta}{\partial \varphi^2} - \frac{\mu_0}{\varepsilon \sigma R B_0^2}\frac{\partial P}{\partial \theta} + \frac{2q}{(R^2+q^2)^{3/2}}\frac{\partial \xi_\sigma}{\partial \varphi}\right), \tag{4.47}$$

$$P = -\frac{B^2}{\varepsilon\sigma\mu_0 R}\left(\frac{\partial(\sigma\xi_\sigma)}{\partial\sigma} + \frac{\partial\xi_\theta}{\partial\theta}\right), \tag{4.48}$$

where $v_A(\varphi) = B(\mu_0\rho)^{-1/2}$ is the Alfvén speed and $B$ is evaluated at the loop axis. At this point we choose to introduce the distance along the loop axis, $s$. This distance can be obtained from the parametric equation of the loop axis (equation (3.11)) by evaluating the following integral:

$$s = \int_{\varphi_0}^{\varphi} \sqrt{x'(\varphi)^2 + y'(\varphi)^2 + z'(\varphi)^2}\, d\varphi, \tag{4.49}$$

where a dash denotes a derivative with respect to $\varphi$. After substituting the components from equation (3.11), we find that

$$\begin{aligned} s &= \int_{\varphi_0}^{\varphi} \sqrt{q^2 + R^2\sin^2\varphi + R^2\cos^2\varphi}\, d\varphi \\ &= \int_{\varphi_0}^{\varphi} \sqrt{R^2 + q^2}\, d\varphi \\ &= \sqrt{R^2 + q^2}(\varphi - \varphi_0). \end{aligned} \tag{4.50}$$

Hence, $s = 0$ at one footpoint and

$$s = L = \sqrt{R^2 + q^2}(\pi - 2\varphi_0) \tag{4.51}$$

at the other. Equation (4.50) shows that the distance along the loop axis is related to $\varphi$. This implies that the density, $\rho(\varphi)$, and Alfvén speed, $v_A(\varphi)$, can also be thought of as being dependent on the distance along the loop, such that $\rho = \rho(s)$ and $v_A = v_A(s)$.

We now use equation (4.50) to write equations (4.46) to (4.48) in terms of $s$ and, at the same time, we also return to the original variable $r$, using the relation $r = \epsilon\sigma R$. To convert the derivatives into these variables, we use relations of the following form:

$$\frac{\partial f}{\partial A} = \frac{dB}{dA}\frac{\partial f}{\partial B}, \qquad \frac{\partial^2 f}{\partial A^2} = \left(\frac{dB}{dA}\right)^2 \frac{\partial^2 f}{\partial B^2}, \tag{4.52}$$

where $f(A, B)$ is an arbitrary function. For the specific cases needed here,

equation (4.52) leads to

$$\frac{\partial f}{\partial \sigma} = \epsilon R \frac{\partial f}{\partial r}, \tag{4.53}$$

$$\frac{\partial f}{\partial \varphi} = \sqrt{R^2+q^2}\frac{\partial f}{\partial s}, \qquad \frac{\partial^2 f}{\partial \varphi^2} = (R^2+q^2)\frac{\partial^2 f}{\partial s^2}. \tag{4.54}$$

Applying these relations to equations (4.46) to (4.48) leads us to obtain the following system of equations:

$$\frac{\partial^2 \xi_r}{\partial t^2} = v_A^2 \left( \frac{\partial^2 \xi_r}{\partial s^2} - \frac{\mu_0}{B^2}\frac{\partial P}{\partial r} - \frac{2q}{R^2+q^2}\frac{\partial \xi_\theta}{\partial s} \right), \tag{4.55}$$

$$\frac{\partial^2 \xi_\theta}{\partial t^2} = v_A^2 \left( \frac{\partial^2 \xi_\theta}{\partial s^2} - \frac{\mu_0}{rB^2}\frac{\partial P}{\partial \theta} + \frac{2q}{R^2+q^2}\frac{\partial \xi_r}{\partial s} \right), \tag{4.56}$$

$$P = -\frac{B^2}{r\mu_0}\left( \frac{\partial (r\xi_r)}{\partial r} + \frac{\partial \xi_\theta}{\partial \theta} \right). \tag{4.57}$$

This system of equations has to be supplemented by several boundary conditions. First, consider the ends of the loop. Here the magnetic field lines are frozen in the dense photospheric plasma and we have

$$\xi_r = \xi_\theta = 0 \quad \text{at} \quad s = 0, L, \tag{4.58}$$

where $L$ is the length of the loop, as defined in equation (4.51). Next we must consider the jump at the tube boundary, located at $r = a$. Here the normal component of the displacement and the perturbation of the total pressure need to be continuous. It can be shown that the normal vector to the tube boundary is given by $\boldsymbol{n} = \boldsymbol{e}_r + \mathcal{O}(\varepsilon)$. Hence, in the leading order approximation with respect to $\varepsilon$, we can take $\boldsymbol{n} = \boldsymbol{e}_r$. The normal component of the displacement is approximately equal to $\xi_r$. If we introduce the jump of a function $f$ across the boundary, such that

$$[\![ f ]\!] = \lim_{\delta \to +0} \{ f(a+\delta) - f(a-\delta) \}, \tag{4.59}$$

then the boundary condition for $\xi_r$ can be written as

$$[\![ \xi_r ]\!] = 0 \quad \text{at} \quad r = a. \tag{4.60}$$

Since the equilibrium magnetic field is inhomogeneous, we have to impose the condition that the Lagrangian perturbation of the total pressure is continuous at the boundary. This implies that the following expression must be true:

$$\left[\left[p_0 + P + \xi_r \frac{\partial p_0}{\partial r}\right]\right] = 0, \quad \text{at} \quad r = a, \tag{4.61}$$

where $p_0 = B^2(2\mu_0)^{-1}$ is the equilibrium magnetic pressure and $B$ is the magnitude of the magnetic field, as given by equation (3.10). The equilibrium magnetic field and its partial derivative with respect to $r$ are continuous at the boundary. This implies that the jump in the Lagrangian perturbation of the total pressure coincides with the jump in the Eulerian perturbation of the total pressure and equation (4.61) reduces to

$$[\![P]\!] = 0, \quad \text{at} \quad r = a. \tag{4.62}$$

To make further progress in the derivation of the governing equation, we once again consider the small parameter $\varepsilon = a/R$. In the radial direction the typical length scale of the loop is $\sim a$, while along the length of the loop the scale is $\sim R$. To obtain typical length scales which are the same in both directions we introduce the scaling variable $S = \varepsilon s$ and also scale $t$ in the same way: $T = \varepsilon t$. Furthermore, we can also write $R$ and $q$ in terms of $\varepsilon$, such that $R = a\varepsilon^{-1}\tilde{R}$ and $q = a\varepsilon^{-1}\tilde{q}$, where $\tilde{q}, \tilde{R} \sim 1$. These relations can be combined to obtain $2q(R^2 + q^2)^{-1} = \varepsilon\alpha/a$, where $\alpha = 2\tilde{q}(\tilde{R}^2 + \tilde{q}^2)^{-1} \sim 1$. By using equation (4.52), we can introduce these variables into equations (4.55) to (4.57), which leads to:

$$\varepsilon^2 \frac{\partial^2 \xi_r}{\partial T^2} = v_A^2 \left(\varepsilon^2 \frac{\partial^2 \xi_r}{\partial S^2} - \frac{\mu_0}{B^2}\frac{\partial P}{\partial r} - \frac{\alpha\varepsilon^2}{a}\frac{\partial \xi_\theta}{\partial S}\right), \tag{4.63}$$

$$\varepsilon^2 \frac{\partial^2 \xi_\theta}{\partial T^2} = v_A^2 \left(\varepsilon^2 \frac{\partial^2 \xi_\theta}{\partial S^2} - \frac{\mu_0}{rB^2}\frac{\partial P}{\partial \theta} + \frac{\alpha\varepsilon^2}{a}\frac{\partial \xi_r}{\partial S}\right). \tag{4.64}$$

In both equations we see that all terms are now $\mathcal{O}(\varepsilon^2)$, except those involving the magnetic pressure perturbation $P$. Therefore we introduce another scaling variable $P = \varepsilon^2 Q$, so that all terms in the above equations are the same order of magnitude. Including this scaling variable into equations (4.57), (4.63) and

(4.64) gives:

$$\frac{\partial^2 \xi_r}{\partial T^2} = v_A^2 \left( \frac{\partial^2 \xi_r}{\partial S^2} - \frac{\mu_0}{B^2} \frac{\partial Q}{\partial r} - \frac{\alpha}{a} \frac{\partial \xi_\theta}{\partial S} \right), \tag{4.65}$$

$$\frac{\partial^2 \xi_\theta}{\partial T^2} = v_A^2 \left( \frac{\partial^2 \xi_\theta}{\partial S^2} - \frac{\mu_0}{rB^2} \frac{\partial Q}{\partial \theta} + \frac{\alpha}{a} \frac{\partial \xi_r}{\partial S} \right), \tag{4.66}$$

$$\varepsilon^2 Q = -\frac{B^2}{r\mu_0} \left( \frac{\partial (r\xi_r)}{\partial r} + \frac{\partial \xi_\theta}{\partial \theta} \right). \tag{4.67}$$

Hence we see that the only term which is affected by $\varepsilon$ is the term on the left hand side of equation (4.67). This term is now $\mathcal{O}(\varepsilon^2)$ and is therefore much smaller than other terms in the equation. Therefore, we drop this term and the system of equations becomes

$$\frac{\partial^2 \xi_r}{\partial T^2} = v_A^2 \left( \frac{\partial^2 \xi_r}{\partial S^2} - \frac{\mu_0}{B^2} \frac{\partial Q}{\partial r} - \frac{\alpha}{a} \frac{\partial \xi_\theta}{\partial S} \right), \tag{4.68}$$

$$\frac{\partial^2 \xi_\theta}{\partial T^2} = v_A^2 \left( \frac{\partial^2 \xi_\theta}{\partial S^2} - \frac{\mu_0}{rB^2} \frac{\partial Q}{\partial \theta} + \frac{\alpha}{a} \frac{\partial \xi_r}{\partial S} \right), \tag{4.69}$$

$$\frac{\partial (r\xi_r)}{\partial r} + \frac{\partial \xi_\theta}{\partial \theta} = 0. \tag{4.70}$$

It follows from equation (4.70) that

$$\frac{\partial (r\xi_r)}{\partial r} = -\frac{\partial \xi_\theta}{\partial \theta}. \tag{4.71}$$

To ensure that this equation is satisfied, we introduce a function $\psi$ such that

$$\xi_r = \frac{1}{r} \frac{\partial \psi}{\partial \theta}, \qquad \xi_\theta = -\frac{\partial \psi}{\partial r}. \tag{4.72}$$

Substituting these expressions into equations (4.68) and (4.69) gives the following two equations

$$\frac{1}{r} \frac{\partial^2}{\partial T^2} \frac{\partial \psi}{\partial \theta} = v_A^2 \left( \frac{1}{r} \frac{\partial^2}{\partial S^2} \frac{\partial \psi}{\partial \theta} - \frac{\mu_0}{B^2} \frac{\partial Q}{\partial r} + \frac{\alpha}{a} \frac{\partial}{\partial S} \frac{\partial \psi}{\partial r} \right), \tag{4.73}$$

$$-r \frac{\partial^2}{\partial T^2} \frac{\partial \psi}{\partial r} = v_A^2 \left( -r \frac{\partial^2}{\partial S^2} \frac{\partial \psi}{\partial r} - \frac{\mu_0}{B^2} \frac{\partial Q}{\partial \theta} + \frac{\alpha}{a} \frac{\partial}{\partial S} \frac{\partial \psi}{\partial \theta} \right). \tag{4.74}$$

Here we can use cross differentiation to eliminate $Q$ from these equations and,

returning to the unscaled variables, we obtain the following equation for $\psi$,

$$\frac{\partial^2 F}{\partial t^2} - v_A^2 \frac{\partial^2 F}{\partial s^2} = 0, \qquad F = r\frac{\partial}{\partial r} r \frac{\partial \psi}{\partial r} + \frac{\partial^2 \psi}{\partial \theta^2}. \tag{4.75}$$

It follows from equations (4.58) and (4.72) that

$$\psi = 0 \quad \text{at} \quad s = 0, L. \tag{4.76}$$

In what follows we only consider eigenmodes of kink oscillations and take the displacement proportional to $\exp(-i\omega t)$. Then the first equation in equation (4.75) reduces to

$$\frac{\partial^2 F}{\partial s^2} + \frac{\omega^2}{v_A^2} F = 0. \tag{4.77}$$

This equation describes Alfvén oscillations of individual magnetic field lines. We assume that the eigenfrequencies of kink oscillations do not coincide with any local Alfvén frequencies. Then equation (4.77) only has a trivial solution, $F = 0$, and $\psi$ satisfies the equation

$$r\frac{\partial}{\partial r} r \frac{\partial \psi}{\partial r} + \frac{\partial^2 \psi}{\partial \theta^2} = 0. \tag{4.78}$$

Since we are restricting our analysis to kink oscillations, we take $\psi$ proportional to $\exp(i\theta)$, under the assumption that this azimuthal dependence is still valid in the present geometry. Therefore this equation reduces to

$$r\frac{\partial}{\partial r} r \frac{\partial \psi}{\partial r} - \psi = 0. \tag{4.79}$$

This equation has the solution $\psi = \psi_1 r + \psi_2 r^{-1}$, where, at present, $\psi_1 = \psi_1(s)$ and $\psi_2 = \psi_2(s)$ are arbitrary functions of $s$. To avoid $\psi$ becoming infinite as $r \to 0$, we set $\psi_2 = 0$ for $r < a$, and as $r \to \infty$ we require the perturbation to decay, hence we set $\psi_1 = 0$ for $r > a$. Combining these conditions results in the following expression for $\psi$:

$$\psi = \begin{cases} \psi_1(s) r & r < a \\ \psi_2(s) r^{-1} & r > a. \end{cases} \tag{4.80}$$

If we now consider the unscaled version of equation (4.74), and use equation

(4.80) as shown in appendix A.3, we obtain two equations, one for the region inside the loop

$$P_i = \rho_i \left( irv_{Ai}^2 \frac{d^2\psi_1}{ds^2} + \frac{2qrv_{Ai}^2}{R^2+q^2}\frac{d\psi_1}{ds} + ir\omega^2\psi_1 \right), \tag{4.81}$$

and another which applies outside the loop

$$P_e = \rho_e \left( -\frac{iv_{Ae}^2}{r}\frac{d^2\psi_2}{ds^2} + \frac{2qv_{Ae}^2}{r(R^2+q^2)}\frac{d\psi_2}{\partial s} - \frac{i\omega^2}{r}\psi_2 \right). \tag{4.82}$$

Here a subscript $i$ or $e$ refers to quantities inside or outside of the loop, respectively. We choose to use equation (4.74) rather than equation (4.73), because we take $P$ to be proportional to $\exp(i\theta)$ and hence the derivative of $P$ with respect to $\theta$ simplifies to $iP$. Using equation (4.72) we can rewrite the boundary condition given in equation (4.60) in terms of $\psi$,

$$[\![\psi]\!] = 0 \quad \text{at} \quad r = a. \tag{4.83}$$

This implies that at the loop boundary, $\psi_2 = a^2\psi_1$. Equation (4.62) also tells us that $P_i = P_e$ at the boundary. Using these in equation (4.82) gives

$$P_i = \rho_e \left( -iav_{Ae}^2 \frac{d^2\psi_1}{ds^2} + \frac{2aqv_{Ae}^2}{R^2+q^2}\frac{d\psi_1}{ds} - ia\omega^2\psi_1 \right). \tag{4.84}$$

$P_i$ can be eliminated between this equation, and equation (4.81) evaluated at $r = a$, to give the governing equation for the system,

$$\frac{d^2\psi_1}{ds^2} + \frac{\omega^2}{c_k^2}\psi_1 = 0, \tag{4.85}$$

where

$$c_k^2 = \frac{2B^2}{\mu_0(\rho_i + \rho_e)}, \tag{4.86}$$

is the squared kink speed of the tube and $B$ is evaluated at the loop axis. Since the plasma density varies along the loop, $c_k$ is a function of $s$. The function $\psi_1$ satisfies the boundary conditions

$$\psi_1 = 0 \quad \text{at} \quad s = 0, L. \tag{4.87}$$

Equations (4.85) and (4.87) form the boundary value problem that determines the frequencies of the fundamental mode and overtones of kink oscillations of a curved non-planar loop. This boundary value problem is the same as the boundary value problem determining the frequencies of kink oscillations of a straight magnetic loop with density varying along the loop, as found by Dymova and Ruderman (2005). Hence, we find that the loop curvature and torsion do not directly affect the frequencies of kink oscillations. This result can be expected on physical grounds because, in the leading order approximation with respect to $\varepsilon$, we neglect both the curvature and torsion of the tube. This effectively reduces the problem to studying kink oscillations of a straight tube. However, the loop curvature and torsion can affect these frequencies indirectly because they determine the dependence of $\rho_e$ and $\rho_i$ on $s$.

It follows from equations (4.72) and (4.80) that $\xi_r = i\psi_1$ and $\xi_\theta = -\psi_1$ inside the tube. These relations imply that both $\xi_r$ and $\xi_\theta$ are independent of $r$ inside the tube. Therefore we can say that $\boldsymbol{\xi}$ is also independent of $r$ inside the tube, so that, in the leading order approximation with respect to $\varepsilon$, the tube oscillates as a solid.

Equation (4.85) describes only the eigenmode dependence on $s$. We managed to factor out the radial dependence because $\rho_i$ and $\rho_e$ are independent of $r$. As a result, in the leading order approximation with respect to $\varepsilon$, the Alfvén speeds inside the loop and in the loop vicinity are independent of $r$. However the magnitude of the magnetic field is not constant. We can see from equation (3.10) that it varies from $B_0$ at $\varpi = 0$ to 0 as $\varpi \to \infty$. This implies that, in our model, there is a fundamental Alfvén continuum, $0 \leq \omega_A \leq \omega_{Af}$, and an Alfvén continuum for every overtone, $0 \leq \omega_A \leq \omega_{An}$, where $n = 1, 2, ....$ We do not give the expressions for $\omega_{Af}$ and $\omega_{An}$ because they are not used in what follows. It can be shown that the frequency of the fundamental kink mode is less than $\omega_{Af}$, and the frequency of the $n$th overtone is less than $\omega_{An}$, which implies that there is an Alfvén resonance. This should cause resonant damping of the loop kink oscillations. However the resonant surface is at a distance of the order of $R \gg a$ from the loop, where the oscillation amplitude is extremely small. As a result the resonant damping is very weak and can be neglected.

Since the Alfvén frequency is tending to zero as $\varpi \to \infty$, at some distance from the loop the eigenmode is leaky, which should also cause the oscillation to

damp. However, once again, the wave leakage occurs at distances of the order of $R \gg a$ from the loop, where the oscillation amplitude is extremely small. As a result the damping due to leakage is also very weak and can be neglected.

## 4.4 Polarization of Kink Oscillations

As we have already mentioned, the non-planarity does not directly affect the frequencies of kink oscillations. The main effect of non-planarity resides in changing the polarization of kink oscillations. Therefore we will now discuss how kink oscillations of non-planar loops are polarized.

It is impossible to obtain any information about the polarization of kink eigenmodes directly from equation (4.85) because, when we derived this equation, we cancelled out the dependence on $t$ and $\theta$ by taking all variables proportional to $\exp(-i\omega t + i\theta)$. Hence we will first need to restore this dependence. To do this we write $\psi = r\Psi(s)\exp(-i\omega t + i\theta)$ inside the loop, where we have renamed $\psi_1$ as $\Psi$ because the subscript is no longer necessary. We obtain the same equation (4.85) if we take $\psi = r\Psi(s)\exp(\pm i\omega t \pm i\theta)$ with any combinations of signs. Hence, the general solution is the linear combination of four different exponents. However the coefficients of these exponents are not arbitrary: they have to satisfy the condition that $\psi$ is a real function. Under this restriction, the most general form of $\psi$ is

$$\psi = r\Psi(s)\Re\{\exp(i\theta)[A_1\exp(-i\omega t) + A_2\exp(i\omega t)]\}, \tag{4.88}$$

where $\Re$ indicates the real part of a quantity, and $A_1$ and $A_2$ are arbitrary complex constants. Since it follows from equations (4.85) and (4.87) that the ratio of the imaginary and real part of $\Psi$ is constant, we can take $\Psi(s)$ to be real without loss of generality. Substituting equation (4.88) in equation (4.72) we can find that

$$\begin{aligned} \xi_r &= \Psi(s)(A_-\cos(\omega t - \theta + \alpha_-) + A_+\cos(\omega t + \theta + \alpha_+)), \\ \xi_\theta &= \Psi(s)(A_-\sin(\omega t - \theta + \alpha_-) - A_+\sin(\omega t + \theta + \alpha_+)), \end{aligned} \tag{4.89}$$

where $A_\pm$ and $\alpha_\pm$ are arbitrary real constants.

Let us now calculate the components of $\boldsymbol{\xi}$ inside the tube in Cartesian coor-

dinates. Using equations (4.35) and (4.36) we obtain that, in the leading order approximation with respect to $\varepsilon$, the Cartesian components of the unit vectors in the $r$- and $\theta$-direction are given by

$$\begin{aligned} \boldsymbol{e}_r = \frac{\partial \boldsymbol{X}}{\partial \sigma}\left|\frac{\partial \boldsymbol{X}}{\partial \sigma}\right|^{-1} &= \left(\frac{R\cos\theta}{\sqrt{R^2+q^2}}, \sin\theta\cos\varphi + \frac{q\cos\theta\sin\varphi}{\sqrt{R^2+q^2}},\right. \\ &\left. \sin\theta\sin\varphi - \frac{q\cos\theta\cos\varphi}{\sqrt{R^2+q^2}}\right), \end{aligned} \tag{4.90}$$

$$\begin{aligned} \boldsymbol{e}_\theta = \frac{\partial \boldsymbol{X}}{\partial \theta}\left|\frac{\partial \boldsymbol{X}}{\partial \theta}\right|^{-1} &= \left(-\frac{R\sin\theta}{\sqrt{R^2+q^2}}, \cos\theta\cos\varphi - \frac{q\sin\theta\sin\varphi}{\sqrt{R^2+q^2}},\right. \\ &\left. \cos\theta\sin\varphi + \frac{q\sin\theta\cos\varphi}{\sqrt{R^2+q^2}}\right). \end{aligned} \tag{4.91}$$

Now, using the relation $\boldsymbol{\xi} = (\xi_x, \xi_y, \xi_z) = \xi_r \boldsymbol{e}_r + \xi_\theta \boldsymbol{e}_\theta$ and equations (4.50) and (4.89) to (4.91), we obtain

$$\xi_x = \Psi(s)\frac{RA_c\cos(\omega t + \alpha_c)}{\sqrt{R^2+q^2}}, \tag{4.92}$$

$$\begin{aligned} \xi_y &= \Psi(s)\left(A_s\sin(\omega t+\alpha_s)\cos\left(\varphi_0 + \frac{s}{\sqrt{R^2+q^2}}\right)\right. \\ &\left. + \frac{qA_c\cos(\omega t+\alpha_c)}{\sqrt{R^2+q^2}}\sin\left(\varphi_0 + \frac{s}{\sqrt{R^2+q^2}}\right)\right), \end{aligned} \tag{4.93}$$

$$\begin{aligned} \xi_z &= \Psi(s)\left(A_s\sin(\omega t+\alpha_s)\sin\left(\varphi_0 + \frac{s}{\sqrt{R^2+q^2}}\right)\right. \\ &\left. - \frac{qA_c\cos(\omega t+\alpha_c)}{\sqrt{R^2+q^2}}\cos\left(\varphi_0 + \frac{s}{\sqrt{R^2+q^2}}\right)\right), \end{aligned} \tag{4.94}$$

where $A_c$, $A_s$, $\alpha_c$ and $\alpha_s$ are expressed in terms of $A_\pm$ and $\alpha_\pm$. Since $A_\pm$ and $\alpha_\pm$ are arbitrary real constants, $A_c$, $A_s$, $\alpha_c$ and $\alpha_s$ are also arbitrary real constants.

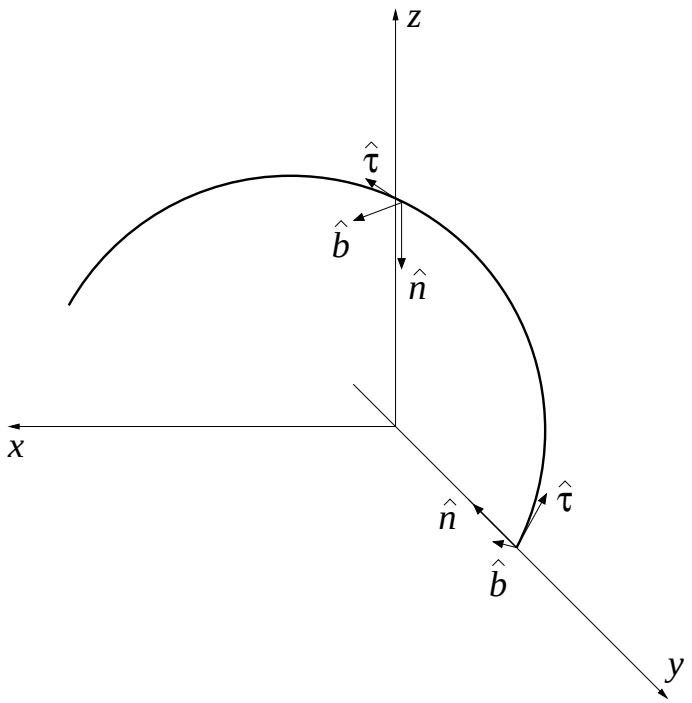


Figure 4.2: The Frenet basis for the loop axis, which is shown at two different points to illustrate the rotation of the basis along the loop.

Next we introduce the Frenet basis for the axis of the loop. It consists of the unit tangent vector $\hat{\boldsymbol{\tau}}$, the unit vector of the principal normal $\hat{\boldsymbol{n}}$, and the unit binormal vector $\hat{\boldsymbol{b}}$ (see figure 4.2). If $\boldsymbol{X} = \boldsymbol{X}_a(s)$ is the equation of the tube axis, then

$$\hat{\boldsymbol{\tau}} = \frac{d\boldsymbol{X}_a}{ds}, \quad \hat{\boldsymbol{n}} = \frac{d\hat{\boldsymbol{\tau}}}{ds}\left|\frac{d\hat{\boldsymbol{\tau}}}{ds}\right|^{-1}, \quad \hat{\boldsymbol{b}} = \hat{\boldsymbol{\tau}} \times \hat{\boldsymbol{n}}. \tag{4.95}$$

Using equations (3.11) and (4.50), as shown in appendix A.4, we obtain that the Cartesian coordinates of the Frenet basis vectors are

$$\begin{aligned} \hat{\boldsymbol{\tau}} \;=\; & \frac{1}{\sqrt{R^2+q^2}}\left(q,\, -R\sin\left(\varphi_0 + \frac{s}{\sqrt{R^2+q^2}}\right),\right. \\ & \left. R\cos\left(\varphi_0 + \frac{s}{\sqrt{R^2+q^2}}\right)\right), \end{aligned} \tag{4.96}$$

$$\hat{\boldsymbol{n}} = -\left(0,\, \cos\left(\varphi_0 + \frac{s}{\sqrt{R^2+q^2}}\right),\, \sin\left(\varphi_0 + \frac{s}{\sqrt{R^2+q^2}}\right)\right), \tag{4.97}$$

$$\begin{aligned}\hat{\boldsymbol{b}} \;=\; & \frac{1}{\sqrt{R^2+q^2}}\left(R,\, q\sin\left(\varphi_0 + \frac{s}{\sqrt{R^2+q^2}}\right),\right. \\ & \left. -q\cos\left(\varphi_0 + \frac{s}{\sqrt{R^2+q^2}}\right)\right).\end{aligned} \tag{4.98}$$

Then, using equations (4.92) to (4.94) and (4.96) to (4.98) we obtain that the projection of $\boldsymbol{\xi}$ on the Frenet basis vectors are given by

$$\begin{aligned}&\xi_\tau = \hat{\boldsymbol{\tau}}\cdot\boldsymbol{\xi} = 0, \qquad \xi_n = \hat{\boldsymbol{n}}\cdot\boldsymbol{\xi} = A_s\Psi(s)\sin(\omega t + \alpha_s),\\ &\xi_b = \hat{\boldsymbol{b}}\cdot\boldsymbol{\xi} = A_c\Psi(s)\cos(\omega t + \alpha_c).\end{aligned} \tag{4.99}$$

Eliminating $t$ from these equations we obtain

$$\frac{(\xi_n\cos\beta - \xi_b\sin\beta)^2}{(H_1\Psi(s))^2} + \frac{(\xi_n\sin\beta + \xi_b\cos\beta)^2}{(H_2\Psi(s))^2} = 1, \tag{4.100}$$

where $\beta$ is defined by

$$\tan 2\beta = \frac{2A_sA_c\sin\alpha}{A_s^2 - A_c^2}, \qquad \alpha = \alpha_c - \alpha_s, \tag{4.101}$$

and $H_1$ and $H_2$ are expressed in terms of $A_s$, $A_c$, $\alpha$ and $\beta$. We do not give these expressions because they are not used in what follows. Equation (4.100) is the equation of an ellipse in the $\xi_n\xi_b$-plane with half-axes equal to $H_1\Psi(s)$ and $H_2\Psi(s)$. The angle between one of the axes and the vector $\hat{\boldsymbol{n}}$ is $\beta$ (see figure 4.3). Note that this angle is independent of $s$. The ratio of axes is equal to $H_2/H_1$, therefore it is also independent of $s$. We see that, in general, the oscillation is elliptically polarized in the plane containing the vectors $\hat{\boldsymbol{n}}$ and $\hat{\boldsymbol{b}}$. This plane is orthogonal to the loop axis. The length of the axes of the polarization ellipse are proportional to $\Psi(s)$. As we move along the loop axis, the vectors $\hat{\boldsymbol{n}}$ and $\hat{\boldsymbol{b}}$ rotate as shown in figure 4.2. Since $\beta$ is independent of $s$, the ellipse shown in figure 4.3 will also rotate with $\hat{\boldsymbol{n}}$ and $\hat{\boldsymbol{b}}$ as we move along the loop. As it is well known from differential geometry, the angle of rotation

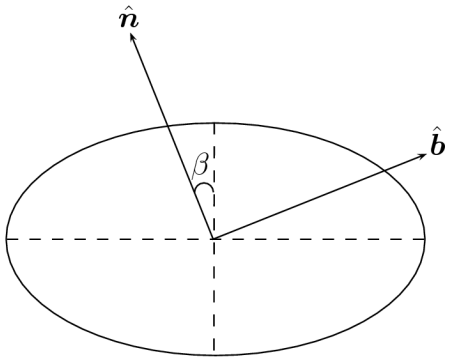


Figure 4.3: The polarization ellipse in the $\xi_n\xi_b$-plane.

per unit length is equal to the loop axis torsion, which was given previously in equation (3.15) as $q(R^2 + q^2)^{-1}$.

In an elliptically polarized eigenmode, the direction of the polarization vector rotates with constant angular speed about the tangent to the loop axis, and the end of the displacement vector moves along the polarization ellipse. If the eigenmode is linearly polarized, then the direction of the displacement vector at each point on the loop axis remains the same at any moment of time. Hence, the end of the displacement vector is moving along a straight line. For a linearly polarized eigenmode, we can arbitrarily fix the polarization direction at one point. After that, the polarization direction at all other points on the loop axis will be defined. Similarly, for an elliptically polarized mode, we can fix the direction of the semimajor axis of the polarization ellipse at one point. Then, the directions of the axes of the polarization ellipse will be defined at all other points on the loop axis. The fact that we can choose the polarization direction at one point arbitrarily implies that kink oscillations of the loop are degenerate. There are infinitely many eigenmodes with different polarizations corresponding to the same eigenfrequency. The situation is similar to that in the case of a straight tube: due to the symmetry the tube can oscillate with the same frequency in any direction. An illustration of the polarization of a fundamental kink eigenmode is shown in figure 4.4.

Van Doorsselaere et al. (2004) studied kink oscillations of a loop with a semicircular shape. They found that the account of the loop curvature removes the degeneration of kink oscillations that takes place in the case of a straight

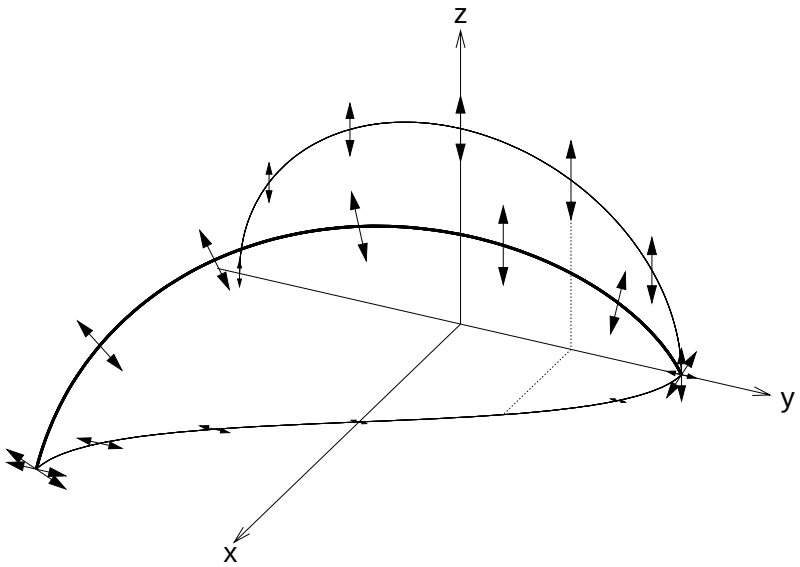


Figure 4.4: Illustration of the polarization of a fundamental kink mode. The loop axis is represented by the thick arc. The small arrows show the direction of the loop axis displacement, and their projections on the $xy$- and $yz$-planes are shown. The dotted line shows a location where the displacement is entirely in the $z$-direction, and therefore the component of the displacement on the $xy$-plane is zero. Note that we have taken $\beta = 0$ and hence the displacement is parallel to the unit normal vector $\hat{\boldsymbol{n}}$.

tube. Now there are two fundamental eigenmodes, one polarized in the vertical and one in the horizontal direction. These modes have different frequencies. The same is true for all overtones. These results were confirmed by the numerical study by Terradas et al. (2006). However, Van Doorsselaere et al. (2004) found that the difference in frequencies of the vertically and horizontally polarized eigenmodes is of the order of $\varepsilon^2$, so that it is extremely small for any realistic coronal loop. If the loop is initially displaced in a direction that is neither vertical nor horizontal, then both the vertically and horizontally polarized eigenmodes will be excited. Since they have different frequencies, a beating phenomenon will take place. However, this phenomenon will be manifested only after a time of the order of the oscillation period multiplied by $\varepsilon^{-2}$, which is much larger than the characteristic damping time of kink oscillations. This implies that the splitting of oscillation frequency caused by the curvature is unimportant from the observational point of view.

We anticipate that the situation with non-planar loops is similar to that with curved planar loops. Namely, we anticipate that, on extending our analysis to a higher order approximation with respect to $\varepsilon$, we would find that there are two fundamental modes with mutually orthogonal polarization directions and different frequencies. Furthermore, we anticipate that the same is true for all overtones. However, the frequency differences will be of the order of $\varepsilon^2$ (or, at least, of the order of $\varepsilon$), so these differences are unimportant for applications.

## 4.5 Observational Signatures of Non-Planar Loop Oscillations

Other than the distinct S-shape of a non-planar loop when viewed from above, there is another observational feature that would be characteristic of a non-planar loop, which could help when identifying oscillations of these loops.

Consider the fundamental horizontal kink oscillation of a coronal loop. In general, the fundamental horizontal mode has two nodes, one at each footpoint. In the case of a planar loop, the loop oscillates in the direction perpendicular to the line joining the footpoints. Hence, when viewed from directly above, we see the loop oscillating from one side of the line to the other. In the case of the non-planar loops discussed here, the situation is slightly different. As we found in section 4.4, the direction of polarization of the oscillation rotates with the principal normal as we move along the loop. Therefore, if there is a point where the direction of polarization is parallel to the line of sight, then we would not be able to see the oscillation. Hence, we would observe an extra node at some point along the loop. As an example, consider the loop shown in figure 4.4. If this loop was observed when the line-of-sight was parallel to the $z$-direction, then we would observe the point marked by the dotted line as being stationary, although it is in fact oscillating. Since the first overtone of a kink oscillation also has a node between the footpoints, this could lead to confusion when identifying the mode of oscillation. Here we present a method for distinguishing between observations of the fundamental harmonic of a non-planar loop kink oscillation and the first overtone of a kink oscillation. The motivation for this section was provided by an oscillation that was reported by Schrijver et al. (2002) and

interpreted by De Moortel and Brady (2007), which will be discussed further in chapter 6.

We will consider a linearly polarized kink oscillation of a non-planar loop. We choose to limit the analysis to linearly polarized oscillations rather than elliptically polarized, because, in the elliptical case, the rotation of the displacement vector causes the position of the extra node to move along the length of the loop. Since the displacement vector is fixed in the linear case, then the position of the node is also fixed, which leads to a simpler analysis.

An oscillation is linearly polarized when one of the two axes of the polarization ellipse is zero. However, since we do not give the expressions for $H_1$ and $H_2$ in equation (4.100), we will use another condition. In the general case of an elliptically polarized oscillation, the end of the displacement vector moves around the polarization ellipse and the ratio of its components $\xi_n/\xi_b$ varies with $t$. In the case of a linearly polarized oscillation, this ratio is independent of $t$ because the components of $\boldsymbol{\xi}$ are fixed. From equation (4.99), we obtain

$$\frac{\xi_n}{\xi_b} = \frac{A_s \sin(\omega t + \alpha_s)}{A_c \cos(\omega t + \alpha_c)}. \tag{4.102}$$

The above ratio is independent of $t$ when $\sin(\omega t + \alpha_s) = \cos(\omega t + \alpha_c)$. This occurs when $\alpha_c = \alpha_s + \pi/2 + n\pi$, where $n$ is any integer number. Without loss of generality we can take $\alpha_c = \alpha_s + \pi/2$. Then we obtain

$$(\xi_n, \xi_b) = A(\cos\beta, \sin\beta)\Psi(s)\sin(\omega t + \alpha_s), \tag{4.103}$$

where

$$A = \sqrt{A_s^2 + A_c^2}, \qquad \tan\beta = \frac{A_c}{A_s}. \tag{4.104}$$

We now assume that we observe an oscillation of this type and that the line-of-sight is determined by the unit vector $\boldsymbol{S}$. Let $\hat{\boldsymbol{\tau}}_0$, $\hat{\boldsymbol{n}}_0$ and $\hat{\boldsymbol{b}}_0$ be the vectors of the Frenet basis at the loop apex, i.e. at $s = L/2$. We define the vector $\boldsymbol{S}$ as (see figure 4.5)

$$\boldsymbol{S} = \hat{\boldsymbol{n}}_0 \cos\chi + \hat{\boldsymbol{b}}_0 \sin\chi \cos\varsigma + \hat{\boldsymbol{\tau}}_0 \sin\chi \sin\varsigma, \tag{4.105}$$

where $0 \leq \chi \leq \pi$ and $0 \leq \varsigma \leq 2\pi$. Since $s = L/2$, it follows from equation

(4.51) that $\varphi_0 + s(R^2+q^2)^{-1/2} = \pi/2$. Substituting this expression in equations (4.96) to (4.98) we obtain

$$\hat{\boldsymbol{\tau}}_0 = \frac{(q,-R,0)}{\sqrt{R^2+q^2}}, \quad \hat{\boldsymbol{n}}_0 = (0,0,-1), \quad \hat{\boldsymbol{b}}_0 = \frac{(R,q,0)}{\sqrt{R^2+q^2}}. \tag{4.106}$$

Then, writing equations (4.97) and (4.98) in terms of the vectors given in equation (4.106), we obtain

$$\begin{aligned} \hat{\boldsymbol{n}} &= \sin\varphi\hat{\boldsymbol{n}}_0 + \frac{\cos\varphi}{\sqrt{R^2+q^2}}\left(R\hat{\boldsymbol{\tau}}_0 - q\hat{\boldsymbol{b}}_0\right), \\ \hat{\boldsymbol{b}} &= \frac{qR(1-\sin\varphi)\hat{\boldsymbol{\tau}}_0 + (R^2+q^2\sin\varphi)\hat{\boldsymbol{b}}_0}{R^2+q^2} + \frac{q\cos\varphi}{\sqrt{R^2+q^2}}\hat{\boldsymbol{n}}_0, \end{aligned} \tag{4.107}$$

where $\varphi$ is expressed in terms of $s$ by equation (4.50). Visually we can only observe the component of the vector $\boldsymbol{\xi}$ perpendicular to $\boldsymbol{S}$, and this component is given by $\boldsymbol{\xi}_\perp = \boldsymbol{\xi} - \boldsymbol{S}(\boldsymbol{\xi}\cdot\boldsymbol{S})$. As we found previously, the direction of polarization rotates as we move along the loop. If there is a point on the loop where the direction of polarization is parallel to the line-of-sight, then $\boldsymbol{\xi}_\perp = 0$ and we will not be able to observe the oscillation. This would give the appearance of an additional node in the oscillation. We can find the location of this additional node on the loop by finding the value of $\varphi$ which corresponds to $\boldsymbol{\xi}_\perp = 0$.

The condition that $\boldsymbol{\xi}_\perp = 0$ is written as $\boldsymbol{\xi} \parallel \boldsymbol{S}$. Using equations (4.103) and (4.107), as shown in appendix A.5, we obtain from the condition $\boldsymbol{\xi} \parallel \boldsymbol{S}$ two equations,

$$\begin{aligned} \frac{(R^2+q^2\sin\varphi)\tan\beta}{R^2+q^2} \;-\; &\frac{q\cos\varphi}{\sqrt{R^2+q^2}} \\ &= \tan\chi\cos\varsigma\left(\sin\varphi + \frac{q\cos\varphi\tan\beta}{\sqrt{R^2+q^2}}\right), \end{aligned} \tag{4.108}$$

$$\begin{aligned} \frac{qR(1-\sin\varphi)\tan\beta}{R^2+q^2} \;+\; &\frac{R\cos\varphi}{\sqrt{R^2+q^2}} \\ &= \tan\chi\sin\varsigma\left(\sin\varphi + \frac{q\cos\varphi\tan\beta}{\sqrt{R^2+q^2}}\right). \end{aligned} \tag{4.109}$$

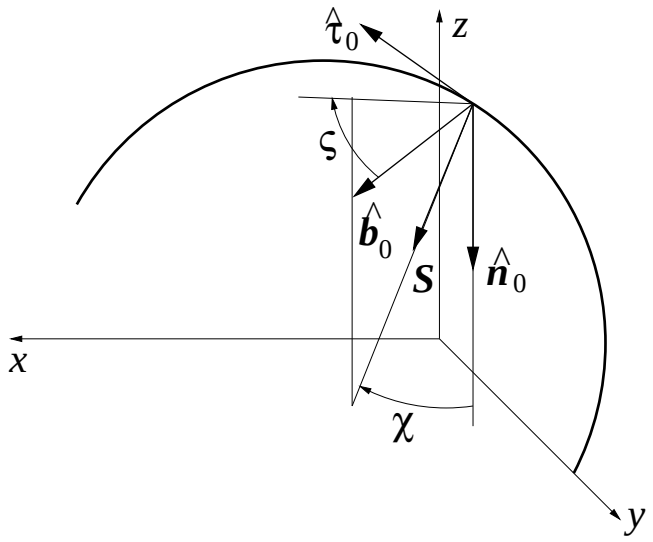


Figure 4.5: A sketch showing the introduction of angles $\chi$ and $\varsigma$. The thick arc represents the loop axis.

Eliminating $\tan\beta$ from equations (4.108) and (4.109) we obtain the equation for $\varphi$,

$$\begin{aligned} R\sin\varphi\tan\chi(q\cos\varsigma - R\sin\varsigma) + R\sqrt{R^2+q^2}\cos\varphi \\ - \quad q\tan\chi(R\cos\varsigma + q\sin\varsigma) = 0. \end{aligned} \tag{4.110}$$

If this equation does not have a solution satisfying $\varphi_0 \leq \varphi \leq \pi - \varphi_0$, then this means that, for any polarization angle $\beta$, we cannot have a node in the observation of the loop oscillation in its fundamental mode. This would be strong evidence supporting the conclusion that the observed oscillation is the first overtone.

Now assume that equation (4.110) does have a solution satisfying $\varphi_0 \leq \varphi \leq \pi - \varphi_0$. It is possible that there is more than one solution of equation (4.110) satisfying this condition, but we do not consider this case and assume that there is only one solution. After solving equation (4.110) to obtain a value for $\varphi$, we use equation (4.50) to find the position of the node on the loop, $s_{\rm th}$. Let $s_{\rm obs}$ be the position of the node found from the observation. If $|s_{\rm th} - s_{\rm obs}|$ is small enough, i.e. if it is within a specified interval, then it is strong evidence

supporting the conclusion that the observed oscillation is the fundamental mode, while the presence of the node is an observational effect. On the other hand, if $|s_{\rm th} - s_{\rm obs}|$ is larger than this interval, then it is evidence in favour of concluding that the observed oscillation is the first overtone.

We consider one example to demonstrate how the method works. Assume that we have observed a kink oscillation of a non-planar loop described by our model with $R = q$, $\varphi_0 = 0$ (so that the projection of the loop on the $yz$-plane is a semicircle), and the line-of-sight vector $\boldsymbol{S}$ is defined by $\chi = \pi/4$ and $\varsigma = \pi/3$. Then equation (4.110) reduces to

$$(1 - \sqrt{3}) \sin\varphi + 2\sqrt{2} \cos\varphi - (1 + \sqrt{3}) = 0. \tag{4.111}$$

The solution to this equation satisfying $0 < \varphi < \pi$ is

$$\varphi = \arcsin \frac{2\sqrt{4 - 2\sqrt{3}} - 1}{6 - \sqrt{3}} \approx 0.109, \tag{4.112}$$

so that $s_{\rm th} = \varphi L/\pi \approx 0.035L$. Hence, if $s_{\rm obs}$ is close to $0.035L$ then we conclude that the observed oscillation was the fundamental mode. If, on the other hand, there is a large difference between $s_{\rm obs}$ and $0.035L$, then we conclude that the observed oscillation was the first overtone.

In practice, this method may not be very easy to implement, unless we could obtain a 3D reconstruction of the loop. This would allow us to measure the observed position of the node and the loop apex more accurately. Furthermore, we can estimate $R$ by considering the projection of the loop reconstruction on the $yz$-plane, and fitting a circle to it as was done by Aschwanden et al. (2008) for the loops in figure 3.8. The radius of this circle would be equal to $R$. This circle would also show us how close the projection in the $yz$-plane is to being semicircular, which would allow us to estimate $\varphi_0$ and $z_0$ (see figure 3.6). In general, the loop footpoints have Cartesian coordinates given by equation (3.12), hence the distance between the footpoints, D, is

$$D = \sqrt{q^2(2\varphi_0 + \pi)^2 + 4(R^2 - {z_0}^2)}. \tag{4.113}$$

The distance between the footpoints can be measured from observational im-

ages, and assuming we can estimate $\varphi_0$ and $z_0$ as described above, we can use equation (4.113) to find an estimate for $q$, which gives us all of the loop parameters needed for equation (4.110). Finally, we would need to attempt to obtain values for the angles which define the line-of-sight vector, $\varsigma$ and $\chi$.

# Chapter 5

# Coronal Seismology using Non-Planar Coronal Loops

In section 1.3 we discussed coronal seismology, and how different properties of coronal loops can affect the results obtained via seismological theories. In particular, we considered methods of estimating the magnetic field strength inside a coronal loop and estimating the density scale height in the corona. In this chapter we consider the effects of our helical loop model on these seismological results. In section 5.1 we calculate the density scale height using kink oscillations of non-planar loops, and in section 5.2 we examine any change to the magnetic field strength estimates due to density stratification and loop non-planarity.

## 5.1 Estimation of the Density Scale Height

In section 4.3 we showed that the kink oscillation frequencies of a thin helical loop are given by the eigenvalue problem

$$\frac{d^2\Psi}{ds^2} + \frac{\omega^2}{c_k^2(s)}\Psi = 0, \qquad \Psi(0) = \Psi(L) = 0, \tag{5.1}$$

where

$$c_k^2(s) = \frac{2B^2}{\mu_0(\rho_i(s) + \rho_e(s))} \tag{5.2}$$

is the squared kink speed of the tube. The function $\Psi(s)$ determines the displacement of the loop axis, $\boldsymbol{\xi}$, as a function of $s$. We will consider a loop which

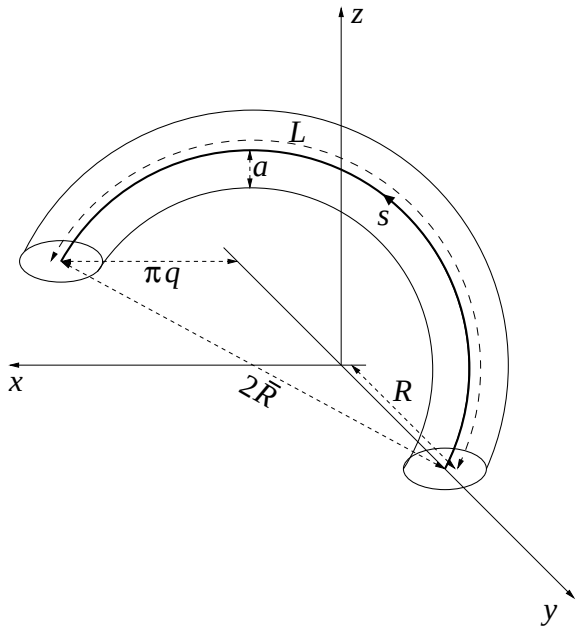


Figure 5.1: Helical loop geometry. Footpoints are anchored in the photosphere at the $xy$-plane, $z$ represents the height in the atmosphere, $s$ is the distance along the loop and $R$ is the radius of the semicircular loop projection on the $yz$-plane. $2\pi q$ is a measure of the pitch of the helix, although only half a turn of the helix is shown here to represent the loop.

has a semicircular projection on the $yz$-plane. Therefore $\varphi_0 = 0$ and, using equation (4.51), we find that $L = \pi R(1+\gamma^2)^{1/2}$. For the case of an unstratified loop $\rho_i$, $\rho_e$ and therefore $c_k^2$ are constant and equation (5.1) reduces to

$$\frac{d^2\Psi}{ds^2} + \frac{\omega^2}{c_k^2}\Psi = 0, \qquad \Psi(0) = \Psi(L) = 0, \tag{5.3}$$

which is a Sturm-Liouville problem, with a well known solution. Here the oscillation frequencies are given by

$$\omega_n = \frac{n\pi}{L}c_k, \tag{5.4}$$

where $n$ represents the mode, with $n = 1$ being the fundamental mode and $n = 2$ being the first overtone. Hence, we can see that the ratio between the period of the fundamental mode, $P_1$, and the period of the first overtone, $P_2$, is $P_1/P_2 = \omega_2/\omega_1 = 2$ for an unstratified loop.

Here we consider the case where density is not constant, and assume that the densities inside and outside the loop vary along the length of the loop, but not in the radial direction. We also assume that the stratification is uniform, which implies that the ratio between these two densities is constant, such that $\rho_i(s)/\rho_e(s) = \zeta > 1$. We model the stratified atmosphere by using an exponential density profile, $\rho(z)$, which decreases with height and assume it has the form

$$\rho(z) = \rho_f \exp\left(-\frac{z}{H}\right), \tag{5.5}$$

where $\rho_f$ is the density at the footpoints and $H$ is the density scale height. We project this onto our non-planar loop geometry by using the relation

$$z(s) = R\sin\left(\frac{s}{\sqrt{q^2+R^2}}\right) = R\sin\left(\frac{s}{R\sqrt{1+\gamma^2}}\right). \tag{5.6}$$

Therefore the density profile along the loop is given by

$$\rho_i(s) = \rho_f \exp\left[-\frac{R}{H}\sin\left(\frac{s}{R\sqrt{1+\gamma^2}}\right)\right]. \tag{5.7}$$

The density profile can now be substituted into equation (5.1) and the eigenvalue problem for this situation becomes

$$\frac{d^2\Psi}{ds^2} + \frac{\omega^2}{c_{kf}^2}\exp\left[-\frac{R}{H}\sin\left(\frac{s}{R\sqrt{1+\gamma^2}}\right)\right]\Psi = 0, \qquad \Psi(0) = \Psi(L) = 0, \tag{5.8}$$

where $c_{kf}^2 = 2\zeta B^2/\mu_0\rho_f(1+\zeta)$ is the squared kink speed at the footpoints. This equation can be non-dimensionalized by introducing the dimensionless frequency $\Omega$ and length $S$

$$\Omega^2 = \frac{\pi^2\omega^2R^2(1+\gamma^2)}{c_{kf}^2}, \qquad S = \frac{s}{L}, \tag{5.9}$$

which allows us to write equation (5.8) as

$$\frac{d^2\Psi}{dS^2} + \Omega^2\exp\left(-\frac{R}{H}\sin(\pi S)\right)\Psi = 0, \qquad \Psi(0) = \Psi(1) = 0. \tag{5.10}$$

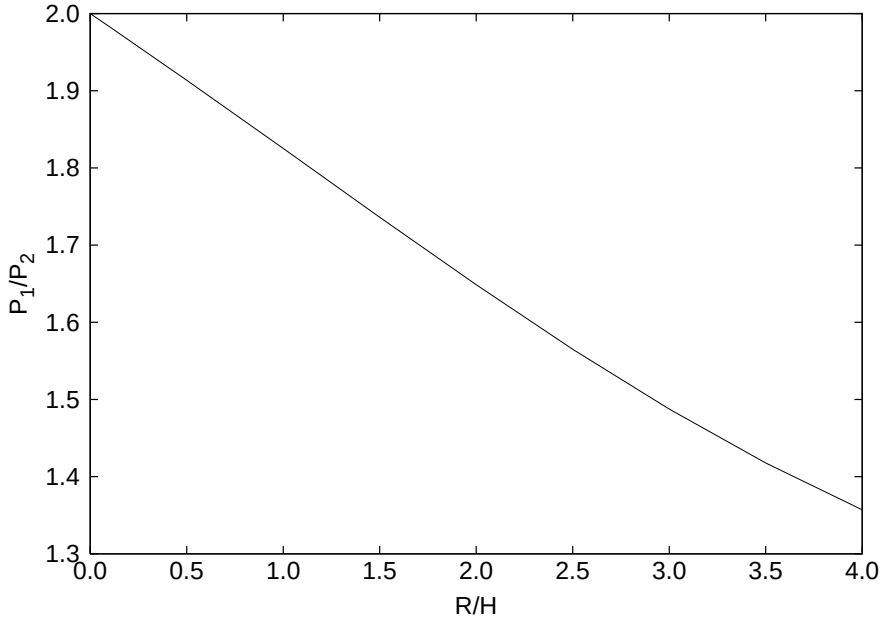


Figure 5.2: The ratio, $P_1/P_2$, of the periods of the fundamental mode and first overtone of a kink oscillation of a non-planar loop. This is unaffected by the non-planarity of the loop and therefore agrees with the results for a semicircular loop as given by Andries et al. (2005a), Dymova and Ruderman (2006) and Morton and Erdélyi (2009a).

This equation can be solved numerically using the shooting method to obtain the dimensionless frequencies $\Omega_1$ and $\Omega_2$ for the fundamental mode and first overtone, respectively.[1] Since equation (5.10) does not contain the non-planarity parameter $\gamma$, it follows that $\Omega_1$ and $\Omega_2$ are independent of $\gamma$. Subsequently, we can also state that the period ratio $P_1/P_2 = \Omega_2/\Omega_1$ is independent of $\gamma$. Therefore we conclude that the non-planarity does not affect estimates of the density scale height, at least not for loops which can be described by our helical model when $z_0 = 0$. Nevertheless, the results did show that the period ratio decreases from the expected value of two as $R/H$ increases. These results are shown in figure 5.2 and agree with the results found by Andries et al. (2005a, Figure 1b), (Dymova and Ruderman, 2006, Figure 4) and (Morton and Erdélyi, 2009a, Figure 3b) for the case of a semicircular loop. Note that the dimensional frequencies of the fundamental mode and first overtone, $\omega_1$ and $\omega_2$, do depend

[1]The source code used to implement the shooting method can be seen in appendix B.

on $\gamma$. It is also important to remember that these results apply for linearized MHD because the governing equation for the system, equation (5.1), was derived using the linearized MHD equations.

## 5.2 Estimation of the Magnetic Field Strength

Next we move on to study the effect of density stratification and loop non-planarity on the estimation of the magnetic field strength inside the loop. To obtain an equation for the magnetic field strength, we take the definition of $\Omega$ from equation (5.9) and combine it with equation (5.2) to eliminate $c_k^2$. We can then introduce $\omega = 2\pi/P$ and rearrange to find $B$, which gives

$$B = \frac{\pi^2 R}{\Omega P}\sqrt{\frac{2\mu_0\rho_f(1+\zeta)(1+\gamma^2)}{\zeta}}. \tag{5.11}$$

Here $\Omega$ is the dimensionless frequency of the fundamental mode of a kink oscillation, which can be obtained from equation (5.10), and $P$ is the observed period of the fundamental mode. Observationally, it is easier to obtain the distance between the footpoints, $2\bar{R}$, rather than $R$. These distances are related by

$$\bar{R} = R\sqrt{1+\pi^2\gamma^2/4}, \tag{5.12}$$

and we use this to write equation (5.11) as

$$B = \frac{2\pi^2 \bar{R}}{\Omega P}\sqrt{\frac{2\mu_0\rho_f(1+\zeta)(1+\gamma^2)}{\zeta(4+\pi^2\gamma^2)}}. \tag{5.13}$$

Equation (5.13) gives the magnetic field strength in Tesla. We can define a non-dimensional magnetic field strength as

$$\tilde{B} = \frac{BP}{\bar{R}\sqrt{\mu_0\rho_a}} = \frac{2\pi^2 e^{R/2H}}{\Omega}\sqrt{\frac{2(1+\zeta)(1+\gamma^2)}{\zeta(4+\pi^2\gamma^2)}}, \tag{5.14}$$

where $\rho_a = \rho_f \exp(-R/H)$ is the plasma density at the loop apex. For $\zeta = 10$, figure 5.3 shows the dependence of $\tilde{B}$ on $R/H$, the ratio of the loop height to the density scale height, for different values of the non-planarity parameter $\gamma$. We

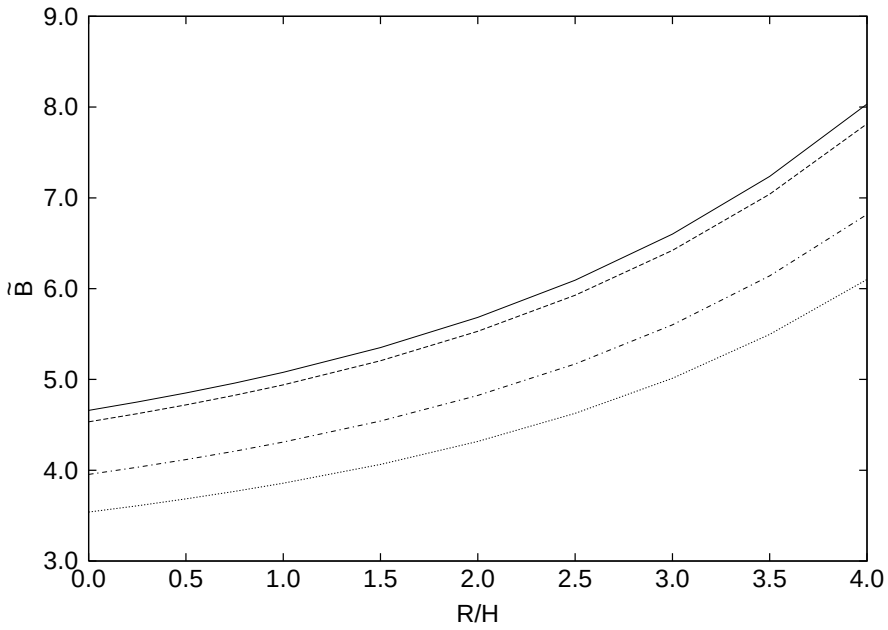


Figure 5.3: The dimensionless magnetic field strength, $\tilde{B}$, inside the coronal loop as a function of $R/H$ for various values of the non-planarity parameter $\gamma$. Here $\zeta = 10$ and the solid, dashed, dashed-dotted and dotted lines correspond to $\gamma = 0$, 0.2, 0.6 and 1, respectively.

see that, for a loop with a given non-planarity, as $R/H$ increases, the estimate of the magnetic field strength also increases. Conversely, if $R/H$ is kept constant and $\gamma$ is increased, then the magnetic field strength estimate decreases. The ratio of the internal and external densities $\zeta$, which is also known as the density contrast, is another parameter which can be varied. The density contrast is not the same for all loops, and several loops considered by Aschwanden (2001) were estimated to have densities in the range $8 \leq \zeta \leq 18$. The effect of varying the density contrast can be seen in figure 5.4, where $\gamma = 0$ and we have chosen the range of densities to be $1.5 \leq \zeta \leq 20$, using the loops discussed by Aschwanden (2001) as a guide. Figure 5.4 shows that as the density contrast is increased, the magnetic field strength estimate decreases. However, if we examine the form of equation (5.14) and allow the density contrast to increase beyond our chosen range, we see that the magnetic field strength estimate tends towards a

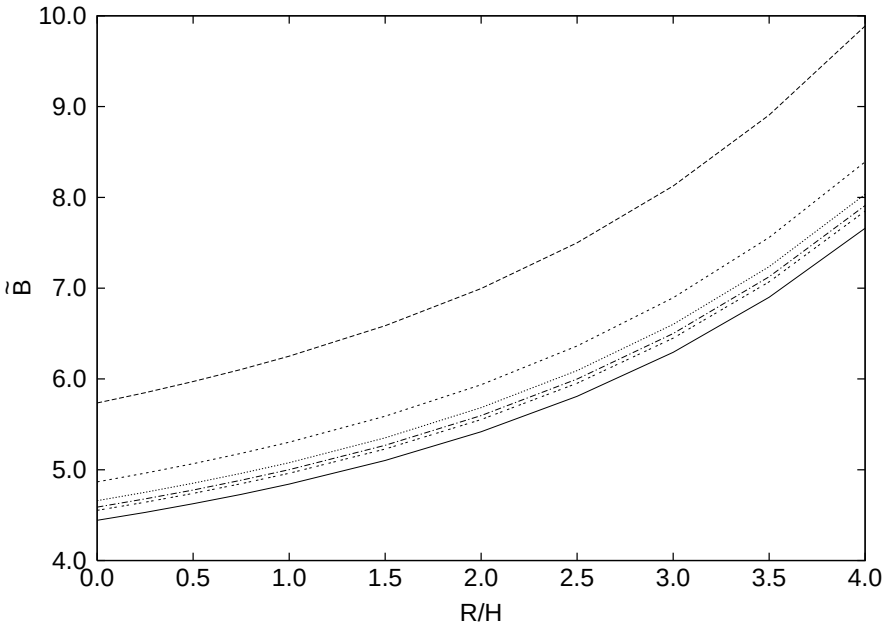


Figure 5.4: The dimensionless magnetic field strength, $\tilde{B}$, inside the coronal loop as a function of $R/H$ for various values of the density contrast $\zeta$. Here $\gamma = 0$ and the dashed, short-dashed, dotted, dashed-dotted and double-dashed lines correspond to $\zeta = 1.5$, 5, 10, 15 and 20, respectively. The solid line represents the lowest value of the magnetic field strength estimate, as given in equation (5.16).

particular value. Rewriting equation (5.14) in the form

$$\tilde{B} = \frac{2\pi^2 e^{R/2H}}{\Omega} \sqrt{\left(\frac{2(1+\gamma^2)}{4+\pi^2\gamma^2}\right)\left(1+\frac{1}{\zeta}\right)}, \tag{5.15}$$

and looking at the limit when $\zeta$ is large, we find that

$$\lim_{\zeta\to\infty} \tilde{B} = \frac{2\pi^2 e^{R/2H}}{\Omega} \sqrt{\frac{2(1+\gamma^2)}{4+\pi^2\gamma^2}}. \tag{5.16}$$

For a loop with a given non-planarity, this function represents the lowest estimate for the magnetic field strength that can be obtained using this model.

As an example, we apply equation (5.13) to an event also considered by Nakariakov and Ofman (2001). The oscillating loop was observed on the 4th of July 1999, the half-distance between its footpoints was measured to be $\bar{R} =$

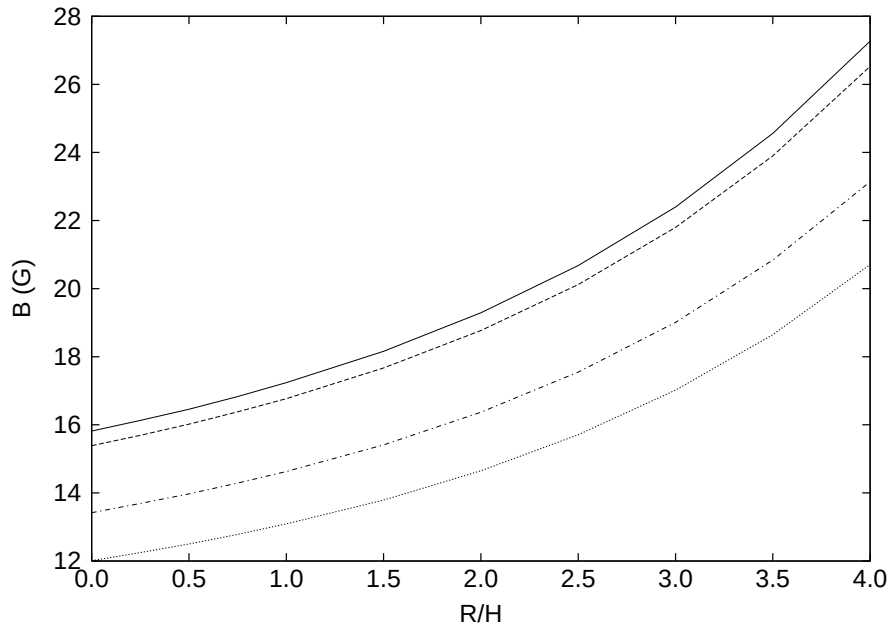


Figure 5.5: The magnetic field strength inside a coronal loop as a function of $R/H$, for the oscillation event observed on the 4th of July 1999. The results are plotted for several values of the non-planarity parameter $\gamma$. Here $\zeta = 10$ and the solid, dashed, dashed-dotted and dotted lines correspond to $\gamma = 0$, 0.2, 0.6 and 1, respectively. Note that the magnetic field strength, B, is given in Gauss, where 1 T $= 10^4$ G.

$6.0 \times 10^7$ m and the period of the fundamental mode was $P = 360$ s. Following Nakariakov and Ofman (2001) we take $\zeta = 10$ and $\rho_a = 3.3 \times 10^{-12}$ kg m$^{-3}$. The estimate of the magnetic field strength inside this loop is shown in figure 5.5 for different values of the non-planarity parameter $\gamma$. It is useful to look at some specific values from this figure so that we can easily compare the results found here with those found previously.

First we consider the unstratified planar case where $R/H = 0$ and $\gamma = 0$. In this case $\Omega = \pi$ and using equation (5.13) we find that $B \approx 16$ G, which agrees well with the estimate of $B = 13 \pm 9$ G given by Nakariakov and Ofman (2001). (Note that 1 Tesla $= 10^4$ Gauss.) Next we take $R/H = 1$, which is a reasonable value for a loop that has a distance of $1.2 \times 10^8$ m between its footpoints and a plasma temperature of about $10^6$ K. The numerical solution of equation (5.10) with $R = H$ gives $\Omega \approx 4.8$. Substituting these values and $\zeta = 10$ into equation

(5.13) gives

$$B \approx 1.7 \times 10^{-3} \sqrt{\frac{1+\gamma^2}{1+\pi^2\gamma^2/4}}, \tag{5.17}$$

where, once again, the value of $B$ is measured in Tesla. Using this equation we find that, when $\gamma = 0$, $B \approx 17$ G, while for $\gamma = 1$ we obtain $B \approx 13$ G. On comparison with the unstratified planar estimate of $B \approx 16$ G, we see that the variation of the estimate of the magnetic field strength caused by accounting for the stratification and non-planarity is less than 20% for these typical loop parameters. Therefore, we conclude that the effects of density variation along the loop and loop non-planarity are weak. This suggests that the model used by Nakariakov and Ofman (2001) provides a sufficient estimate of the magnetic field strength inside the loop, even though it assumes the simplest model of a coronal loop in the form of a straight homogeneous cylindrical magnetic tube.

# Chapter 6

# Discussion

As was discussed in chapter 1 there have been many models of coronal loops, which investigated their many different physical features. The coronal loop model which was introduced in this thesis was defined such that it had non-zero curvature and torsion. We found that the main effect of including loop torsion in the loop model is that it changes the polarization of the kink oscillations. This could lead to an observational effect being produced, such that the fundamental kink mode appears to have a node at some point along the loop other than at the footpoints. There has only been one such oscillation, that we know of, which could possibly show this phenomenon. However, the spatial structure of oscillating loops is not usually considered during the analysis of these events, therefore it is possible that other oscillations of this type have been overlooked.

The oscillation was excited by a blast wave from a nearby flare and was observed by TRACE on the 13th of May 2001. It was reported by Schrijver et al. (2002) and interpreted by De Moortel and Brady (2007). De Moortel and Brady (2007) found that the oscillation contained two harmonics, one which had a period of 577-672 s, and another which had a period of 250-346 s. Their analysis showed that the harmonic with the larger period was the more prominent of the two. This harmonic was found to have a larger amplitude in the loop legs than at a point near the loop apex. Therefore this point appeared to be a node. This fact, combined with the oscillations in the loop legs being out of phase, led De Moortel and Brady (2007) to classify the oscillation as the first overtone of a standing kink oscillation. This makes the oscillation unusual because in the majority of other observations of coronal loop kink oscillations, the fundamental

mode is seen to be the dominant harmonic rather than the first overtone. But in this case it does not appear to have been excited. De Moortel and Brady (2007) then proceed to consider why this might be the case. One suggestion is that it was due to the blast wave not hitting the loop centrally. They suggest that since the loop was positioned at an angle to the flare site, it is possible that the fundamental mode was not excited initially, and damped before it had time to become fully established. They also discuss the possibility of the loop geometry having an effect on the oscillation, and point out that the loop has "a kind of S-shape." They say that the loop geometry, combined with unknown projection effects, could result in the fundamental mode looking like a first overtone. This description matches reasonably well with the situation we described in section 4.5, which suggests that this loop could possibly be displaying the fundamental kink mode of a non-planar loop oscillation. However, before we could know for sure if this was the case, we would need to observe more oscillations of this type, with an aim of testing the method introduced in section 4.5. With the current fleet of sophisticated spacecraft, such as STEREO and SDO, watching the Sun as it approaches a maximum in its activity cycle maybe this will become a possibility.

To aid with the identification of non-planar loop oscillations it could also be useful to consider how they would look in a time series of images, in the same way as Wang et al. (2008) have done for planar loop oscillations. In their paper Wang et al. (2008) model several loops and then "observe" them from different angles to find out what the observational signatures of different types of oscillations would be. They then compare these to actual observations with an aim of identifying the mode of oscillation. Interestingly, Wang et al. (2008) also considered the same loop as discussed by De Moortel and Brady (2007). Using the methods described in their paper, they classify the oscillation as a fundamental vertical kink oscillation. However, this conclusion is based on an analysis by Aschwanden et al. (2002), which assumes that the apparent node is in fact a footpoint. Later, Wang et al. (2008) consider combinations of modes and find that the oscillation could possibly be a combination of the fundamental horizontal and vertical modes. This links back to the observations reported by Aschwanden (2009) discussed in section 1.2. Aschwanden (2009) found that reconstructing the 3D motion of coronal loop oscillations revealed horizontal

and vertical motions. He said that these vertical and horizontal motions could be linked to form a circularly polarized oscillation if the loop has a helical shape. If the 13th of May 2001 oscillation event does indeed show both vertical and horizontal motions, then this could be additional evidence to support our theory that the oscillation is the fundamental mode of a non-planar loop kink oscillation.

# Chapter 7

# Conclusions and Future Work

In this thesis we have introduced a non-planar model of a coronal loop. Motivation for studying non-planar loops was provided by the 3D reconstruction of coronal loop geometries carried out by Aschwanden et al. (2008) and Aschwanden (2009). These reconstructions revealed several loops that did not lie in a plane, which suggested investigating loops of this type.

The coronal loop model constructed here was based on helical geometry and had non-zero curvature and torsion. In this model a loop was formed from helical field lines and had a constant circular cross-section. The radius of the loop cross-section was defined to be much smaller than the loop curvature radius. The background magnetic field was force-free, and field lines twisted around the central loop axis. We assumed that the atmosphere was stratified and allowed the density, both inside and outside the loop, to vary along the length of the loop, but not in the radial direction.

On comparison with the observations reported by Aschwanden et al. (2008) and Aschwanden (2009), we found that our loop model is most useful for describing loops that have a small or moderate value of the non-planarity parameter. This would correspond to $\gamma \leq 1$. Since Aschwanden (2009) has observed a loop that is outside this range, this suggests that studying other non-planar loop models could be worthwhile.

We devised a set of curvilinear coordinates, which used the loop axis as a coordinate line and the loop boundary as a coordinate surface. Using this coordinate system and the linearized ideal MHD equations, we derived the governing equation for kink oscillations of the loop. We found that the governing

equation is identical to the governing equation of a straight loop with density varying along the tube, as found by Dymova and Ruderman (2005). Therefore we conclude that the curvature and torsion of a coronal loop do not directly affect the eigenfrequencies of the kink oscillations of the loop. However, the loop non-planarity will still affect the eigenfrequencies indirectly via modifications to the density profile along the length of the loop. We found that the main effect of the loop torsion is that it alters the polarization of oscillations. We found that, for a loop with non-zero torsion, the direction of polarization rotates with the principal normal as we move along the loop. We have considered how non-planar loop oscillations would appear in observations. In the case of a fundamental kink oscillation there are only nodes at the loop footpoints. However, since the direction of polarization varies along the loop, the oscillation would also appear to have a node at the point where it is polarized in the direction parallel to the line of sight. Here we have presented a method to distinguish these oscillations from the first overtone, which also contains a node.

We have also examined the effects of our helical loop model on the results of coronal seismology. Firstly, we considered the estimate of the density scale height in the corona found using the ratio of periods of the fundamental harmonic and first overtone of kink oscillations. We found that, at least for the model used here, the non-planarity of the loop does not affect the period ratio, and therefore does not influence estimates of the density scale height. Secondly, we investigated the effect of loop non-planarity and density stratification on the estimates of the magnetic field strength. We found that including these features does change the estimate of the magnetic field strength, and that the variation due to density stratification is larger than the variation due to loop non-planarity. However, for typical loop parameters, the difference in the magnetic field strength estimate was less than 20% from the estimate obtained by modelling the loop as a straight cylinder, as found by Nakariakov and Ofman (2001). Therefore we conclude that modelling the loop as a straight cylinder is likely to be sufficient when estimating the magnetic field strength.

There are several ways in which this work could be continued in the future. Firstly, it would be useful to search for more observational evidence of non-planar coronal loop oscillations, so that the model we have introduced here can be checked against observational data. Secondly, the current loop model could

be extended in a number of different ways. Two examples include: examining loops with $z_0 \neq 0$ in more detail and including other features of loop geometry, such as changing the shape of the loop cross-section. Finally, different non-planar loop models could be investigated, with an aim of describing loops with $\gamma > 1$ or loops that do not have constant curvature.

# Appendix A

# Extended Derivations from Chapter 4

This appendix contains further details for some of the derivations that were presented in chapter 4.

## A.1 Curvilinear Coordinates

To find the expressions for the Cartesian coordinates in terms of $r$, $\theta$ and $\varphi$, we start with equation (4.15), which is repeated below,

$$\bar{x} = q(\bar{\varphi}' - \varphi_c') + \frac{Rr\cos\theta}{\sqrt{R^2+q^2}}, \qquad \bar{y} = \varpi_0 \cos\bar{\varphi}', \qquad \bar{z} = \varpi_0 \sin\bar{\varphi}', \tag{A.1}$$

and substitute in equations (4.17) and (4.22), which are repeated below,

$$\varpi_0 \approx R + r\sin\theta, \qquad \varphi_c' \approx -\frac{qr\cos\theta}{R\sqrt{R^2+q^2}}, \tag{A.2}$$

$$\bar{\varphi}' \approx \bar{\varphi} - \frac{qr\cos\theta}{R\sqrt{R^2+q^2}}. \tag{A.3}$$

The $\bar{x}$ component is the most straightforward and on substitution of the above approximations we obtain

$$\begin{aligned}\bar{x} &\approx q\left(\bar{\varphi} - \frac{qr\cos\theta}{R\sqrt{R^2+q^2}} + \frac{qr\cos\theta}{R\sqrt{R^2+q^2}}\right) + \frac{Rr\cos\theta}{\sqrt{R^2+q^2}} \\ &\approx q\bar{\varphi} + \frac{Rr\cos\theta}{\sqrt{R^2+q^2}}.\end{aligned} \tag{A.4}$$

Next, we consider the $\bar{y}$ coordinate, which becomes

$$\bar{y} \approx (R + r\sin\theta)\cos\left(\bar{\varphi} - \frac{qr\cos\theta}{R\sqrt{R^2+q^2}}\right) \tag{A.5}$$

on substitution of equations (A.2) and (A.3). Then, using the trigonometric identity $\cos(A-B) = \cos A\cos B + \sin A\sin B$, we can write

$$\bar{y} \approx (R + r\sin\theta)\left[\cos\bar{\varphi}\cos\left(\frac{qr\cos\theta}{R\sqrt{R^2+q^2}}\right) + \sin\bar{\varphi}\sin\left(\frac{qr\cos\theta}{R\sqrt{R^2+q^2}}\right)\right]. \tag{A.6}$$

To linearize this equation with respect to $r$, we need to linearize the sine and cosine terms that depend on $r$. Since $qr\cos\theta \ll R\sqrt{R^2+q^2}$, this can be done by using the following approximations

$$\sin A \approx A, \qquad \cos A \approx 1, \tag{A.7}$$

to give,

$$\bar{y} \approx (R + r\sin\theta)\left(\cos\bar{\varphi} + \frac{qr\cos\theta\sin\bar{\varphi}}{R\sqrt{R^2+q^2}}\right). \tag{A.8}$$

Then, after expanding the brackets we obtain

$$\bar{y} \approx R\cos\bar{\varphi} + r\sin\theta\cos\bar{\varphi} + \frac{qr\cos\theta\sin\bar{\varphi}}{\sqrt{R^2+q^2}} + \frac{qr^2\sin\theta\cos\theta\sin\bar{\varphi}}{R\sqrt{R^2+q^2}}. \tag{A.9}$$

Here the final term can be dropped since it is quadratic in $r$. Finally, we obtain

$$\bar{y} \approx R\cos\bar{\varphi} + r\sin\theta\cos\bar{\varphi} + \frac{qr\cos\theta\sin\bar{\varphi}}{\sqrt{R^2+q^2}}. \tag{A.10}$$

The third coordinate $\bar{z}$ becomes

$$\bar{z} \approx (R + r\sin\theta)\sin\left(\bar{\varphi} - \frac{qr\cos\theta}{R\sqrt{R^2+q^2}}\right), \tag{A.11}$$

on substitution of equations (A.2) and (A.3). Then, using the trigonometric identity $\sin(A-B) = \sin A\cos B - \cos A\sin B$, we can write

$$\bar{z} \approx (R + r\sin\theta)\left[\sin\bar{\varphi}\cos\left(\frac{qr\cos\theta}{R\sqrt{R^2+q^2}}\right) - \cos\bar{\varphi}\sin\left(\frac{qr\cos\theta}{R\sqrt{R^2+q^2}}\right)\right]. \tag{A.12}$$

Again, the non-linear sine and cosine terms can be linearized by using equation (A.7) to give,

$$\bar{z} \approx (R + r\sin\theta)\left(\sin\bar{\varphi} - \frac{qr\cos\theta\cos\bar{\varphi}}{R\sqrt{R^2+q^2}}\right). \tag{A.13}$$

After expanding the brackets we obtain

$$\bar{z} \approx R\sin\bar{\varphi} + r\sin\theta\sin\bar{\varphi} - \frac{qr\cos\theta\cos\bar{\varphi}}{\sqrt{R^2+q^2}} - \frac{qr^2\sin\theta\cos\theta\cos\bar{\varphi}}{R\sqrt{R^2+q^2}}, \tag{A.14}$$

where the final term can be dropped since it is quadratic in $r$. Finally, we obtain

$$\bar{z} \approx R\sin\bar{\varphi} + r\sin\theta\sin\bar{\varphi} - \frac{qr\cos\theta\cos\bar{\varphi}}{\sqrt{R^2+q^2}}. \tag{A.15}$$

After dropping the bar, we can summarize these coordinates as:

$$x = q\varphi + \frac{Rr\cos\theta}{\sqrt{R^2+q^2}} + \mathcal{O}(\varepsilon^2), \tag{A.16}$$

$$y = R\cos\varphi + r\sin\theta\cos\varphi + \frac{qr\cos\theta\sin\varphi}{\sqrt{R^2+q^2}} + \mathcal{O}(\varepsilon^2), \tag{A.17}$$

$$z = R\sin\varphi + r\sin\theta\sin\varphi - \frac{qr\cos\theta\cos\varphi}{\sqrt{R^2+q^2}} + \mathcal{O}(\varepsilon^2), \tag{A.18}$$

where $\varepsilon = a/R$ and $\mathcal{O}(\varepsilon^2)$ indicates higher terms with respect to $r$ starting from quadratic.

## A.2 Derivation of Scale Factors

This appendix contains the derivation of the scale factors given in equation (4.38). We use equations (4.35) to (4.37) to evaluate equation (4.34), starting with $h_\sigma$:

$$\begin{aligned}
h_\sigma &= \left|\frac{\partial \boldsymbol{X}}{\partial \sigma}\right| = \left[\left(\frac{\partial x}{\partial \sigma}\right)^2 + \left(\frac{\partial y}{\partial \sigma}\right)^2 + \left(\frac{\partial z}{\partial \sigma}\right)^2\right]^{1/2} \\
&= \left[\varepsilon^2 R^2 \frac{R^2\cos^2\theta}{R^2+q^2} + \varepsilon^2 R^2 \left(\sin\theta\cos\varphi + \frac{q\cos\theta\sin\varphi}{\sqrt{R^2+q^2}}\right)^2 \right. \\
&\qquad \left. + \varepsilon^2 R^2 \left(\sin\theta\sin\varphi - \frac{q\cos\theta\cos\varphi}{\sqrt{R^2+q^2}}\right)^2 + \mathcal{O}(\varepsilon^3)\right]^{1/2} \\
&= \left[\varepsilon^2 R^2 \left(\frac{R^2\cos^2\theta}{R^2+q^2} + \sin^2\theta\cos^2\varphi + \frac{q^2\cos^2\theta\sin^2\varphi}{R^2+q^2}\right.\right. \\
&\qquad + \frac{2q\sin\theta\cos\varphi\cos\theta\sin\varphi}{\sqrt{R^2+q^2}} + \sin^2\theta\sin^2\varphi \\
&\qquad \left.\left. + \frac{q^2\cos^2\theta\cos^2\varphi}{R^2+q^2} - \frac{2q\sin\theta\sin\varphi\cos\theta\cos\varphi}{\sqrt{R^2+q^2}}\right) + \mathcal{O}(\varepsilon^3)\right]^{1/2}. \qquad \text{(A.19)}
\end{aligned}$$

Then, making use of the identity $\sin^2\varphi + \cos^2\varphi = 1$, we find that the above equation simplifies to:

$$\begin{aligned}
h_\sigma &= \left[\varepsilon^2 R^2 \left(\frac{R^2\cos^2\theta}{R^2+q^2} + \sin^2\theta + \frac{q^2\cos^2\theta}{R^2+q^2}\right) + \mathcal{O}(\varepsilon^3)\right]^{1/2} \\
&= \left[\varepsilon^2 R^2(\cos^2\theta + \sin^2\theta) + \mathcal{O}(\varepsilon^3)\right]^{1/2} \\
&= \left[\varepsilon^2 R^2 + \mathcal{O}(\varepsilon^3)\right]^{1/2}. \qquad \text{(A.20)}
\end{aligned}$$

We can simplify this further by using the binomial expansion, such that

$$\begin{aligned} h_\sigma &= \varepsilon R\left[1+\frac{\mathcal{O}(\varepsilon^3)}{\varepsilon^2 R^2}\right]^{1/2} \\ &\approx \varepsilon R\left[1+\frac{\mathcal{O}(\varepsilon^3)}{2\varepsilon^2 R^2}\right] \\ &\approx \varepsilon R+\frac{\mathcal{O}(\varepsilon^3)}{2\varepsilon R} \\ &\approx \varepsilon R+\mathcal{O}(\varepsilon^2). \end{aligned} \tag{A.21}$$

Using a similar method, we can obtain an expression for $h_\theta$:

$$\begin{aligned} h_\theta &= \left|\frac{\partial \boldsymbol{X}}{\partial\theta}\right| = \left[\left(\frac{\partial x}{\partial\theta}\right)^2+\left(\frac{\partial y}{\partial\theta}\right)^2+\left(\frac{\partial z}{\partial\theta}\right)^2\right]^{1/2} \\ &= \left[\varepsilon^2\sigma^2R^2\left(\frac{R^2\sin^2\theta}{R^2+q^2}+\left(\cos\theta\cos\varphi-\frac{q\sin\theta\sin\varphi}{\sqrt{R^2+q^2}}\right)^2\right.\right. \\ &\qquad \left.\left.+\left(\cos\theta\sin\varphi+\frac{q\sin\theta\cos\varphi}{\sqrt{R^2+q^2}}\right)^2\right)+\mathcal{O}(\varepsilon^3)\right]^{1/2} \\ &= \left[\varepsilon^2\sigma^2R^2\left(\frac{R^2\sin^2\theta}{R^2+q^2}+\cos^2\theta\cos^2\varphi+\frac{q^2\sin^2\theta\sin^2\varphi}{R^2+q^2}\right.\right. \\ &\qquad -\frac{2q\cos\theta\cos\varphi\sin\theta\sin\varphi}{\sqrt{R^2+q^2}}+\cos^2\theta\sin^2\varphi \\ &\qquad \left.\left.+\frac{q^2\sin^2\theta\cos^2\varphi}{R^2+q^2}+\frac{2q\cos\theta\sin\varphi\sin\theta\cos\varphi}{\sqrt{R^2+q^2}}\right)+\mathcal{O}(\varepsilon^3)\right]^{1/2}. \end{aligned} \tag{A.22}$$

Then, making use of the identity $\sin^2\varphi+\cos^2\varphi=1$, we find that the above

equation simplifies to:

$$\begin{aligned}
h_\theta &= \left[\varepsilon^2\sigma^2R^2\left(\frac{R^2\sin^2\theta}{R^2+q^2}+\cos^2\theta+\frac{q^2\sin^2\theta}{R^2+q^2}\right)+\mathcal{O}(\varepsilon^3)\right]^{1/2}\\
&= \left[\varepsilon^2\sigma^2R^2(\sin^2\theta+\cos^2\theta)+\mathcal{O}(\varepsilon^3)\right]^{1/2}\\
&= \left[\varepsilon^2\sigma^2R^2+\mathcal{O}(\varepsilon^3)\right]^{1/2}\\
&= \varepsilon\sigma R\left[1+\frac{\mathcal{O}(\varepsilon^3)}{\varepsilon^2\sigma^2R^2}\right]^{1/2}\\
&\approx \varepsilon\sigma R\left[1+\frac{\mathcal{O}(\varepsilon^3)}{2\varepsilon^2\sigma^2R^2}\right]\\
&\approx \varepsilon\sigma R+\frac{\mathcal{O}(\varepsilon^3)}{2\varepsilon\sigma R}\\
&\approx \varepsilon\sigma R+\mathcal{O}(\varepsilon^2). \qquad \text{(A.23)}
\end{aligned}$$

Finally, we repeat the above method for $h_\varphi$:

$$\begin{aligned}
h_\varphi &= \left|\frac{\partial \boldsymbol{X}}{\partial\varphi}\right| = \left[\left(\frac{\partial x}{\partial\varphi}\right)^2+\left(\frac{\partial y}{\partial\varphi}\right)^2+\left(\frac{\partial z}{\partial\varphi}\right)^2\right]^{1/2}\\
&= \left[q^2+\left(-R\sin\varphi-\varepsilon\sigma R\sin\theta\sin\varphi+\frac{q\varepsilon\sigma R\cos\theta\cos\varphi}{\sqrt{R^2+q^2}}\right)^2\right.\\
&\qquad \left.+\left(R\cos\varphi+\varepsilon\sigma R\sin\theta\cos\varphi+\frac{q\varepsilon\sigma R\cos\theta\sin\varphi}{\sqrt{R^2+q^2}}\right)^2+\mathcal{O}(\varepsilon^3)\right]^{1/2}, \qquad \text{(A.24)}
\end{aligned}$$

$$
\begin{aligned}
h_\varphi &= \Bigg[q^2 + R^2\sin^2\varphi + 2\varepsilon\sigma R^2\sin\theta\sin^2\varphi - \frac{2q\varepsilon\sigma R^2\cos\theta\cos\varphi\sin\varphi}{\sqrt{R^2+q^2}} \\
&\quad + \varepsilon^2\sigma^2R^2\sin^2\theta\sin^2\varphi - \frac{2q\varepsilon^2\sigma^2R^2\cos\theta\cos\varphi\sin\theta\sin\varphi}{\sqrt{R^2+q^2}} \\
&\quad + \frac{q^2\varepsilon^2\sigma^2R^2\cos^2\theta\cos^2\varphi}{R^2+q^2} + R^2\cos^2\varphi + 2\varepsilon\sigma R^2\sin\theta\cos^2\varphi \\
&\quad + \frac{2q\varepsilon\sigma R^2\cos\theta\sin\varphi\cos\varphi}{\sqrt{R^2+q^2}} + \varepsilon^2\sigma^2R^2\sin^2\theta\cos^2\varphi \\
&\quad + \frac{2q\varepsilon^2\sigma^2R^2\cos\theta\sin\varphi\sin\theta\cos\varphi}{\sqrt{R^2+q^2}} + \frac{q^2\varepsilon^2\sigma^2R^2\cos^2\theta\sin^2\varphi}{R^2+q^2} + \mathcal{O}(\varepsilon^3)\Bigg]^{1/2} \\
&= \Bigg[q^2 + R^2 + 2\varepsilon\sigma R^2\sin\theta + \varepsilon^2\sigma^2R^2\sin^2\theta + \frac{q^2\varepsilon^2\sigma^2R^2\cos^2\theta}{R^2+q^2} + \mathcal{O}(\varepsilon^3)\Bigg]^{1/2}.
\end{aligned}
\tag{A.25}
$$

To leading order in $\varepsilon$, the above equation can be written as

$$
h_\varphi = \left[R^2 + q^2 + \mathcal{O}(\varepsilon)\right]^{1/2}. \tag{A.26}
$$

Then, continuing as above, we obtain

$$
\begin{aligned}
h_\varphi &= \sqrt{R^2+q^2}\left[1 + \frac{\mathcal{O}(\varepsilon)}{R^2+q^2}\right]^{1/2} \\
&\approx \sqrt{R^2+q^2}\left[1 + \frac{\mathcal{O}(\varepsilon)}{2(R^2+q^2)}\right] \\
&\approx \sqrt{R^2+q^2} + \frac{\mathcal{O}(\varepsilon)}{2\sqrt{R^2+q^2}} \\
&\approx \sqrt{R^2+q^2} + \mathcal{O}(\varepsilon).
\end{aligned}
\tag{A.27}
$$

## A.3 Derivation of the Governing Equation

To proceed with the derivation of the governing equation, we first consider the unscaled version of equation (4.74):

$$-r\frac{\partial^2}{\partial t^2}\left(\frac{\partial \psi}{\partial r}\right) = v_A^2\left(-r\frac{\partial^2}{\partial s^2}\frac{\partial \psi}{\partial r} - \frac{\mu_0}{B^2}\frac{\partial P}{\partial \theta} + \frac{2q}{R^2+q^2}\frac{\partial^2 \psi}{\partial s \partial \theta}\right). \tag{A.28}$$

We choose to use this equation rather than equation (4.73), because we take $P$ to be proportional to $\exp(i\theta)$ and hence the derivative of $P$ with respect to $\theta$ simplifies to $iP$. Now, we use equation (4.80) in equation ($A$.28), which gives two equations, one for inside and another for outside the loop, and in the following equations a subscript $i$ or $e$ refers to quantities inside or outside of the loop, respectively. First, we consider the region inside the loop:

$$\begin{aligned} r\omega^2\psi_1 &= v_{Ai}^2\left(-r\frac{d^2\psi_1}{ds^2} - \frac{\mu_0 i P_i}{B^2} + \frac{2qri}{R^2+q^2}\frac{d\psi_1}{ds}\right) \\ r\omega^2\psi_1 &= -rv_{Ai}^2\frac{d^2\psi_1}{ds^2} - \frac{iP_i}{\rho_i} + \frac{2qriv_{Ai}^2}{R^2+q^2}\frac{d\psi_1}{ds}. \end{aligned} \tag{A.29}$$

Then, rearranging for $P_i$:

$$\begin{aligned} \frac{iP_i}{\rho_i} &= -r\omega^2\psi_1 - rv_{Ai}^2\frac{d^2\psi_1}{ds^2} + \frac{2qriv_{Ai}^2}{R^2+q^2}\frac{d\psi_1}{ds} \\ P_i &= \rho_i\left(ir\omega^2\psi_1 + irv_{Ai}^2\frac{d^2\psi_1}{ds^2} + \frac{2qrv_{Ai}^2}{R^2+q^2}\frac{d\psi_1}{ds}\right). \end{aligned} \tag{A.30}$$

Repeating this for the region outside the loop leads to:

$$\begin{aligned} -\frac{\omega^2\psi_2}{r} &= v_{Ae}^2\left(\frac{1}{r}\frac{d^2\psi_2}{ds^2} - \frac{\mu_0 i P_e}{B^2} + \frac{2qi}{r(R^2+q^2)}\frac{d\psi_2}{ds}\right) \\ -\frac{\omega^2\psi_2}{r} &= \frac{v_{Ae}^2}{r}\frac{d^2\psi_2}{ds^2} - \frac{iP_e}{\rho_e} + \frac{2qv_{Ae}^2 i}{r(R^2+q^2)}\frac{d\psi_2}{ds} \\ \frac{iP_e}{\rho_e} &= \frac{\omega^2}{r}\psi_2 + \frac{v_{Ae}^2}{r}\frac{d^2\psi_2}{ds^2} + \frac{2qv_{Ae}^2 i}{r(R^2+q^2)}\frac{d\psi_2}{ds} \\ P_e &= \rho_e\left(-\frac{i\omega^2}{r}\psi_2 - \frac{iv_{Ae}^2}{r}\frac{d^2\psi_2}{ds^2} + \frac{2qv_{Ae}^2}{r(R^2+q^2)}\frac{d\psi_2}{ds}\right). \end{aligned} \tag{A.31}$$

Using equation (4.72), we can rewrite the boundary condition given in equation (4.60) in terms of $\psi$,

$$[\![\psi]\!] = 0 \quad \text{at} \quad r = a. \tag{A.32}$$

This implies that at the loop boundary, $\psi_2 = a^2\psi_1$. Equation (4.62) also tells us that $P_i = P_e$ at the boundary. Using these in equation (4.82) gives

$$P_i = \rho_e \left( -ia\omega^2\psi_1 - iav_{Ae}^2 \frac{d^2\psi_1}{ds^2} + \frac{2qav_{Ae}^2}{R^2+q^2}\frac{d\psi_1}{ds} \right), \tag{A.33}$$

and, evaluating equation (A.30) at $r = a$, we obtain

$$P_i = \rho_i \left( ia\omega^2\psi_1 + iav_{Ai}^2 \frac{d^2\psi_1}{ds^2} + \frac{2qav_{Ai}^2}{R^2+q^2}\frac{d\psi_1}{ds} \right). \tag{A.34}$$

Then, we equate the expressions for $P_i$ in equations (A.33) and (A.34), which gives

$$\begin{aligned} &\rho_i \left( ia\omega^2\psi_1 + iav_{Ai}^2 \frac{d^2\psi_1}{ds^2} + \frac{2qav_{Ai}^2}{R^2+q^2}\frac{d\psi_1}{ds} \right) \\ &- \rho_e \left( -ia\omega^2\psi_1 - iav_{Ae}^2 \frac{d^2\psi_1}{ds^2} + \frac{2qav_{Ae}^2}{R^2+q^2}\frac{d\psi_1}{ds} \right) = 0, \end{aligned} \tag{A.35}$$

which simplifies to

$$\frac{2iaB^2}{\mu_0}\frac{d^2\psi_1}{ds^2} + (\rho_i + \rho_e)ia\omega^2\psi_1 = 0. \tag{A.36}$$

Next, we divide through by $ia(\rho_i + \rho_e)$ to find

$$\frac{2B^2}{\mu_0(\rho_i+\rho_e)}\frac{d^2\psi_1}{ds^2} + \omega^2\psi_1 = 0, \tag{A.37}$$

which can be written as

$$\frac{d^2\psi_1}{ds^2} + \frac{\omega^2}{c_k^2}\psi_1 = 0, \tag{A.38}$$

where

$$c_k^2 = \frac{2B^2}{\mu_0(\rho_i+\rho_e)}, \tag{A.39}$$

is the squared kink speed of the tube and $B$ is evaluated at the loop axis.

## A.4 Frenet Basis

In this appendix we derive the Frenet basis for the loop axis. We start with the equation of the loop axis, which we write in terms of $s$ using equation (4.50):

$$\boldsymbol{X}_a = \begin{pmatrix} q\varphi \\ R\cos\varphi \\ R\sin\varphi \end{pmatrix} = \begin{pmatrix} q\left(\varphi_0 + \frac{s}{\sqrt{R^2+q^2}}\right) \\ R\cos\left(\varphi_0 + \frac{s}{\sqrt{R^2+q^2}}\right) \\ R\sin\left(\varphi_0 + \frac{s}{\sqrt{R^2+q^2}}\right) \end{pmatrix}. \tag{A.40}$$

Therefore it follows that the unit tangent vector, $\hat{\boldsymbol{\tau}}$, is

$$\begin{aligned} \hat{\boldsymbol{\tau}} = \frac{d\boldsymbol{X}_a}{ds} &= \begin{pmatrix} \frac{q}{\sqrt{R^2+q^2}} \\ -\frac{R}{\sqrt{R^2+q^2}}\sin\left(\varphi_0 + \frac{s}{\sqrt{R^2+q^2}}\right) \\ \frac{R}{\sqrt{R^2+q^2}}\cos\left(\varphi_0 + \frac{s}{\sqrt{R^2+q^2}}\right) \end{pmatrix} \\ &= \frac{1}{\sqrt{R^2+q^2}} \begin{pmatrix} q \\ -R\sin\left(\varphi_0 + \frac{s}{\sqrt{R^2+q^2}}\right) \\ R\cos\left(\varphi_0 + \frac{s}{\sqrt{R^2+q^2}}\right) \end{pmatrix}. \end{aligned} \tag{A.41}$$

Next, we consider the unit normal vector,

$$\hat{\boldsymbol{n}} = \frac{d\hat{\boldsymbol{\tau}}}{ds}\left|\frac{d\hat{\boldsymbol{\tau}}}{ds}\right|^{-1}. \tag{A.42}$$

Using equation (A.41) we obtain

$$\frac{d\hat{\boldsymbol{\tau}}}{ds} = \begin{pmatrix} 0 \\ -\frac{R}{R^2+q^2}\cos\left(\varphi_0 + \frac{s}{\sqrt{R^2+q^2}}\right) \\ -\frac{R}{R^2+q^2}\sin\left(\varphi_0 + \frac{s}{\sqrt{R^2+q^2}}\right) \end{pmatrix}, \tag{A.43}$$

and therefore,

$$\left|\frac{d\hat{\boldsymbol{\tau}}}{ds}\right| = \left(\frac{R^2}{(R^2+q^2)^2}\cos^2\left(\varphi_0 + \frac{s}{\sqrt{R^2+q^2}}\right) + \frac{R^2}{(R^2+q^2)^2}\sin^2\left(\varphi_0 + \frac{s}{\sqrt{R^2+q^2}}\right)\right)^{1/2}$$
$$= \left(\frac{R^2}{(R^2+q^2)^2}\right)^{1/2} = \frac{R}{R^2+q^2}. \tag{A.44}$$

Hence,

$$\hat{\boldsymbol{n}} = -\left(0, \cos\left(\varphi_0 + \frac{s}{\sqrt{R^2+q^2}}\right), \sin\left(\varphi_0 + \frac{s}{\sqrt{R^2+q^2}}\right)\right). \tag{A.45}$$

Finally, we obtain that the unit binormal vector is

$$\hat{\boldsymbol{b}} = \hat{\boldsymbol{\tau}} \times \hat{\boldsymbol{n}}$$
$$= \frac{1}{\sqrt{R^2+q^2}}\left(R, q\sin\left(\varphi_0 + \frac{s}{\sqrt{R^2+q^2}}\right), -q\cos\left(\varphi_0 + \frac{s}{\sqrt{R^2+q^2}}\right)\right). \tag{A.46}$$

## A.5 Derivation of Equations (4.108) and (4.109)

The first step in finding the value of $\varphi$ where $\boldsymbol{\xi}_\perp = 0$ requires us to consider the components of the following equation

$$\boldsymbol{\xi} - \boldsymbol{S}(\boldsymbol{\xi}\cdot\boldsymbol{S}) = 0, \tag{A.47}$$

which can be written in terms of the Frenet basis at the loop apex as given in equation (4.106):

$$\begin{pmatrix}\xi_{n_0}\\ \xi_{b_0}\\ \xi_{\tau_0}\end{pmatrix} - \begin{pmatrix}S_{n_0}\\ S_{b_0}\\ S_{\tau_0}\end{pmatrix}(\boldsymbol{\xi}\cdot\boldsymbol{S}) = 0. \tag{A.48}$$

From equation (4.103), we know we can write $\boldsymbol{\xi} = \xi_n\hat{\boldsymbol{n}} + \xi_b\hat{\boldsymbol{b}}$. In addition, as shown in equation (4.107), we see that we can write $\hat{\boldsymbol{n}}$ and $\hat{\boldsymbol{b}}$ in terms of $\hat{\boldsymbol{n}}_0$, $\hat{\boldsymbol{b}}_0$ and $\hat{\boldsymbol{\tau}}_0$, such that $\hat{\boldsymbol{n}} = \hat{n}_{n_0}\hat{\boldsymbol{n}}_0 + \hat{n}_{b_0}\hat{\boldsymbol{b}}_0 + \hat{n}_{\tau_0}\hat{\boldsymbol{\tau}}_{\mathbf{0}}$ and a similar expression can be written for $\hat{\boldsymbol{b}}$. Hence, we can write $\boldsymbol{\xi}$ in terms of $\hat{\boldsymbol{n}}_0$, $\hat{\boldsymbol{b}}_0$ and $\hat{\boldsymbol{\tau}}_0$ in the following

way:

$$\begin{aligned}\boldsymbol{\xi} &= \xi_{n_0}\hat{\boldsymbol{n}}_0 + \xi_{b_0}\hat{\boldsymbol{b}}_0 + \xi_{\tau_0}\hat{\boldsymbol{\tau}}_0 \\ &= (\xi_n\hat{n}_{n_0} + \xi_b\hat{b}_{n_0})\hat{\boldsymbol{n}}_0 + (\xi_n\hat{n}_{b_0} + \xi_b\hat{b}_{b_0})\hat{\boldsymbol{b}}_0 + (\xi_n\hat{n}_{\tau_0} + \xi_b\hat{b}_{\tau_0})\hat{\boldsymbol{\tau}}_0. \end{aligned} \tag{A.49}$$

Therefore, we can write equation (A.48) as

$$\begin{pmatrix} \xi_n\hat{n}_{n_0} + \xi_b\hat{b}_{n_0} \\ \xi_n\hat{n}_{b_0} + \xi_b\hat{b}_{b_0} \\ \xi_n\hat{n}_{\tau_0} + \xi_b\hat{b}_{\tau_0} \end{pmatrix} - \begin{pmatrix} S_{n_0} \\ S_{b_0} \\ S_{\tau_0} \end{pmatrix} (\boldsymbol{\xi}\cdot\boldsymbol{S}) = 0. \tag{A.50}$$

Taking the component of equation (A.50) which is in the $\hat{\boldsymbol{n}}_0$ direction, we obtain

$$\xi_n\hat{n}_{n_0} + \xi_b\hat{b}_{n_0} - S_{n_0}(\boldsymbol{\xi}\cdot\boldsymbol{S}) = 0, \tag{A.51}$$

which implies that

$$\boldsymbol{\xi}\cdot\boldsymbol{S} = \frac{\xi_n\hat{n}_{n_0} + \xi_b\hat{b}_{n_0}}{S_{n_0}}. \tag{A.52}$$

Next, taking the component of equation (A.50) which is in the $\hat{\boldsymbol{b}}_0$ direction, we obtain

$$\xi_n\hat{n}_{b_0} + \xi_b\hat{b}_{b_0} - S_{b_0}(\boldsymbol{\xi}\cdot\boldsymbol{S}) = 0, \tag{A.53}$$

and use equation (A.52) to find

$$\xi_n\hat{n}_{b_0} + \xi_b\hat{b}_{b_0} - \frac{S_{b_0}}{S_{n_0}}(\xi_n\hat{n}_{n_0} + \xi_b\hat{b}_{n_0}) = 0. \tag{A.54}$$

Then, substituting in the appropriate components from equations (4.103), (4.105) and (4.107), we obtain

$$-\cos\beta\frac{q\cos\varphi}{\sqrt{R^2+q^2}} + \sin\beta\frac{R^2+q^2\sin\varphi}{R^2+q^2} = \frac{\sin\chi\cos\varsigma}{\cos\chi}\left(\sin\varphi\cos\beta + \frac{q\cos\varphi\sin\beta}{\sqrt{R^2+q^2}}\right) \tag{A.55}$$

Note that each term in the above equation would also have an extra factor of $A\Psi(s)\sin(\omega t + \alpha_s)$, which has been omitted here because it can be cancelled.

Finally, upon dividing through by $\cos\beta$, we obtain

$$\frac{(R^2+q^2\sin\varphi)\tan\beta}{R^2+q^2}-\frac{q\cos\varphi}{\sqrt{R^2+q^2}}=\tan\chi\cos\varsigma\left(\sin\varphi+\frac{q\cos\varphi\tan\beta}{\sqrt{R^2+q^2}}\right). \tag{A.56}$$

Repeating this method with the $\hat{\boldsymbol{\tau}}_0$ component of equation (A.50) gives

$$\xi_n\hat{n}_{\tau_0}+\xi_b\hat{b}_{\tau_0}-\frac{S_{\tau_0}}{S_{n_0}}(\xi_n\hat{n}_{n_0}+\xi_b\hat{b}_{n_0})=0, \tag{A.57}$$

which leads to

$$\begin{aligned}\frac{R\cos\varphi\cos\beta}{\sqrt{R^2+q^2}}+\frac{qR\sin\beta(1-\sin\varphi)}{R^2+q^2}&=\frac{\sin\chi\sin\varsigma}{\cos\chi}\left(\sin\varphi\cos\beta+\frac{q\cos\varphi\sin\beta}{\sqrt{R^2+q^2}}\right)\\ \frac{R\cos\varphi}{\sqrt{R^2+q^2}}+\frac{qR(1-\sin\varphi)\tan\beta}{R^2+q^2}&=\tan\chi\sin\varsigma\left(\sin\varphi+\frac{q\cos\varphi\tan\beta}{\sqrt{R^2+q^2}}\right).\end{aligned} \tag{A.58}$$

# Appendix B

# Source Code Used to Implement the Shooting Method

The following source code was written in Fortran 90 and used to solve equation (5.10). The shooting method was used with the fourth-order Runge-Kutta method to obtain a value for $\Omega$, the dimensionless kink oscillation frequency. Note that the variable `zeta` is equivalent to $S$ in equation (5.10).

Initially the number of steps, `nn`, the initial condition for $d\Psi/dS$, `z0`, and the accuracy of the program, `acc`, were varied to assess their effect on the resulting value of $\Omega$. After testing to find values for these parameters which did not change the value of $\Omega$ found by the program they were chosen to be `nn` $= 1 \times 10^4$, `z0` $= 1.0$ and `acc` $= 1 \times 10^{-9}$.

```
program shootingmethodnonplanar
!
!Aim: To solve the system of equations
!dp/dzeta=f(zeta,p,z)=z
!dz/dzeta=g(zeta,p,z)=-Omega**2*exp((-RoH)*sin(zeta*Pi))*p
!with boundary conditions p(0)=p(1)=0
!and initial condition z(0)=1
!to find the value of Omega.
!Method: Shooting method (for Omega) with Runge-Kutta 4
!
implicit none
```

```
integer :: nn,count
double precision :: zeta,z,h,p0,pL
double precision :: OG1,OG2,OG3,pL1,pL2,pL3,acc,z0,RoH

!!Definitions of the above variables:
!nn: Number of steps
!count: Used to count guesses
!zeta,z: See aim above.
!h =1/nn
!p0 =p(0) and pL =p(1)
!OG1,OG2,OG3: Guesses for Omega.
!pL1,pL2,pL3: Values of p(1) corresponding to the Omega guesses.
!acc: Numerical values pL1, pL2, pL3 are compared to pL. acc
!     defines the number of decimal places which must be equal
!     before the numerical result is considered equal to pL.
!z0: dp/dzeta at zeta=0 (z(0))
!RoH =R/H


!Get run parameters from the user
print*,'Enter loop parameters:'
print*, 'R/H='
read*,RoH
!print*,'Enter initial condition: dp/ds(0)='
!read*,z0
z0=1.d0
!print*,'Enter number of steps nn'
!read*, nn
nn=10000
!print*,'Solve to an accuracy of '
!read*,acc
acc=1.0e-9
print*, 'Enter first guess for Omega'
```

```
read*,OG1

!Boundary conditions p(0)=p(1)=0 are fixed
!so can define them in the program:
p0=0.d0
pL=0.d0

!Divide the loop into nn equal chunks
h=1.d0/nn


!Solve for first time - uses 1st guess (OG1)
call rk4(h,nn,p0,z0,zeta,pL1,z,pL,acc,OG1,RoH)

!Print 1st guess results
write (unit=6,fmt="(a,f20.16,a,e14.7)")&
'Guess  1 results: Omega=',OG1,'     p(1)=',pL1

!Check pL1 against boundary condition pL
if (abs(pL1-pL)<acc) stop


!Ask user for second guess for Omega (OG2)
print*,'Enter second guess for Omega'
read*,OG2

!Solve for second time - uses 2nd guess (OG2)
call rk4(h,nn,p0,z0,zeta,pL2,z,pL,acc,OG2,RoH)

!Print 2nd guess results
write (unit=6,fmt="(a,f20.16,a,e14.7)")&
'Guess  2 results: Omega=',OG2,'     p(1)=',pL2

!Check pL2 against boundary condition pL
```

```
if (abs(pL2-pL)<acc) stop


!Now have enough info to perform a linear interpolation
!and iterate to find the next guess for Omega

print*,' '
print*,'Iterating...'
print*,' '

!Guess counter
count=2
1 count=count+1

!Perform the linear interpolation
If (pL2==pL1) then
  print*,' '
  print*,'Divide by zero in linear interpolation! Abort!'
  print*,'Try reducing accuracy for next run.'
  stop
else
  OG3=OG1+(OG2-OG1)*(pL-pL1)/(pL2-pL1)
end if

!Solve again using new guess from linear interpolation (OG3)
call rk4(h,nn,p0,z0,zeta,pL3,z,pL,acc,OG3,RoH)

!Print results
write (unit=6,fmt="(a,i3,a,f20.16,a,e14.7)")&
'Guess',count,' results: Omega=',OG3,'     p(1)=',pL3

!Check pL3 against boundary condition pL
!!Stop if result is to required accuracy
!!Otherwise update values to be used in the linear interpolation
```

```
!!Latest guesses used to give
!!better numbers for the interpolation
if (abs(pL3-pL)<acc) then
  stop
else
  OG1=OG2
  OG2=OG3
  pL1=pL2
  pL2=pL3

  Go To 1
end if

end program
!*****************************************************************
subroutine rk4(h,nn,p0,z0,zeta,p,z,pL,acc,OG,RoH)

integer :: n,nn,ierrzeta,ierrp,ierrz,i
double precision :: zeta,p,zetaold,pold,z,zold
double precision :: h,k1,k2,k3,k4,m1,m2,m3,m4,OG,RoH
double precision :: p0,z0,pL,acc
double precision, allocatable :: Azeta(:),Ap(:),Az(:)

!!Definitions of the above variables:
!n, i: Integers used for counting loop steps
!ierrzeta, ierrp, ierrz: Integers used for error checking
!                        the arrays
!p: See 'aim' in main program
!zetaold, pold, zold: Old values of zeta, p, z
!k1,k2,k3,k4,m1,m2,m3,m4: As defined in the standard RK4
!                         definition
!OG: Current guess for Omega
!Azeta(:), Ap(:), Az(:): Arrays to contain the values of
!                        zeta, p, z
```

```
!
!!!All other variables are as defined in the main program


!Set initial values from main program
zeta=0.d0
p=p0
z=z0

!Check allocation status and if ok
!allocate arrays to store zeta,p,z data
!Azeta
if (allocated(Azeta)) then
  print*,'Already allocated Azeta'
else
  allocate(Azeta(0:nn),stat=ierrzeta)
end if

if (ierrzeta/=0)then
  print*,'Allocation of Azeta failed in subroutine RK4'
  stop
end if
!Ap
if (allocated(Ap)) then
  print*,'Already allocated Ap'
else
  allocate(Ap(0:nn),stat=ierrp)
end if

if (ierrp/=0)then
  print*,'Allocation of Ap failed in subroutine RK4'
  stop
end if
!Az
```

```
if (allocated(Az)) then
  print*,'Already allocated Az'
else
  allocate(Az(0:nn),stat=ierrz)
end if

if (ierrz/=0)then
  print*,'Allocation of Az failed in subroutine RK4'
  stop
end if

!Put inital values into arrays
Azeta(0)=zeta
Ap(0)=p
Az(0)=z

!Time loop
do n=1,nn
  !Update 'old' values from 'last' step
  zetaold=zeta
  pold=p
  zold=z
  !For both equations calculate the 4 RK terms
  !for the 4 evaluations of the RHS of the equation
  !!! k - 1st step (k1)
  call get_f(h,zetaold,pold,zold,k1)
  !!! m - 1st step (m1)
  call get_g(h,zetaold,pold,zold,m1,OG,RoH)
  !!! k - 2nd step (k2)
  call get_f(h,zetaold+0.5*h,pold+0.5*k1,zold+0.5*m1,k2)
  !!! m - 2nd step (m2)
  call get_g(h,zetaold+0.5*h,pold+0.5*k1,zold+0.5*m1,m2,OG,RoH)
  !!! k - 3rd step (k3)
  call get_f(h,zetaold+0.5*h,pold+0.5*k2,zold+0.5*m2,k3)
```

```
  !!! m - 3rd step (m3)
  call get_g(h,zetaold+0.5*h,pold+0.5*k2,zold+0.5*m2,m3,OG,RoH)
  !!! k - 4th step (k4)
  call get_f(h,zetaold+h,pold+k3,zold+m3,k4)
  !!! m - 4th step (m4)
  call get_g(h,zetaold+h,pold+k3,zold+m3,m4,OG,RoH)

  !Evolve zeta, p and z by one timestep
  zeta=h*n
  p=pold+(k1+2*k2+2*k3+k4)/6.d0
  z=zold+(m1+2*m2+2*m3+m4)/6.d0

  !Put zeta,p,z into the arrays
  Azeta(n)=zeta
  Ap(n)=p
  Az(n)=z
enddo

!Check final p value (approx p at zeta=1) against
!boundary condition pL
!!If result is within required accuracy write values to file
if (abs(p-pL)<acc) then
  !Open a file to write results to
  open(unit=7,file='outSMNP.txt')

  !Write array to file
  do i=0,nn
    write(unit=7,fmt="(3e12.4)")Azeta(i),Ap(i),Az(i)
  end do

  !Finished with the output file
  close(unit=7)
end if
```

```
!Deallocate arrays
deallocate(Azeta)
deallocate(Ap)
deallocate(Az)

end subroutine
!*************************************************************
subroutine get_f(h,zeta,p,z,k)
!Calculate dp/dzeta=f(zeta,p,z)=z

implicit none

double precision :: zeta,p,z,h,k,f

!p: See 'aim' in main program
!k and f are used in the RK4 method.
!Other variables are defined as in the main program.


!Calculate f as defined above
f=z

!Calculate k
k=h*f

end subroutine
!*************************************************************
subroutine get_g(h,zeta,p,z,m,OG,RoH)
!Calculate
!dz/dzeta=g(zeta,p,z)=-Omega**2*exp((-RoH)*sin(zeta*Pi))*p

implicit none

double precision :: zeta,p,z,h,m,g,OG,RoH,pi
```

```
!p: See 'aim' in main program
!m and g are used in the RK4 method
!OG is the current guess for Omega
!pi is pi
!Other variables are as defined in the main program


!Get value for pi
pi=4.d0*atan(1.d0)

!Calculate g as defined above
g=(-1.d0)*(OG**2.d0)*exp((-RoH)*sin(zeta*pi))*p

!Calculate m
m=h*g

end subroutine
!***************************************************************
```

# Bibliography


Andries, J., Arregui, I., and Goossens, M. (2005a). *The Astrophysical Journal,* **624**, L57.

Andries, J., Goossens, M., Hollweg, J. V., Arregui, I., and Van Doorsselaere, T. (2005b). *Astronomy and Astrophysics,* **430**, 1109.

Anzer, U. and Tandberg-Hanssen, E. (1970). *Solar Physics,* **11**, 61.

Aschwanden, M. (2009). *Physics of the Solar Corona. An Introduction with Problems and Solutions*. UK: Springer (in association with Praxis Publishing).

Aschwanden, M. J. (2001). *The Astrophysical Journal,* **560**, 1035.

Aschwanden, M. J. (2003). *ArXiv Astrophysics e-prints, arXiv:astro-ph/0309505,* .

Aschwanden, M. J. (2009). *Space Science Reviews,* **149**, 31.

Aschwanden, M. J., De Pontieu, B., Schrijver, C. J., and Title, A. M. (2002). *Solar Physics,* **206**, 99.

Aschwanden, M. J., Fletcher, L., Schrijver, C. J., and Alexander, D. (1999). *The Astrophysical Journal,* **520**, 880.

Aschwanden, M. J., Poland, A. I., and Rabin, D. M. (2001). *Annual Review of Astronomy and Astrophysics,* **39**, 175.

Aschwanden, M. J. and Schrijver, C. J. (2011). *The Astrophysical Journal,* **736**, 102.

Aschwanden, M. J., Wülser, J.-P., Nitta, N. V., and Lemen, J. R. (2008). *The Astrophysical Journal,* **679**, 827.

Baumjohann, W. and Treumann, R. A. (1997). *Basic Space Plasma Physics*. UK: Imperial College Press.

Chaplin, B. and Ballai, I. (2005). *Astronomy and Geophysics,* **46**, 4.27.

Choudhuri, A. R. (1998). *The Physics of Fluids and Plasmas, An Introduction for Astrophysicists*. UK: Cambridge University Press.

De Moortel, I. and Brady, C. S. (2007). *The Astrophysical Journal,* **664**, 1210.

De Moortel, I. and Nakariakov, V. M. (2012). *Philosophical Transactions of the Royal Society A,* **370**, 3193.

Dere, K. P., Brueckner, G. E., Howard, R. A., Michels, D. J., and Delaboudiniere, J. P. (1999). *The Astrophysical Journal,* **516**, 465.

Díaz, A. J., Zaqarashvili, T., and Roberts, B. (2006). *Astronomy and Astrophysics,* **455**, 709.

Dymova, M. V. and Ruderman, M. S. (2005). *Solar Physics,* **229**, 79.

Dymova, M. V. and Ruderman, M. S. (2006). *Astronomy and Astrophysics,* **459**, 241.

Edwin, P. M. and Roberts, B. (1982). *Solar Physics,* **76**, 239.

Edwin, P. M. and Roberts, B. (1983). *Solar Physics,* **88**, 179.

Erdélyi, R. and Morton, R. J. (2009). *Astronomy and Astrophysics,* **494**, 295.

Foukal, P. V. (2004). *Solar Astrophysics*. Germany: WILEY-VCH.

Goedbloed, H. and Poedts, S. (2004). *Principles of Magnetohydrodynamics with Applications to Laboratory and Astrophysical Plasmas*. USA: Cambridge University Press.

Golub, L. and Pasachoff, J. M. (2002). *Nearest Star: The Surprising Science of Our Sun*. USA: Harvard University Press.

Golub, L. and Pasachoff, J. M. (2010). *The Solar Corona*. UK: Cambridge University Press, Second edition.

Kuridze, D., Morton, R. J., Erdélyi, R., Dorrian, G. D., Mathioudakis, M., Jess, D. B., and Keenan, F. P. (2012). *The Astrophysical Journal,* **750**, 51.

Luna, M., Terradas, J., Oliver, R., and Ballester, J. L. (2008). *The Astrophysical Journal,* **676**, 717.

Luna, M., Terradas, J., Oliver, R., and Ballester, J. L. (2009). *The Astrophysical Journal,* **692**, 1582.

Luna, M., Terradas, J., Oliver, R., and Ballester, J. L. (2010). *The Astrophysical Journal,* **716**, 1371.

McEwan, M. P., Donnelly, G. R., Díaz, A. J., and Roberts, B. (2006). *Astronomy and Astrophysics,* **460**, 893.

Morton, R. J. and Erdélyi, R. (2009a). *Astronomy and Astrophysics,* **502**, 315.

Morton, R. J. and Erdélyi, R. (2009b). *The Astrophysical Journal,* **707**, 750.

Morton, R. J. and Ruderman, M. S. (2011). *Astronomy and Astrophysics,* **527**, A53.

Nakariakov, V. M. and Ofman, L. (2001). *Astronomy and Astrophysics,* **372**, L53.

Nakariakov, V. M., Ofman, L., DeLuca, E. E., Roberts, B., and Davila, J. M. (1999). *Science,* **285**, 862.

Nakariakov, V. M. and Verwichte, E. (2005). *Living Reviews in Solar Physics,* **2**, 3.

Plunkett, S. P., Vourlidas, A., Šimberová, S., Karlický, M., Kotrč, P., Heinzel, P., Kupryakov, Y. A., Guo, W. P., and Wu, S. T. (2000). *Solar Physics,* **194**, 371.

Priest, E. R. (2000). *Solar Magnetohydrodynamics.* Holland: D. Reidel Publishing Company.

Roberts, B. (1981a). *Solar Physics,* **69**, 27.

Roberts, B. (1981b). *Solar Physics,* **69**, 39.

Roberts, B., Edwin, P. M., and Benz, A. O. (1984). *The Astrophysical Journal,* **279**, 857.

Robertson, D., Ruderman, M. S., and Taroyan, Y. (2010). *Astronomy and Astrophysics,* **515**, A33.

Rosenberg, H. (1970). *Astronomy and Astrophysics,* **9**, 159.

Ruderman, M. S. (2003). *Astronomy and Astrophysics,* **409**, 287.

Ruderman, M. S. (2007). *Solar Physics,* **246**, 119.

Ruderman, M. S. (2009). *Astronomy and Astrophysics,* **506**, 885.

Ruderman, M. S. and Erdélyi, R. (2009). *Space Science Review,* **149**, 199–228.

Ruderman, M. S., Verth, G., and Erdélyi, R. (2008). *The Astrophysical Journal,* **686**, 694.

Rust, D. M. (2003). *Advances in Space Research,* **32**, 1895.

Rust, D. M. and Kumar, A. (1996). *The Astrophysical Journal,* **464**, L199.

Ryutov, D. A. and Ryutova, M. P. (1976). *Soviet Physics, Journal of Experimental and Theoretical Physics,* **43**, 491.

Schrijver, C. J., Aschwanden, M. J., and Title, A. M. (2002). *Solar Physics,* **206**, 69.

Solanki, S. K., Inhester, B., and Schüssler, M. (2006). *Reports on Progress in Physics,* **69**, 563.

Sterling, A. C. (2000). *Solar Physics,* **196**, 79.

Terradas, J., Oliver, R., and Ballester, J. L. (2006). *The Astrophysical Journal,* **650**, L91.

Uchida, Y. (1970). *Publications of the Astronomical Society of Japan,* **22**, 341.

Van Doorsselaere, T., Debosscher, A., Andries, J., and Poedts, S. (2004). *Astronomy and Astrophysics,* **424**, 1065.

Van Doorsselaere, T., Ruderman, M. S., and Robertson, D. (2008). *Astronomy and Astrophysics,* **485**, 849.

Van Doorsselaere, T., Verwichte, E., and Terradas, J. (2009). *Space Science Reviews,* **149**, 299.

Verth, G. and Erdélyi, R. (2008). *Astronomy and Astrophysics,* **486**, 1015.

Verwichte, E., Nakariakov, V. M., Ofman, L., and Deluca, E. E. (2004). *Solar Physics,* **223**, 77.

Wang, T. J. and Solanki, S. K. (2004). *Astronomy and Astrophysics,* **421**, L33.

Wang, T. J., Solanki, S. K., and Selwa, M. (2008). *Astronomy and Astrophysics,* **489**, 1307.

White, R. S. and Verwichte, E. (2012). *Astronomy and Astrophysics,* **537**, A49.